THEORETICAL STUDY OF THERMAL SPALLING OF BRITTLE MATERIALS

by

Thang Dinh Nguyen

Dissertation submitted to the Faculty of the

Virginia Polytechnic Institute and State University

in partial fulfillment of the requirements for the degree of

Doctor of Philosophy

in

Mechanical Engineering

APPROVED:

Dr. J. R. Thomas, Jr.

Dr. D. P. H. Hasselman

Dr. C. E. Knight

Dr. B. Vick

Dr. T. E. Diller

May, 1986

Blacksburg, Virginia

THEORETICAL STUDY OF THERMAL SPALLING OF BRITTLE MATERIALS

by

Thang Dinh Nguyen

Dr. J. R. Thomas, Jr.

Mechanical Engineering

(ABSTRACT)

In this work several problems related to thermal spalling are considered. First, a novel approximate technique to solve general linear heat-conduction problems with changing boundary conditions and locations is proposed. The technique is based on the concept of linear superposition and the possibility to transform the initial condition into a time-varying boundary condition. The proposed technique is evaluated and compared to some of the existing techniques. The individual contribution of several stress components and their combined effects on the risk of failure are then considered for a theoretical axi-symmetric body subjected to uniform unconfined heating. The results indicate that using a single stress component in the prediction of failure for brittle materials is not justified in general. Finally, the thermal spalling process in jet piercing operations is studied. The finite element model consists of a large axi-symmetric object subjected to a confined heat flux. The numerical results are used to study the combined effects of several stress components and the influence of material properties and heat flux intensity on the spalling rate and spallability of brittle materials. The results compare favorably with experimental results reported in the literature. A set of plots are offered for use in design. Possible extensions and variations of the present work are also discussed.

ACKNOWLEDGEMENTS

The author wishes to dedicate this work to his parents, brothers, and sister. The author expresses much thanks to Dr. J. R. Thomas, Jr., for his help, support, and friendship during the preparation of this work. The author also thanks Dr. D. P. H. Hasselman, Dr. C. E. Knight, Dr. B. Vick, and Dr. T. E. Diller for their helpful suggestions in the course of the research and for serving on his committee. The author feels deeply grateful for the suggestions of Dr. G. W. Swift and Dr. S. L. Ling on various theoretical aspects of the research. Finally, the author would like to express special thanks to his dear friend, Dieu Hien, for her moral support and encouragements.

TABLE OF CONTENTS

NOMENCLATURE

Symbols	Descriptions
Bi	Biot number, hR_q/k
C_p	Specific heat
E	Modulus of elasticity
F	Failure factor
F_c	Critical value of the failure factor
h	Convective heat transfer coefficient
k	Thermal conductivity of material
k_0	Thermal conductivity at boundary at x = 0
k_L	Thermal conductivity at boundary at x = 1
$K(\beta m_i, x)$	Eigenfunction corresponding to βm_i
L	Longitudinal dimension of an axi-symmetric body
q''	Heat flux intensity
r	Radial coordinate
r^*	Non-dimensionalized r, r/R_q
R_q	Radius of the circular heat flux area
R_l	Linear spalling rate
R	Radial size of an axi-symmetric body
R_{st}	Strength ratio, S_t/S_c
R_t	Thermal stress resistance, $(k/q''R_q)(S_t(1-\nu)/E\alpha)$
R_v	Volumetric spalling rate
S_c	Compressive strength
S_t	Tensile strength

S_u	Ultimate strength
t	Time
t^*	Non-dimensional time or Fourier number, $\kappa t/R_q^2$
t_i	Time of the i^{th} spalling
T_i	Temperature in the i^{th} thermal phase
T_0	Reference temperature
$u[.]$	Unit step function
x	Longitudinal coordinate
x_i	Longitudinal displacement of the boundary after the i^{th} thermal phase
x^*	Non-dimensionalized x, x/R_q
α	Linear thermal expansion coefficient
βm_i	Eigenvalues in the i^{th}thermal phase
ΔT	Temperature difference
κ	Thermal diffusivity
ν	Poisson's ratio
ψ_i	Boundary condition at x = L in the i^{th} thermal phase
ρ	Density
σ	Stress
σ^*	Non-dimensional stress, $(k/q''R_q)\sigma(1-\nu)/E\alpha$
σ_r	Radial stress
σ_{rx}	Shear stress
σ_t	Tangential stress
σ_x	Axial stress
ζ	Thermal layer
ζ^*	Non-dimensionalized thermal layer ζ/R_q

LIST OF FIGURES

2.0 LIST OF TABLES

I. INTRODUCTION

Thermal spalling of brittle materials induced by high intensity heat flux is an important factor in many engineering designs. Depending on each application, a high spallability may be desirable or undesirable. For example, a low spallability, or equivalently, a high resistance to thermal stress, is crucial in the design of nuclear reactors, nuclear waste storages, refractory bricks, etc. On the other hand, in destructive operations such as jet-chanelling, jet-quarrying, or jet-surfacing, a high spalling rate determines their economical viability compared to other operations.

Despite its importance, the field of thermal spalling is still largely unexplored, partly due to its late development and partly due to the complexity of thermo-elastic problems. The literature directly related to thermal spalling is very scarce, with only a few papers reporting experimental results and a few analytical works.

The experiments to determine the effects of thermo-elastic, petrographic, and external factors on spalling are too diverse in test conditions to draw any definite conclusion and are, in cases, contradicting. Extrapolation of these experimental observations to predict spalling behavior of materials in practice may lead to erroneous conclusions. Furthermore, most of these experiments have not been substantiated by analytical models. The few existing analytical or finite element models are constrained by many simplifying assumptions which are not compatible with test conditions or actual operations. Some of the as-

sumptions most commonly made are one-dimensional temperature distributions, infinite geometry, and failure by a single stress component. On the last assumption, the investigators still have divided opinions of the mode of failure, i.e., by shear, compressive or tensile stress. Also, no attempt has been made to study the state of stress after the first spalling.

In fact, simplifying assumptions are unavoidable because thermal spalling is a very complex process encompassing several fields of engineering. In most cases in practice, heat fluxes are confined to a finite region, generating a complex three dimensional temperature distribution, which in turn induces a highly complicated stress field. Rock mechanics then determines the formation and propagation of cracks which finally may result in fracture of the material. The location and path of spalling in turn determine the residual temperature distribution and geometrical configuration of the next stage, and so on. The complexity is compounded by the fact that material properties change with temperature and upon crack formation.

The objectives of this study are first to develop a technique to solve heat-conduction problems of moving boundaries and with sudden changes in boundary conditions. This type of problems are typical of thermal spalling in which the heat source is moved to the new surface after each spalling. Next, the combined effects of several stress components produced by unconfined heating on fracture are studied. Finally, thermal spalling produced by confined heating is studied. The report is organized as follows.

In chapter II, the literature review presents the state-of-the-art and at the same time sketches the development of the field.

In chapter III, an approximate technique to solve finite heat-conduction problems with discretely moving boundaries and sudden changes in boundary conditions is presented in general terms, along with numerical evaluations of the technique and examples of its applications. The underlying concept is to transform the initial condition in each thermal phase into time-varying fictitious conditions at the boundaries, making the general solution a linear superposition of solutions to simpler complementary problems. This transformation allows more computationally efficient solutions with a high degree of accuracy.

In chapter IV, the combining effects of several stress components in a finite axi-symmetric object subjected to a uniform heat flux over the front face are studied for the purpose of evaluating the assumption of fracture by a single stress component. The temperature distributions are obtained by the exact technique of integral transform. Stress distributions are then obtained from a finite-element model. The modified Coulomb-Mohr theory of failure is used to develop a failure factor which relates the combined effects of several stress components to failure. Numerical results including stress and failure factor distributions show that using any single stress component in the study of failure in brittle materials is only justified under specific conditions. In general, a more comprehensive theory of failure is needed.

The problem of confined heat flux is considered in chapter V. The model consists of a large axi-symmetric body subjected to a confined heat flux over a circular region on the surface. The dimensions are chosen

to approximate an infinitely large medium. The non-dimensional thermal stress resistance, strength ratio and failure factor are defined and used to determine the spallability of materials. Only the first spalling is considered because of the prohibitive computing time and because the first thermal phase gives good approximation to subsequent phases. The results, to a certain extent, explain many experimental and on-site observations on the shape of spalls, size of spalls, surface temperature at the exposed surface, etc. Attempts are also made to study the contribution of each stress component to failure in this case of highly complex stress distributions. Examples are given to illustrate the design use of the plotted results.

Finally, chapter VI relates and compares the results of the previous chapters. Suggestions are also made on the possible extensions of the present work to other problems of interest.

II. LITERATURE REVIEW

Compared to many other fields of thermal stress, thermal spalling has not had adequate attention from the engineering community. The literature directly related to thermal spalling is very scarce. Experimental data available in the open literature are limited to a few papers. Most analytical models are based on many simplifying assumptions which may deviate greatly from the actual problems. This might be partly due to the late development of the field and partly due to the intractability of any analytical solution.

A theory of thermal spalling was first formulated by Norton [38] in 1925. From observations of fracture in bricks, Norton conjectured that a low coefficient of thermal expansion and a coarse structure were indications of good resistance against spalling. Norton's analytical model is based on a semi-infinite body, whose surface is suddenly cooled and maintained at a fixed temperature. The tendency to spall is defined as $Cs\alpha/\sqrt{\kappa\varepsilon_s}$ where s is the size of the specimen, ε_s the maximum shearing strain, κ the thermal diffusivity, α the linear coefficient of thermal expansion, and C a scaling factor. According to this model, spalling is due to shear, which is directly proportional to temperature gradient. Therefore, failure is expected to occur along the surface where the temperture gradient is largest. However, this model also predicts a lower tendency to spall at corners, which contradicts on-site observations. Norton explained that spalls at corners are due to structurally weak points rather than stress distribution. According to this theory, a good

resistance to thermal shock corresponds to high diffusivity, low thermal expansion coefficient, and high shear strength.

In disagreement with Norton, Preston [48] claimed that fracture is due to tension normal to the direction of heat flow, hence, cracks would form normal to isothermal planes and propagate in a direction normal to the heated surface. Using an infinitely thick body as model, Preston showed that fracture depends on $E\alpha\Delta T$, where E is the modulus of elasticity and ΔT the temperature rise, and is independent of thermal diffusivity. With this model, if spalling occurred, it would occur in the first quenching where ΔT is largest; if not, spalling would never occur afterwards.

In response to Preston's criticisms, Norton [40] suggested that in general, the ratio between shear and tensile strengths, in combination with the grouped parameter defined above as the tendency to spall, determines the mode of failure--by tension or by shear. To verify this conjecture, stresses in bakelite brick specimens, repeatedly heated and cooled in an air blast, were measured by photo-elastic methods. Based on experimental results, Norton concluded that spalling is by shear under rapid heating, and by tensile stresses normal to the direction of heat flow upon cooling. Shear failures were also observed to initiate from the corners and failures in tension to initiate close to the central axis parallel to the direction of heat flow.

Thermal shock resistance, related to the reciprocal of Norton's definition of tendency to spall, was experimentally determined by Lidman and Bobrowsky [30]. Bricks subjected to repeated heating and quenching showed that a relationship exists between the grouped parameter $kS_t/\alpha E$,

where k is the thermal conductivity, and thermal shock resistance. It was observed that for most cases, failure occured during cooling and due to tensile stresses. It was conjectured that when shear strength is less than half the tensile strength, failure by shear would occur before failure in tension.

Similar experiments were performed by Manson [31,34] and Manson and Smith [32,33], considering different regimes of heat transfer. Thin disks of rock, thermally insulated at both faces and subjected to repeated quenching, were used in the experiment. Experimental results showed that thermal shock resistance of brittle materials depends on thermal conductivity and the grouped parameter $S_t/E\alpha$. Maximum tensile stress and Weibull's statistical theory of failure were found to correlate well with experimental data and with each other. Manson and Smith observed that at low heat transfer coefficients, alumina bricks, having higher thermal conductivity, are less resistant to thermal shock than beryllium bricks. At high heat transfer coefficients, the reverse is true: high conductivity indicates better resistance to thermal shock. A low modulus of elasticity was also observed to enhance thermal shock resistance.

Henke, Thomas, and Hasselman [26] offered an analytical model for a long cylinder subjected to sudden change in temperature, which predicts dependence of thermal shock resistance on diffusivity. Thermal shock resistance was defined as the critical quenching temperature difference causing failure, and was found to be proportional to $\sqrt{k\rho C_p}S_t(1-\nu)/E\alpha$. The grouped parameter $\sqrt{k\rho C_p}$, rewritten as $k/\sqrt{\kappa}$, suggests that high diffusivity will reduce resistance to thermal shock, in contradiction to Norton's conjecture.

The effects of material properties, structure, texture, and composition on thermal spallability of rocks in jet piercing were experimentally studied by Soles and Geller [51]. Thermal spallability was rated on a scale of 1 to 10. A high rating corresponds to rapid piercing and clean spalls. At the lowest rating, rocks tend to soften and melt rather than spall. At intermediate rating, rocks spall with a certain amount of fusion and blockage. Of all the factors studied, the only evident indicator of spallability was rock composition. In general, a large component of quartz and granite indicates good spallability. Soft and pliable minerals like mica, nepheline, and mafic (ferro magnesian) minerals inhibits spalling. Rock composition also affects linear thermal expansion coefficient which in turn determines spallability. Rocks with thermal expansion of less than 0.75 percent from ambient temperature up to 573^{o}C showed poor spallability while those expanding more than one percent were pierced easily [51]. Specific heat, mechanical strength, texture, and structure did not give any reliable correlation with spallability. However, the range of specimens used suggests that they were not chosen selectively enough to show the isolated effects of each factor. The authors also described the shape of the spalls, which could cast some light on the mechanics of spalling. Regardless of rock types or hole depth, the flakes were observed to be very similar in shape: thin, curved and ocasionally bevelled at the edges. The locus of potential rupture was observed to be a plane extending from 1 to 3 mm below the surface facing the jet flame. Evidence suggested that these spalls initiated at the outer surface of the rock at an irregularity or on an inclined plane, then propagated to the center along the plane of potential

rupture, crossing all brittle material species. Soles and Geller [51] conjectured that the thickness of the spall was governed by the temperature gradient. A steep gradient would cause thin spall. This was supported by the observation that the temperature of the freshly exposed surface was only negligibly higher than the bulk temperature of the rock. No direct relation between spallability and the grouped parameter $S_t(1-\nu)/E\alpha$ was observed.

Mirkovich [35] extended Soles and Geller's [51] work by studying the effects of thermal properties on piercing rate. A linear regression of the latters' experimental results gives the functional form of the piercing rate in cm/s as $R = 21.3\alpha\kappa - 0.0175$, where κ is measured at 200°C in cm^2/s, and α expressed as percent elongation from 25 to 500°C. Mirkovich acknowledged that such external factors as heat transfer rate and the configuration of the heated surface were omitted in the regression model. The above relation is reminiscent of Henke, Thomas and Hasselman's result [26], and contradicts the common belief that low thermal diffusivity induces sharp temperature gradient, hence high stress and better piereceability. Mirkovich explained this paradox following the line presented by Manson and Smith [27,28]. Mirkovich reported that for rocks of low to intermediate spallability, the continuous piercing rate is usually less than the initial piercing rate, probably due to physical and chemical change at the heated surface. It was also noted that failures were governed not only by the maximum stress but also by the stress distribution within the body, requiring a statistical theory of failure, as mentioned by Manson and Smith. The fact that the piercing rate depends only on $\alpha\kappa$ suggests that other parameters such as the modulus of

elasticity and mechanical strength do not differ much from one rock type to another and do not change much with temperature. It was also noted that thermal conductivity of rocks decreases with increasing temperature and the difference between thermal conductivity of different rock types diminishes with increasing temperature.

In a subsequent experiment, Mirkovich and Bell [36] tried to correlate thermal shock resistance of rocks, defined by Manson and Smith [32,33] as $S_t/E\alpha$, with the piercing rate R. Thermal shock resistance was determined by cyclically heating 25x25x100 cm rectangular bars of brittle materials to 550°C and then quenching them in water at room temperature to half the specimen's height. Thermal diffusivity and thermal expansion were experimentally measured as functions of temperature. Thermal diffusivity was found to vary less with temperature than with rock type, and thermal expansion to 500°C was found to vary little between rock types, within a range from 2.7 to 4.3 percent per 500°C. A non-linear relationship was found between piercing rate and thermal shock resistance of rocks.

Freeman, Sawdye and Mumpton [20] also experimentally studied the effects of thermal expansion, diffusivity, strength, texture and composition of rocks on their spallability. Rocks containing 20 percent or more quartz were found to be highly spallable. High composition of feldspar, on the other hand, reduces spallability. Granitoid texture indicates good spallability while a high density of fine-grained minerals indicates poor spallability. These petrographic effects are partly reflected in material properties of rocks. Quartz has a high thermal expansion coefficient at rather low temperature (less than 573°C), which

explains good spallability of rocks with high composition of quartz. Fine-grained materials, on the contrary, tend to reduce thermal expansion through slipping and migration. Fine-grained materials also tend to reduce conductivity and diffusivity. High diffusivity was found to correspond to good spallability, to a certain extent. Structure, texture, and composition of rocks also determine their mechanical strength, which was observed to correlate well with spallability. Rocks with strength decreasing with temperature, beginning at low temperature until plastic flow, were found to be highly spallable. The authors also noted that the exposed surface after each spalling was essentially at the bulk temperature of the rock body.

The mechanics of spalling in jet-piercing was qualitatively discussed by Gray [22]. Gray conjectured that for a sudden change in temperature over a circular area, the stress field at the surface is similar to the one due to complete constraint in all radial directions, as long as the thermal layer, the spatial extent over which the temperature rise is non-negligible, is much smaller than the radius of the heated area. Under this condition, the surface stress was given as $\sigma_b = -E\alpha T/(1-\nu)$, and failure would be by shear and correspond to a critical rise in surface temperature independently of heating rate and temperature distribution. Referring to Aleck's work [3], Gray suggested that large compressive stresses over a depth of the order of the thickness of the spall induces high shear at the circumference of the heated area, causing cracks. These cracks then propagate parallel to the surface by shear or tensile failure. Failure by shear explains the bevelled shape of the spalls, as observed by Soles and Geller [51]. Thermal shock resistance was defined as the

temperature rise needed to cause spalling, $S_c(1-\nu)/E\alpha$. This temperature rise was observed to have an average of 235°C for all rocks. In a scaled down test to verify his conjecture, Gray observed that spalling occured at very low increase in surface temperature (61°C) in contradiction to the predicted temperature rise of 107°C. The surface of the freshly exposed surface was predicted to be 99°C, suggesting that the thermal layer would be rather thick in contrast with the on-site observations by Soles and Geller. Spalls collected from the test suggested that fracture surfaces ignore the structure of rocks and were totally determined by the pattern of thermal stress.

Kingery [28] suggested another mode of spalling based on crack propagation, which depends on the depth of crack required to release strain energy, according to Griffith's criterion. Under this assumption, spall depth is expected to be proportional to the reciprocal of strain energy. If this depth is too large, the crack will not propagate and spalling will not occur. The effects of material properties on thermal stress resistance, defined as $kS_t(1-\nu)/E\alpha$, were also studied experimentally. A high thermal conductivity was found desirable in cooling. However, in heating, high conductivity reduces compressive and shear stresses at the surface but at the same time increases tensile stress inside the body. At a high rate of heat transfer, the effects of thermal conductivity on thermal shock resistance was reported to be negligible. The thermal expansion coefficient and Poisson's ratio were almost invariant with temperature. The modulus of elasticity, on the other hand, tended to decrease at high temperatures. At still higher temperatures,

plastic or viscous flow might take place, changing the stress state drastically.

Thirumalai [56] substantiated experimental data with analytical results for the problem of jet piercing. His analytical model assumed a semi-infinite geometry and one-dimensional temperature, resulting in plane stress, with zero stress in the direction parallel to heat flow. This model implies failure by shear, which arises due to the bending moment created by differential expansion of the material. Experiments on Sioux quartzite, charcoal granite, and Dresser basalt gave surface temperatures at spalling between 167 and 350°C, which were in average about 30 percent lower than the predicted values. Themal layers at spalling were measured to range from 0.7 to 3.2 mm. Micrographs of spall surfaces showed smooth areas of failure, suggesting failure by shear. Inelasticity was observed to reduce stress but experimental data were too scarce to obtain a definite conclusion.

An analytical model was considered by Aleck. In his much cited paper [3], Aleck offered an approximate solution to thermal stresses in a finite rectangular plate clamped along an edge, induced by a uniform temperature rise in the body. An implicit assumption of free expansion in the direction normal to the clamped edge was made, which is not true in most practical cases. The analytical results confirm Saint Venant's principle, predicting that boundary effects are not more than several times the characteristic dimension of the body, which in this case is the geometrical dimension normal to the clamped edge. Aleck's work has been used by many authors to justify their assumption of semi-infinite geometry in thermo-elastic problems of jet piercing.

Jaunzemis and Sternberg [27] were among the few who analytically studied the case of confined heating. Their model consists of a semi-infinite body whose surface was suddenly brought to temperature ΔT over a confined strip, the remaining part of the surface being insulated. Numerical results showed that lateral stresses (normal to heat flow) on the surface are compressive and decrease in magnitude with time. This compressive surface stress could be approximated in the limit as $-E\alpha\Delta T$ only right after the change in surface temperature. This suggests that the assumption made in many previously mentioned papers is valid only at very small times. Longitudinal stresses along the central axis are tensile and have a maximum at a depth of approximately half the width of the heated strip. The location of this maximum stress is almost invariant over a large range of Fourier numbers, from 0 to 100. Numerical results also show that, at a depth of half the width, tensile longitudinal and lateral stresses change roles as the dominant stress as time increases.

Becker [5] extended Jaunzemis' and Sternberg's work in studying stress concentration in thermal shock fields. His analysis shows that $\alpha E\Delta T$ is an upper bound to thermal stresses in a filleted notch subjected to a sudden change in surface temperature of ΔT, if stress penetration is less than half the radius of the notch. Under this condition, it is also shown that the stress field is essentially confined to a boundary layer of thickness independent of boundary shape. This implies that discontinuities in the thermal stress field results in stress amplification much less than it would in a mechanical stress field. Experimental inspection of the stress pattern in notches supports those conjectures.

Chang et al. [12] used a finite element model to analyze thermal stresses induced by a linear change in surface temperature of segmented thick-walled refractory bricks. One dimensional temperature and plane stress were assumed. At moderate heating rates, biaxial tensile stresses developed with their magnitude proportional to the rate of heating. At higher heating rates, maximum tensile stress was found to occur parallel to the heated surface. It can be observed that the location of this maximum tensile stress is at a depth of about half the width of the heated surface, and moves deeper into the body very slowly with time. The authors suggested that higher diffusivity would improve thermal resistance to spalling, in agreement with Norton.

As can be seen, the literature on thermal spalling is scarce and scarcer still is the literature directly related to jet piercing. Furthermore, no definite theory on thermal spalling has been formulated. Although in quenching experiments most authors agree that failure occurs in tension there are divided opinions on the mode of failure of brittle materials in heating. Some authors conjecture that failure during heating is by shear. Some suggest that it is by tensile stress parallel to the direction of heat flow. Some others suggest failure by tensile stress normal to the direction of heat flow. Some authors extrapolate the observations of failure behavior in cyclical quenching and heating experiments to jet piercing. It should be noted, however, that the test conditions in those experiments are very much different from the actual conditions in jet piercing found in practice. On the other hand, most conjectures use the same assumptions of one-dimensional temperature and plane stress. These assumptions have not been analytically verified and

are subject to debate. The definition of thermal shock resistance, which includes the factors affecting fracture behavior, is also a controversial issue. In most cases, the controversy is over the contribution of thermal conductivity and thermal diffusivity to thermal shock resistance. Thermal spalling, especially in jet piercing, is therefore still an open field requiring more research.

III. THE TECHNIQUE OF FICTITIOUS BOUNDARY CONDITIONS

In this chapter the technique of fictitious boundary conditions is proposed as a novel approach to solving heat-conduction problems with moving boundaries and/or with sudden changes in boundary conditions. The general concept is first presented based on an overview of similar existing techniques. The technique is then derived for a general one-dimensional heat-conduction problem of finite dimension. The technique is next evaluated in terms of accuracy and computing time, compared to other techniques, based on a case study. The merits of the technique are further illustrated with two simple examples. Finally, a general discussion of the technique offers more insight into the working of the technique, its limitations, and its possible application to more complicated problems.

1. GENERAL CONCEPT

In heat transfer as well as in many other applications, transforming the original problem into an equivalent problem but different in form may yield a more suitable form of solution, or may suggest a more preferrable solution technique. The most common and simple of such transformations is linear superposition [4] used to separate a linear differential equation with n non-homogeneous boundary conditions into n complementary problems each having at most one non-homogeneous boundary condition.

A more elaborate technique also based on the concept of linear superposition is discussed by Ozisik [45], in connection with ablation problems where the two phases (liquid and solid) were modeled as the two regions of a composite body. By transferring the boundary condition at the common boundary into the partial differential equation, Ozisik proved that a common solution for both regions could be obtained with the use of Green's functions.

A similar concept is discussed by Boley [8], with the use of the technique of superposition and imaging of heat sources and sinks. Boley pointed out that in problems where the thermal properties are constant, and the body is either infinite or bounded by plane surfaces, the solutions can be obtained by formulating the boundary values as heat sources or sinks. In particular, a constant condition at the boundary can be simulated by introducing mirror images of the actual heat sources or sinks. These fictitious sources or sinks again require further mirror images to balance their fictitious effects, and so on, resulting in a converging infinite series (Poisson's series) of fictitious sources and sinks.

The same concept leads further to a novel approach to solve ablation problems: the embedding technique, first discussed by Boley in references [6,7]. In this approach, the body with changing boundary is thought of as being embedded in a fictitious body with unchanged geometry that is the same as the original geometry of the actual body. A fictitious boundary condition is then introduced at the unchanged boundary of the fictitious body so as to produce a temperature distribution that is the solution to the actual problem. Using this technique to solve a melting

and solidification problem, Boley [6,7] assumed the fictitious boundary condition to be expressible in the form of a power series in which the coefficients are determined so as to produce the actual condition at the newly exposed boundary. The merits of this technique is to convert a problem with changing geometry to one with fixed geometry, the solution of which may be obtained by any suitable conventional technique.

Unlike ablation problems, where the rate of change of the boundary is an inherent part of the problem, problems of repetitive spalling have their boundary locations and conditions changing as step functions of time that, in general, cannot be determined from the problem itself but must be determined from a coupled problem. For instance, in problems involving spalling due to thermal stresses, the time and location of spalling are determined by a critical value in the stress field. Therefore, the above methods are not readily applicable to this type of problem.

The exact solution to this type of problem can be obtained by many existing techniques [4,46] by formulating the residual temperature from the previous thermal phase--time between step changes in boundary locations or conditions--as the initial condition of the present thermal phase. However, in cases where the geometry or the heating regime at the boundary is different from one thermal phase to the next, the principle of orthogonality of eigenfunctions does not apply. The exact solution will have the form of multiply nested infinite summations for finite geometry or multiply nested integrals for infinite geometry. This form of the solution is computationally unattractive because the computing time and cost tend to increase geometrically with the order of nesting. The round-off errors also build up with the number of computations performed

and will eventually become a cause for concern as more thermal phases are considered.

One possible approach to reduce the number of computations is to approximate the initial condition by a curve-fitting function. However, in this case the accumulated truncation errors due to the approximations may become excessive, as shown in a later section.

It is therefore necessary to seek an alternate technique which gives an approximate but highly accurate solution which is more computationally efficient. Here we propose the technique of fictitious boundary conditions, of which the truncation and round-off errors are much less than those of both the above approaches. The underlying idea is to reformulate the original problem such that the solution consists of non-nested summations or integrals, i.e., each additional thermal phase contributes additively to the existing solution. In this form, the number of computations only grows linearly with the number of thermal phases considered. The reformulation involves the separation of the original problem in any thermal phase after the first into two complementary problems with one of them forced to be the continuation of the solution from the preceding thermal phase by way of fictitious boundary conditions. The remaining complementary problem then represents the additive effects of the present thermal phase upon the solution from the previous thermal phase. In other words, linear superposition is performed across thermal phases, or in time, whereas it is in space in the other techniques mentioned above.

It is important to remind ourselves that since it is based on the concept of linear superposition, the technique is only applicable to

linear heat-conduction problems, i.e., those represented by linear differential equations with linear boundary conditions.

2. GENERAL DERIVATION

In this section, the Technique of Fictitious Boundary Conditions is derived for a one-dimensional finite geometry. A finite geometry is considered because it encompasses the infinite and semi-infinite cases, if the appropriate dimensions are made large enough and the boundary conditions compatible with those at infinity. The technique is readily applicable to multi-dimensional problems but with less accuracy.

Let us consider a one-dimensional problem in heat conduction given by (Fig. 3.1.a)

$$\frac{\partial^2}{\partial x^2}T_1(x,t) + \frac{1}{k}\, g_1(x,t) = \frac{1}{\kappa}\cdot\frac{\partial}{\partial x}T_1(x,t)\ ,\ 0 \le x \le L,\ 0 \le t, \qquad (3.2.1.a)$$

subjected to the following boundary and initial conditions:

$$- k_0\frac{\partial}{\partial x}T_1(x,t) + h_0T_1(x,t) = \phi_1(t),\ \text{at } x = 0, \qquad (3.2.1.b)$$

$$k_L\frac{\partial}{\partial x}T_1(x,t) + h_LT_1(x,t) = \psi_1(t),\ \text{at } x = L, \qquad (3.2.1.c)$$

$$T_1(x,t) = T_0(x),\ \text{at } t = 0, \qquad (3.2.1.d)$$

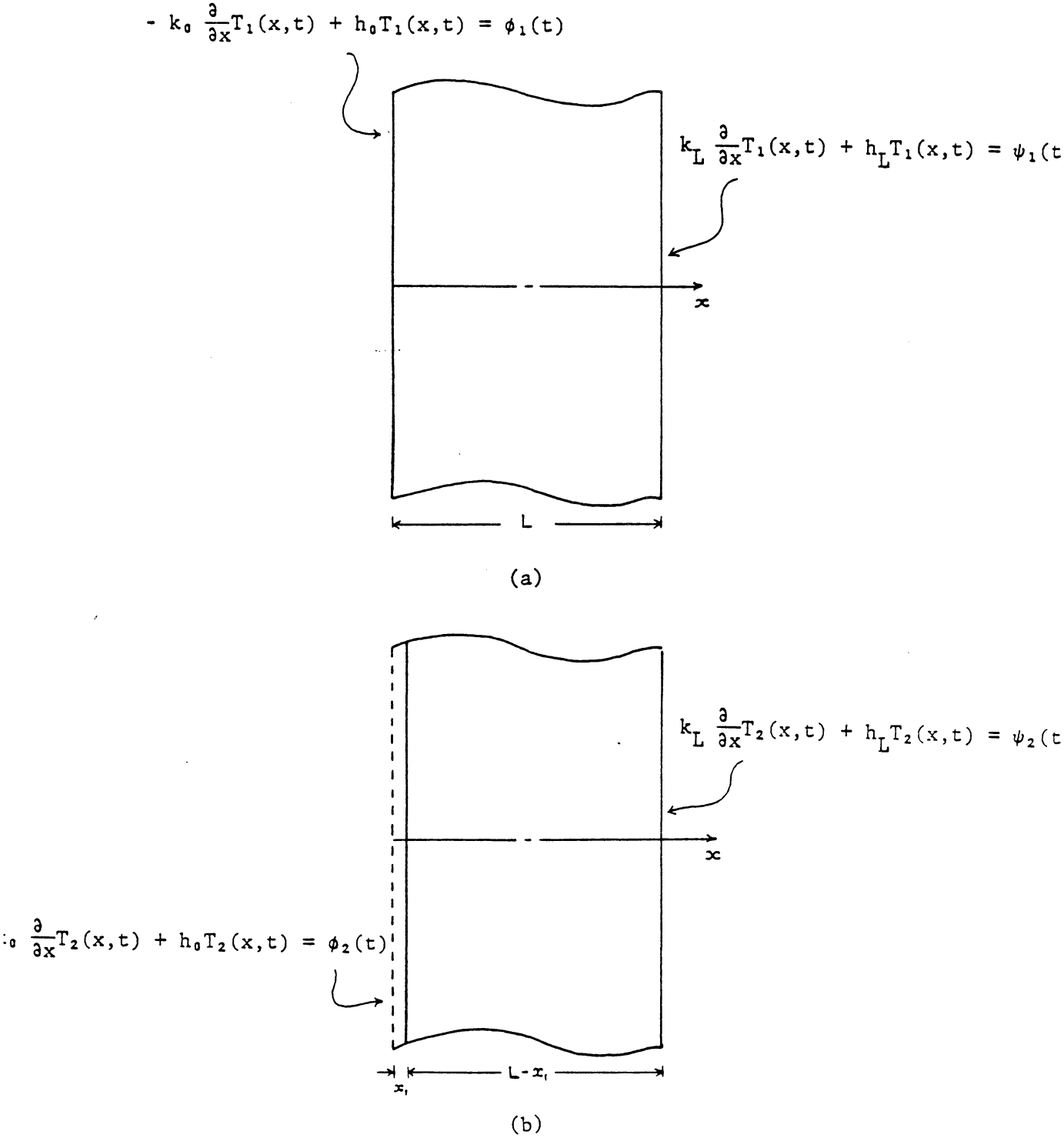

Figure 3.1 Illustration of the heat-conduction problem: (a) before first spalling and (b) after first spalling.

where $\phi_1(t)$ and $\psi_1(t)$ are arbitrary functions of time, and k_i, h_i, for i = 0, L, are evaluated at the boundaries. Thermal properties without subscript refer to the bulk properties of the material.

The solution of the above problem can be obtained from many conventional techniques [4,10,36,38]. However, the form of solution obtained by integral transform [46] is preferred because of its generality, and is given in the following form:

$$T_1(x,t) = \sum_{m_1=0}^{\infty} e^{-\kappa\beta m_1^2 t} K(\beta m_1,x).[\bar{F}(\beta m_1) + \int_0^t e^{\kappa\beta m_1^2 t'} A_1(\beta m_1,t').dt'], \tag{3.2.2.a}$$

where

$$\bar{F}(\beta m_1,t') = \int_0^L K(\beta m_1,x')\ T_0(x')dx' \tag{3.2.2.b}$$

and

$$A_1(\beta m_1,t') = \frac{\kappa}{k}\int_0^L K(\beta m_1,x')\ g_1(x',t')dx' + \frac{\kappa}{k_0}[K(\beta m_1,0)\ \phi_1(t')] + \frac{\kappa}{k_L}[K(\beta m_1,L)\ \psi_1(t')]. \tag{3.2.2.c}$$

$K(\beta m_1,x)$ are the eigenfunctions associated with the eigenvalues βm_1, and is given in general form as:

$$\tan(\beta m_1,L) = -\frac{\beta m_1 (H_0 + H_L)}{\beta m_1 - H_0 H_L}, \tag{3.2.3.a}$$

and

$$K(\beta m_1,x) = \frac{\beta m_1 \cos(\beta m_1 x) + H_o \sin(\beta m_1 x)}{[(\beta m_1^2 + H_o^2)(L + H_L/(\beta m_1^2 + H_L^2)) + H_o^2]}, \qquad (3.2.3.b)$$

where

$$H_0 = \frac{h_0}{k_0}, \qquad (3.2.3.c)$$

and

$$H_L = \frac{h_L}{k_L} . \qquad (3.2.3.d)$$

In Equation (3.2.2.c) when $k_i = 0$, for $i = 0, L$, $(\alpha/k_i)K(\beta m_1,x_i)$ is replaced by $(1/h_i)(dK(\beta m_1,x_i)/dx)$.

Simplified expressions for the eigenfunctions and eigenvalues depend on the kind of boundary conditions involved and are given in [36] for different kinds of boundary conditions.

The initial temperature will be assumed to be uniformly zero, i.e., $T_0(x) = 0$, which simplifies the solution without loss of generality. Now suppose that at time $t = t_1$, the boundary at $x = 0$ is moved to $x = x_1$ with a new boundary condition $\phi_2(t)$, as shown in Fig. 3.1.b. The boundary condition at $x = L$ is changed to $\psi_2(t)$ but the location of the boundary is assumed unchanged. This assumption is not necessary but simplifies the mathematics. The initial condition in the new thermal phase is the solution of the preceding problem evaluated at time $t = t_1$, that is, at the end of the preceding thermal phase.

Assuming constant thermal properties, the problem is now formulated as:

$$\frac{\partial^2}{\partial x^2} T_2(x,t) + \frac{1}{k} g_2(x,t) = \frac{1}{\kappa}.\frac{\partial}{\partial t} T_2(x,t), \; x_1 \le x \le L, \; t_1 \le t, \quad (3.2.4.a)$$

subjected to the following conditions:

$$-k_0\frac{\partial}{\partial x}T_2(x,t) + h_0 T_2(x,t) = \phi_2(t), \text{ at } x = x, \quad (3.2.4.b)$$

$$k_L\frac{\partial}{\partial x}T_2(x,t) + h_L T_2(x,t) = \psi_2(t), \text{ at } x = L, \quad (3.2.4.c)$$

$$T_2(x,t) = T_1(x,t), \text{ at } t = t_1 \; . \quad (3.2.4.d)$$

The exact solution for the above problem will be of the same form as Equation 3.2.2.a with non-zero initial condition $T_1(x,t_1)$. Anticipating that the exact solution for the n^{th} thermal phase will be in the form of n-tuply nested summations, the numerical solution of which is prohibitive in computing time, we will derive an approximate solution based on the technique of fictitious boundary conditions.

With this technique, the solution to Equation 3.2.3 is thought of as the superposition of two complementary solutions, that is,

$$T_2(x,t) = T_2'(x,t) + T_2''(x,t) \quad (3.2.5)$$

where $T_2'(x,t)$ is the solution of

$$\frac{\partial^2}{\partial x^2}T_2'(x,t) + \frac{1}{k}\, g_1(x,t) = \frac{1}{\kappa}.\frac{\partial}{\partial t}T_2'(x,t),\ x_1 \le x \le L,\ t_1 \le t, \qquad (3.2.6.a)$$

subjected to the boundary and initial conditions:

$$-k_0\frac{\partial}{\partial x}T_2'(x,t) + h_0T_2'(x,t) = -\,k_0\frac{\partial}{\partial x}T_1(x_1,t) + h_0T_1(x_1,t),\ \text{at } x = x_1, \qquad (3.2.6.b)$$

$$k_L\frac{\partial}{\partial x}T_2'(x,t) + h_LT_2'(x,t) = k_L\frac{\partial}{\partial x}T_1(L,t) + h_LT_1(L,t),\ \text{at } x = L, \qquad (3.2.6.c)$$

$$T_2'(x,t) = T_1(x,t),\ \text{at } t = t_1, \qquad (3.2.6.d)$$

and $T_2''(x,t)$ is the solution of

$$\frac{\partial^2}{\partial x^2}T_2''(x,t) + \frac{g_2(x,t) - g_1(x,t)}{k} = \frac{1}{\kappa}.\frac{\partial}{\partial t}T_2''(x,t)\ ,\ x_1 \le x \le L,\ t_1 \le t, \qquad (3.2.7.a)$$

with boundary and initial conditions:

$$-\,k_0\frac{\partial}{\partial x}T_2''(x,t) + h_0T_2''(x,t) = \phi_2(t) + k_0\frac{\partial}{\partial x}T_1(x_1,t) - h_0T_1(x_1,t) \quad \text{at } x = x_1, \qquad (3.2.7.b)$$

$$k_L\frac{\partial}{\partial x}T_2''(x,t) + h_LT_2''(x,t) = \psi_2(t) - \psi_1(t),\ \text{at } x = L, \qquad (3.2.7.c)$$

$$T_2''(x,t) = 0,\ \text{at } t = t_1, \qquad (3.2.7.d)$$

In the process, fictitious boundary conditions are introduced at $x = x_1$ and $x = L$ for $T_2'(x,t)$; and the same fictitious boundary conditions

are subtracted from the boundary at $x = x_1$ and $x = L$ for $T_2''(x,t)$. It is obvious that adding Equations 3.2.6 and 3.2.7 term by term will result in Equation 3.2.4.

From the uniqueness theorem for heat conduction problems [8,46], it follows that $T_2'(x,t)$ is identically equal to $T_1(x,t)$, the solution from the preceding thermal phase. A formal proof of the uniqueness theorem for the above problem is given in Appendix A.

The problem is now reduced to the solution of the remaining complementary problem $T_2''(x,t)$.

The exact solution for $T_2''(x,t)$ is again obtained by the integral transform technique, and is given in the following form [46]:

$$T_2''(x,t) = \sum_{m_i=0}^{\infty} e^{-\kappa\beta m_i^2 t} K(\beta m_2,x) \int_{t_1}^{t} e^{-\kappa\beta m_2^2 t'} A_2(\beta m_2,t')dt', \qquad (3.2.8.a)$$

where

$$A_2(\beta m_2,t) = \frac{\kappa}{k} \int_{x_1}^{L} K(\beta m_2,t)[g_2(x',t) - g_1(x',t)]dx'$$
$$+ \frac{\kappa}{k} K(\beta m_2,x_1)[\phi_2(t) + \zeta_2(t)] + \frac{\kappa}{k}[K(\beta m_2,L)\xi_2(t)], \qquad (3.2.8.b)$$

$$\zeta_2(t) = k_0 \frac{\partial}{\partial x} T_1(x_1,t) - h_0 T_1(x_1,t), \qquad (3.2.8.c)$$

and

$$\xi_2(t) = \psi_2(t) - \psi_1(t). \qquad (3.2.8.d)$$

The eigenfunctions and eigenvalues are again given in Equation 3.2.3 with L now replaced by $(L - x_1)$, and x by $(x - x_1)$, i.e., with the spatial origin shifted to x_1.

However, since $\zeta_2(t)$ involves infinite summations, we anticipate that for n thermal phases the exact solution will be in the form of n-tuply nested summations. Therefore, an approximate solution is attempted by approximating $\zeta_2(t)$ as a polynomial or as an exponential function. In most cases an exponential function with three degrees of freedom is satisfactory because the temperature, and hence its derivative, are monotonic in each thermal phase and vary exponentially with time. If the approximation is

$$\zeta_2(t) \cong a_1 + b_1 e^{c_1 t}, \tag{3.2.9}$$

equation (3.2.7) can be expressed as:

$$T_2(x,t) = \kappa \sum_{m_2=0}^{\infty} e^{-\kappa\beta m_2^2 t'} K(\beta m_2, x) \int_{t_1}^{t} [e^{\kappa\beta m_2^2 t'} B_1(\beta m_2, t')]dt' + \frac{\kappa}{k} \sum_{m_2=0}^{\infty} e^{-\kappa\beta m_2^2 t} K(\beta m_2, x_1) B_2(\beta m_2, t'), \tag{3.2.10.a}$$

where

$$B_1(\beta m_2, t) = \int_{x_1}^{L} K(\beta m_2, t)\left[\frac{g_2(x',t) - g_1(x',t)}{k}\right]dx' + \frac{1}{k} K(\beta m_2, x_1)\phi_2(t') + \frac{1}{k} K(\beta m_2, L)\zeta_2(t'), \tag{3.2.10.b}$$

and

$$B_2(\beta m_2,t') = a_1 \frac{e^{\kappa\beta m_2^2 t} - e^{\kappa\beta m_2^2 t_1}}{\kappa\beta m_2^2} + b_1 \frac{e^{(\kappa\beta m_2^2 + c_1)t} - e^{(\kappa\beta m_2^2 + c_1)t_1}}{\kappa\beta m_2^2}.$$

(3.2.10.c)

The constants a_1, b_1, and c_1 can be determined by evaluating $\zeta_2(t)$ at three or more instants in the time interval $[t_1,t]$, which can easily be done knowing the solution for the preceding thermal phase. In practice, an interval larger on both sides than the one to be approximated should be used to reduce the end-effects caused by inaccurate approximation at the end-points of the interval.

If a 3rd degree polynomial is chosen instead, that is

$$\zeta_2(t) \cong a_2 + b_2 t + c_2 t^2, \tag{3.2.11}$$

then the solution is as before with $B_2(\beta m_2,t)$ now taking the form

$$\begin{aligned} B_2(\beta m_2,t) = {} & \frac{e^{\kappa\beta m_2^2 t}}{\kappa\beta m_2^2}\left[(a_2 t^2 + b_2 t + c_2) - \frac{1}{\kappa\beta m_2^2}(2c_2 t + b_2) + \frac{a_2}{\kappa^2\beta m_2^4}\right] \\ & - \frac{e^{\kappa\beta m_2^2 t}}{\kappa\beta m_2^2}\left[(a_2 t^2 + b_2 t + c_2) - \frac{1}{\kappa\beta m_2^2}(2c_2 t + b_2) + \frac{a_2}{\kappa^2\beta m_2^4}\right], \end{aligned}$$

(3.2.12.a)

or in terms of $\zeta_2(t)$ and its derivatives,

$$\begin{aligned} B_2(\beta m_2,t) = {} & \frac{e^{\kappa\beta m_2^2 t}}{\kappa\beta m_2^2}\left[\zeta_2(t_1) - \frac{\zeta_2'(t)}{\kappa\beta m_2} + \frac{\zeta_2''(t)}{(\kappa\beta m_2^2)^2}\right] \\ & - \frac{e^{\kappa\beta m_2^2 t}}{\kappa\beta m^2}\left[\zeta_2(t_1) - \frac{\zeta_2'(t_1)}{\kappa\beta m_2} + \frac{\zeta_2''(t_1)}{(\kappa\beta m_2^2)^2}\right]. \end{aligned} \tag{3.2.12.b}$$

Choosing more degrees of freedom for the approximating functions is possible but hardly justifiable in all the cases considered in this work where three degrees of freedom yield highly accurate results.

The complete solution for the second thermal phase is simply the sum of $T_1(x,t)$ and $T_2''(x,t)$:

$$T_2(x,t) = T_1(x,t) + T_2''(x,t) \tag{3.2.13}$$

for $x_1 \leq x \leq L$ and $t \geq t_1$.

A general solution for both time steps can be written in terms of step functions:

$$T(x,t) = T_1(x,t)u[t] + T_2''(x,t).u[t-t_1] \tag{3.2.14}$$

for $0 \leq x \leq L$ and $t \geq 0$.

The effects of the changes in boundary locations and conditions in the second thermal phase are now represented by $T_2''(x,t)$, which is simply added to the existing solution from the first thermal phase.

The procedure is then repeated for as many thermal phases as necessary. In each thermal phase, the changes may occur either at one boundary or at the other, or at both. The general solution will be of the form

$$T(x,t) = T_1(x,t)u[t] + T_2''(x,t)u[t-t_1] + \ldots + T_n''(x,t)u[t - t_{n-1}]. \tag{3.2.15}$$

Thus, reformulating the original problem by introducing fictitious boundary conditions yields the desired form of the general solution. In the next section, the proposed technique will be evaluated against the exact technique and another approximate technique in terms of accuracy and computational efficiency.

3. EVALUATION OF THE TECHNIQUE

In this section the approximate solution by the technique of fictitious boundary conditions is compared to the exact solution by integral transform and the approximate solution by approximating the initial condition, which we will call the approximate initial condition technique, in terms of accuracy and computing time. This approximate technique gives results equivalent to those of the integral method [44] but is more suitable for comparison with the technique of fictitious boundary conditions. For this purpose, discussion will be based on the case study of the following problem.

An infinite slab of dimension L, initially at a uniform temperature T_0 is suddenly subjected to a constant heat flux q'' at the front face while the back face is kept at T_0. At time t_1, a layer of thickness x_1 is removed and the same heat source is moved to the newly exposed surface. The same process is repeated again and again. The time intervals between removals of the front face material are called thermal phases. The step by step derivation of the solution to this problem by each technique is presented in Appendix C.

For the purpose of comparison, the parameters are arbitrarily chosen as $L = 0.1m$, $q'' = 5.10 \times 10^4 kW/m^2$, $T_0 = 0$. Thermal properties are chosen to be those of granite; namely, the thermal conductivity is chosen to be 2 W/m^oC and the thermal diffusivity to be 10^{-6} m^2/s.

To obtain unbiased comparisons between the techniques, all refinements to enhance the convergence rate or accuracy of one technique are similarly performed on the other techniques.

Figure 3.2 compares the computing times in CPU seconds of the proposed technique and the exact technique as functions of the number of thermal phases. The duration of each thermal phase is arbitrarily chosen to be 1 s and the thickness of the removed material to be 0.001m. The accuracy constraint on the solution by the proposed technique is set to 0.01 per cent, which is good enough for most purposes. It is seen that up to the third thermal phase, the exact method is more efficient because it does not involve any approximation procedure. However, from the fourth thermal phase, it becomes much less efficient than the proposed technique because the nested infinite summations increase the computing time geometrically. Actually, comparison had to be stopped at the fourth thermal phase because one step further is computationally prohibitive. In contrast, the computing time of the proposed technique increases linearly, because each new thermal phase only introduces a simple infinite summation and because the computing time for the approximation remains essentially the same for all thermal phases. For this reason, after the fourth thermal phase, the computing time of the proposed technique only increases linearly with the number of thermal phases considered.

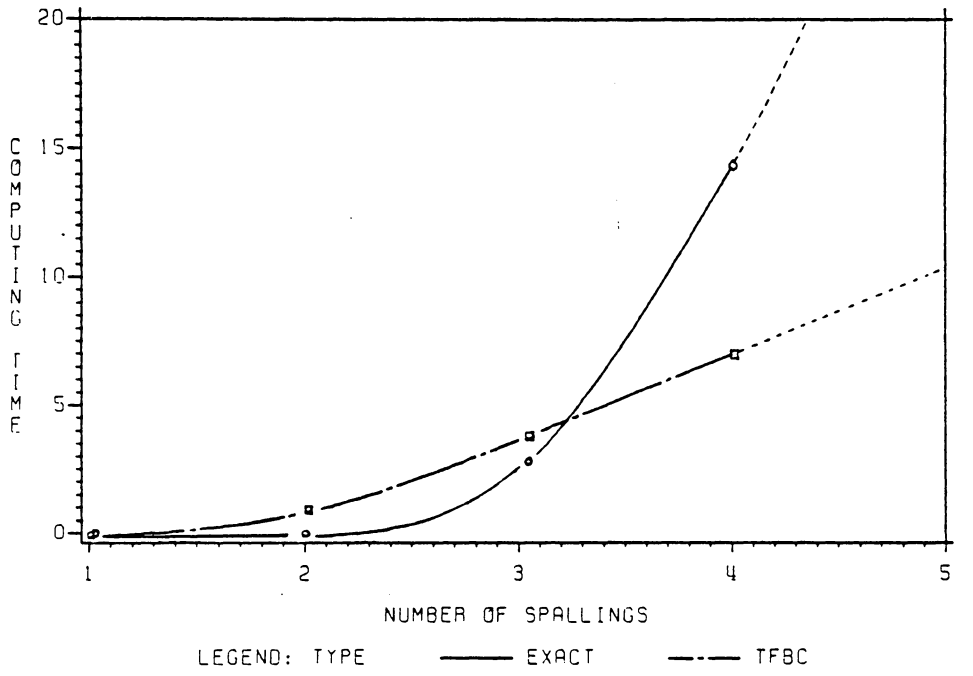

Figure 3.2 Computing times of the exact method and the technique of fictitious boundary conditions (TFBC) in CPU seconds.

Figure 3.3 compares the accuracy of the results of the proposed technique with those by approximating the initial temperature distribution, using the exact solution as reference. For the purpose of comparison, the approximating functions used in both approximate techniques are chosen to be third-degree polynomials. Presented in Fig. 3.4. are temperature distributions in the second thermal phase (after one spalling) at time $t = 2$ s, with $t_1 = 1$ s and $x_1 = 0.001$m, obtained by the three techniques, namely, the integral transform technique--an exact technique, the technique of fictitious boundary conditions, and the approximate initial condition technique. It is seen that even for the case of monotonic temperature distribution the proposed technique is by far more accurate. Actually, in Fig. 3.3 it is not discernable from the exact solution. On the other hand, the approximate solution by approximating the initial condition has large inaccuracies, especially beyond the thermal layer where the approximate solution curves up. Using a higher order polynomial will improve accuracy but would take more computing time. Also the curving up never really disappears.

Figure 3.4.a shows the surface temperature at $t = 20$ s obtained with different methods for different durations of the first thermal phase. It is seen that for large durations the accuracy of the conventional method is improved. This is expected because the temperature distribution gets less non-linear as time passes. In this figure the solution obtained by the proposed method is again indiscernable from the exact solution. The discrepancy between the exact technique and the proposed technique was computed to be 0.5 percent for a thermal phase duration of 1 s and 0.03 percent for a time interval of 10 s. The corresponding values are

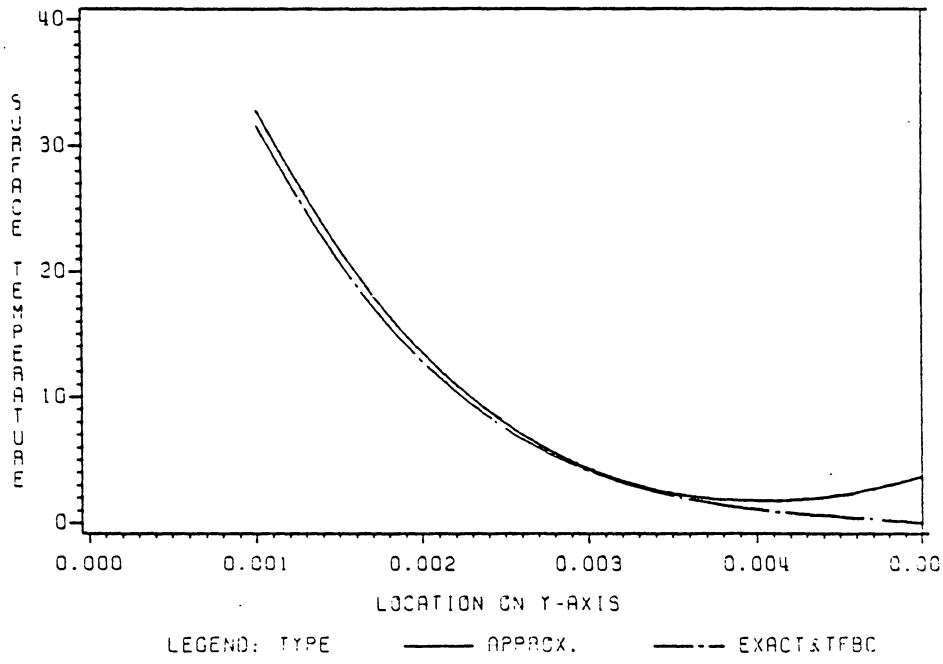

Figure 3.3 Temperature distribution: at t = 20 s in the second thermal phase with first spalling at x_1 = 1.0 mm and t_1 = 1.0 s computed with the exact method, the conventional approximate method, and the technique of fictitious boundary conditions (TFBC).

23.4 and 0.9 percent for the discrepancy between the integral transform technique and the approximate initial condition technique.

Figure 3.4.b shows the surface temperature for a fixed duration of the first thermal phase at different times in the second thermal phase. The error of the approximate initial condition technique increases with time from 3.7 to 5.0 percent over the range of times considered. The error of the proposed technique remains essentially constant at 0.1 percent over the same time range. This agrees with the conjectures previously made.

It should also be noted that the computing time of the proposed technique is slightly less than that of the approximate initial condition technique for the cases considered. This, however, cannot be generalized to other cases.

Numerical results by the above techniques have also been obtained for the problem of sudden changes in boundary conditions with fixed boundary locations. In the first thermal phase, the surface of the same finite one-dimensional object as above is subjected to the same constant heat flux q''. In the next thermal phase, the heat source is removed and the surface is cooled by convection. The results show the same trend as observed for the previous problem, i.e., highly accurate and computationally efficient results have been obtained by the proposed technique.

Actually, the merits of the technique result from the ease of accurately approximating the temperature and its gradient at a fixed location as functions of time with only a few degrees of freedom for the approximating functions. These merits are therefore inherent properties of the technique, developed for heat-conduction problems that can be subdivided

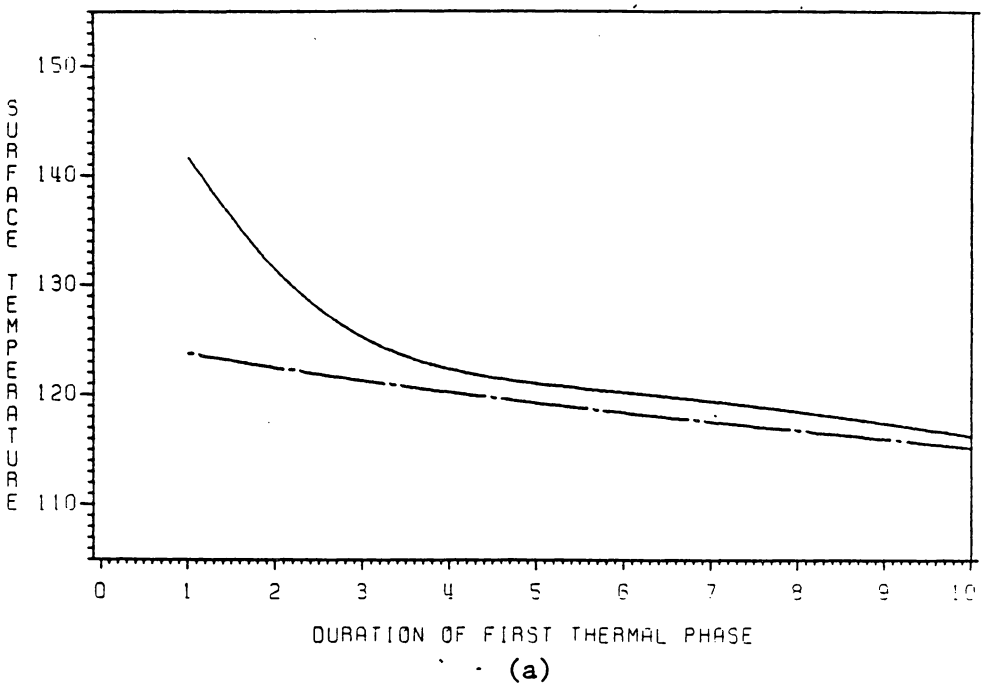

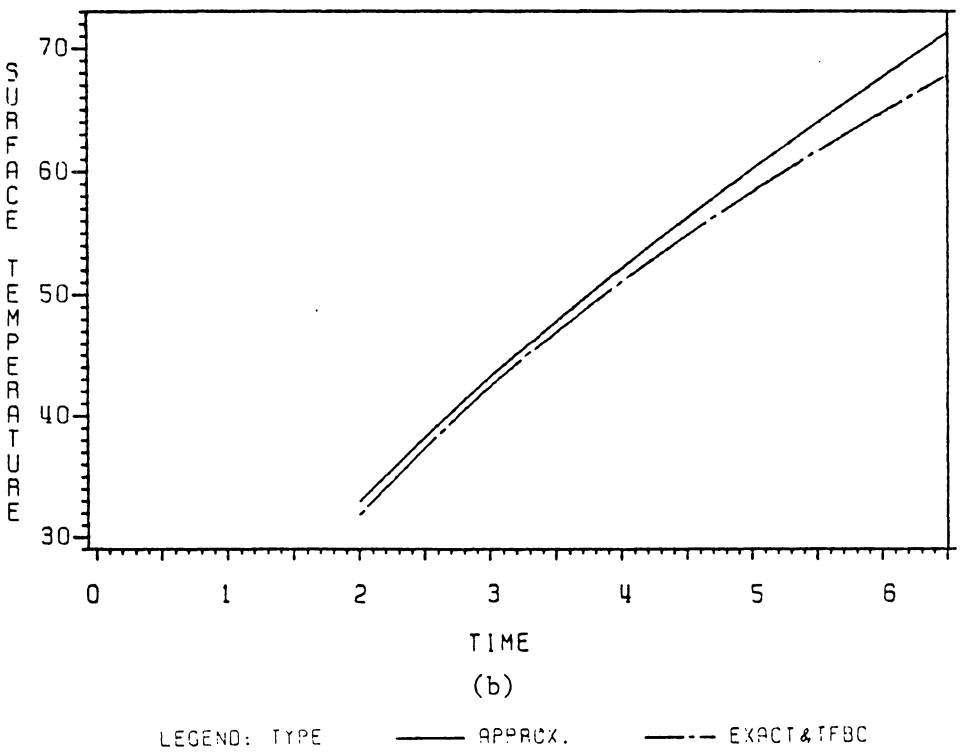

Figure 3.4 Surface temperature computed with different methods: (a) at time t = 20 s in the second thermal phase for different durations of the first thermal phase and x_1 = 1.0 mm, and (b) at different times in the second thermal phase with x_1 = 1.0 mm and t_1 = 1.0 s.

into several thermal phases, no matter whether there is a change in boundary location, boundary condition, or both from one phase to another. This will be discussed in more detail in the discussion.

4. EXAMPLES

Two examples will be presented to illustrate the application of the above technique. The examples will be simple and can be readily solved by existing exact techniques. However, solutions with the technique of fictitious boundary conditions prove to save many steps of derivation, and cast new light on the understanding of the physics of the problem.

4.a Example 1: Let us consider a finite slab with thickness L subjected to a heat flux q" at the surface for time $0 \leq t \leq t_1$ (Fig. 3.4). The problem is formulated as follows:

$$\frac{\partial^2}{\partial x^2}T_1(x,t) = \frac{1}{\kappa}\cdot\frac{\partial}{\partial t}T_1(x,t),\ 0 \leq x \leq L,\ 0 \leq t, \qquad (3.4.1.a)$$

$$-k\frac{\partial}{\partial x}T_1(x,t) = q'',\quad \text{at } x = 0, \qquad (3.4.1.b)$$

$$T_1(x,t) = 0,\quad \text{at } x = L, \qquad (3.4.1.c)$$

$$T_1(x,t) = 0,\quad \text{at } t = 0, \qquad (3.4.1.d)$$

the solution of which is [4]

$$T_1(x,t) = -\frac{2}{L}\cdot\frac{q''}{k}\sum_{m_1=0}^{\infty}\frac{\cos(\beta m_1, x)\ e^{-\kappa\beta m_1^2 t}}{\beta m_1 x} + \frac{q''}{k}(L - x), \qquad (3.4.2.a)$$

where

$$\beta m_1 = \frac{2m_1 + 1}{2L}\pi,\ m_1 = 0,1,2,3,\ldots: \qquad (3.4.2.b)$$

At time $t = t_1$, the heat flux is removed and the surface is suddenly cooled and maintained at T_0 thereafter. The initial condition in this case is the solution from the previous thermal phase evaluated at $t = t_1$ (Fig. 3.4.b). The problem now becomes:

$$\frac{\partial^2}{\partial x^2}T_2(x,t) = \frac{1}{\kappa}\frac{\partial}{\partial t}T_2(x,t)\ ,\ 0 \le x \le L,\ t_1 \le t \le t, \qquad (3.4.3.a)$$

$$T_2(x,t) = T_0, \qquad \text{at } x = 0 \qquad (3.4.3.b)$$

$$T_2(x,t) = 0, \qquad \text{at } x = L \qquad (3.4.3.c)$$

$$T_2(x,t) = T_1(x,t), \qquad \text{at } t = t_1 \qquad (3.4.3.d)$$

The solution for $T_2(x,t)$ can be obtained by decomposing it into two complementary solutions $T_2'(x,t)$ and $T_2''(x,t)$, where $T_2'(x,t)$ is the solution of

$$\frac{\partial^2}{\partial x^2}T_2'(x,t) = \frac{1}{\kappa}.\frac{\partial}{\partial t}T_2'(x,t),\ 0 \le x \le L,\ t_1 \le t, \qquad (3.4.4.a)$$

$$T_2'(x,t) = T_1(x,t), \quad \text{at } x = 0, \qquad (3.4.4.b)$$

$$T_2'(x,t) = 0, \quad \text{at } x = L, \qquad (3.4.4.c)$$

$$T_2'(x,t) = T_1(x,t_1), \quad \text{at } t = t_1. \qquad (3.4.4.d)$$

From the uniqueness theorem, it follows that $T_2'(x,t)$ is identically equal to $T_1(x,t)$ for $t > t_1$.

The complementary problem is given by

$$\frac{\partial^2}{\partial x^2}T_2''(x,t) = \frac{1}{\kappa}.\frac{\partial}{\partial t}T_2''(x,t),\ 0 \le x \le L,\ t_1 \le t, \qquad (3.4.5.a)$$

$$T_2''(x,t) = T_0 - T_1(0,t), \text{ at } x = 0, \qquad (3.4.5.b)$$

$$T_2''(x,t) = 0, \quad \text{at } x = L \qquad (3.4.5.c)$$

$$T_2''(x,t) = 0, \quad \text{at } t = t_1 \tag{3.4.5.d}$$

This problem has solution

$$T_2''(x,t) = \frac{2}{L}\left[\frac{q''}{k}(L - x) + T_0\right] \sum_{m_2=0}^{\infty} \frac{\sin(\beta m_2 x)}{\beta m_2}\left[1 - e^{-\kappa \beta m_2^2 (t - t_1)}\right]$$
$$+ \frac{4}{L^2}\cdot\frac{q''}{k} \sum_{m_2=0}^{\infty} \beta m_2 e^{-\kappa \beta m_2 t} \sin(\beta m_2 x) \sum_{m_1=0}^{\infty} \left[\frac{e^{\kappa(\beta m_2^2 + \beta m_1^2)t} - e^{\kappa(\beta m_2^2 + \beta m_1^2)t_1}}{\beta m_1^2(\beta m_1^2 + \beta m_2^2)}\right] \tag{3.4.6.a}$$

where

$$\beta m_2 = m_2 \pi, \quad m_2 = 0,1,2,3,\ldots \tag{3.4.6.b}$$

By inspection, it is clear that in the above problem, Equation 3.4.6, the effect of the step change in boundary condition is equivalent to an additional step input at time t_1 of magnitude $T_0 - T_1(0,t)$. In this light, the solution for the entire duration can be written as:

$$T_2(x,t) = T_1(x,t)u[t] + T_2''(x,t)u[t-t_1], \tag{3.4.7.a}$$

where $u[t-t_1]$ denotes the step function:

$$u[t-t_1] = \begin{cases} 0 \text{ for } t \leq t_1 \\ \\ 1 \text{ for } t > t_1 \end{cases} \tag{3.4.7.b}$$

It is obvious that for an arbitrary number of thermal phases, the solution is still in the form of a simple summation of step functions. The above example illustrates that the reformulation of the original problem following the technique of fictitious boundary conditions gives a solution for all time in simple form. The merits of the technique are evident even in this simple case. This form of the solution corresponds to the composite solution discussed by Ozisik in reference [45]. However, the former is composite in time instead of in distance as in [45].

4.b Example 2: In this example, a finite slab of size L is successively submerged in fluids at different temperature. The formulation of the problem is given as follows:

$$\frac{\partial^2}{\partial x^2}T_1(x,t) = \frac{1}{\kappa}\frac{\partial}{\partial t}T_1(x,t),\ 0 \le x \le L,\ 0 \le t, \qquad (3.4.8.a)$$

$$-k\frac{\partial}{\partial x}T_1(x,t) + hT_1(x,t) = hT_{W1}\ ,\ \text{at } x = 0, \qquad (3.4.8.b)$$

$$-k\frac{\partial}{\partial x}T_1(x,t) = 0, \qquad \text{at } x = L, \qquad (3.4.8.c)$$

$$T_1(x,t) = 0, \qquad \text{at } t = 0. \qquad (3.4.8.d)$$

The solution of which is given as [37]

$$T_1(x,t) = \frac{h}{k}T_{W1}\sum_{m=0}^{\infty}\frac{K(\beta m,x)K(\beta m,0)}{\beta m^2}[1 - e^{-\kappa\beta m^2 t}], \qquad (3.4.9.a)$$

where

$$K(\beta m,x) = \sqrt{2}\left[\frac{\beta m^2 + H^2}{L(\beta m^2 + H^2) + H}\right]^{\frac{1}{2}}\cos(\beta m(L - x)), \qquad (3.4.9.b)$$

$$\beta m\tan(\beta m,L) = H, \qquad (3.4.9.c)$$

and

$$H = \frac{h}{k} . \qquad (3.4.9.d)$$

At time $t = t_1$, the boundary condition at $x = 0$ is changed to

$$- k \frac{\partial}{\partial x}T_2(x,t) + hT_2(x,t) = h.T_{w2} . \qquad (3.4.10)$$

The initial condition at time $t = t_1$ is $T_1(x,t_1)$.

Again, the solution for the second thermal phase can be decomposed into two complementary parts, $T_2'(x,t)$ and $T_2''(x,t)$. The temperature $T_2'(x,t)$ is forced to be the continuation of $T_1(x,t)$ into the new thermal phase. Then the complementary problem is given by

$$\frac{\partial^2}{\partial x^2}T_2''(x,t) = \frac{1}{\kappa}.\frac{\partial}{\partial t}T_2''(x,t), \qquad (3.4.11.a)$$

$$-k\frac{\partial}{\partial x}T_2''(x,t) + hT_2''(x,t) = hT_{w2} + k\frac{\partial}{\partial x}T_1(0,t) - hT_1(0,t) \quad \text{at } x = 0, \qquad (3.4.11.b)$$

$$\frac{\partial}{\partial x}T_2''(x,t) = 0, \quad \text{at } x = L, \tag{3.4.11.c}$$

$$T_2''(x,t) = 0 \quad \text{at } t = t_1. \tag{3.4.11.d}$$

In this example, since the boundary conditions in both thermal phases are of the same kind and since the bulk temperatures are assumed to be constant, with Equation 3.4.8.b, the boundary condition at x = 0 can be rewritten as:

$$- k \frac{\partial}{\partial x}T_2''(x,t) + hT_2''(x,t) = h(T_{w2} - T_{w1}), \quad \text{at } x = 0. \tag{3.4.12}$$

The solution in the second thermal phase is similar to the one for the previous time step. By inspection, we can deduce that

$$T_2''(x,t) = \frac{h}{k}(T_{w2} - T_{w1}) \sum_{m=0}^{\infty} \frac{K(\beta m,x)K(\beta m,0)}{\beta m^2}[1 - e^{\kappa \beta m^2 t}], \tag{3.4.13}$$

where the eigenfunctions and eigenvalues are the same as before.

The complete solution for the two thermal phases can be given in the following composite form:

$$T(x,t) = T_1(x,t)u[t] + T_2''(x,t)u[t - t_1]. \tag{3.4.14}$$

The effects of cooling in the second thermal phase can be conceptualized as superimposing a convective heat flux of intensity $h[T_{w2} - T_{w1}]$ at time t_1 on the existing heat flux hT_{w1}.

In this problem, the technique of fictitious boundary conditions readily yields the solution to any thermal phase just by inspection. A conventional technique operating by linear superposition in space requires a lengthy procedure with transformation of variables in time for each thermal phase and requires the use of orthogonality properties of the eigenfunctions to reduce the n-tuply nested summations to a simple series of summations. In reference [37], the solution for a specific version of this type of problem is discussed in detail.

The above two examples show that, in cases where orthogonality of the eigenfunctions applies, the proposed technique gives the exact solutions without resorting to the orthogonality principle. The reformulation of the problems also suggests new interpretations of their physical meanings.

5. DISCUSSION

In the above technique, the underlying concept is to introduce fictitious conditions at the boundaries in each thermal phase to account for the residual effects of previous phases, transforming the problem into a linear superposition of problems of the same type, i.e., with zero initial condition. For each new thermal phase, the time and space coordinates are shifted to new origins. The role of the time-varying fictitious boundary conditions is to continuously adjust the transformed problem so as to make its solution identical to that of the original problem. Thus, the fictitious boundary conditions introduced act as memory-prediction functions, in the sense that they memorize past conditions of all pre-

ceding thermal phases and continuously predict the amount of adjustment needed on the transformed problem to make the solutions identical to those of the original problems. In each thermal phase, the fictitious boundary conditions carry information on all past conditions, namely, the boundary conditions, the internal heat generation, the removal of portions of the material with associated internal heat generation, and the effects of moving the boundary conditions to new locations in each phase up to the present phase.

By introducing the fictitious boundary conditions, we need not approximate the initial condition but the temperature or its derivative from the preceding solution at the present boundaries as functions of time. Approximating the fictitious boundary conditions in time has many advantages over approximating the initial condition in space.

Spatial approximation of the initial condition usually requires high-degree or piecewise polynomials, especially at small times when the temperature distribution is highly non-linear [38]. This causes the form of the temperature distribution to vary with time requiring different forms of approximating functions to be used. For example a body suddenly subjected to a high temperature on the surface assumes a high-gradient distribution at first; as time passes, the gradient decreases and finally the distribution becomes linear at steady state. The implication is that no functional form of the approximating function is good over a large time interval. An adequately high-degree polynomial may give good approximation to the temperature distributions at small times, but becomes unnecessary and inefficient at larger times. A low-degree polynomial may be used to improve efficiency but accuracy must be sacrificed at small

times. Also, the goodness of the approximation is time dependent, requiring a minimax optimization of the functional form of the approximating function, i.e., the overall goodness of the approximation is improved by minimizing the maximum error over the whole time interval.

Improvement in efficiency may be obtained by performing the approximation over the thermal layer only. The thermal layer is defined as the spatial interval extending from the surface to a depth having a temperature only negligibly higher than the bulk temperature of the object. However, this still requires the knowledge of the size of the thermal layer, which in turn requires the computation of the temperature distribution over an interval larger than necessary, or requires further derived assumptions on the boundary conditions as done in the integral method [46]. Either way would result in bounds on the amount of improvement achieved as observed by Ozisik [46]. Another drawback of this approach is also noted by Ozisik in the above reference. By using the same approximating function but with different derived boundary conditions, the integral method yields different numerical results.

Another possible problem is the propagating effects of the truncation errors inherent in the approximations. When the approximated initial condition is used to compute temperature at times far from the time where the approximation is done, the accuracy tends to deteriorate.

More severely, approximating the initial temperature distribution in space becomes rapidly more inefficient and inaccurate as the number of flexion points and maxima of the initial distribution increases because the approximating polynomial must be of very high degree. Such temperature distributions are encountered in situations where the material is

cyclically heated and cooled [37]. Even more exotic distributions may exist in situations where the boundaries are subjected to different conditions at the same time, e.g., one surface heated and the other cooled; these boundaries may change erratically with each thermal phase, say the heated surface is next cooled and the cooled surface is removed with the newly exposed surface cooled further. In such cases, the inaccuracy of the solutions may become unacceptable for use in thermal stress analysis because thermal stresses are highly sensitive to small differences in temperature.

The technique of fictitious boundary conditions allows us to avoid most of the above drawbacks by carrying out approximations in time.

With this technique, the approximation does not involve the thermal layer and needs only be performed over an interval from the beginning of each thermal phase up to the time considered, i.e., the interval of approximation is predetermined. Also, the accuracy does not deteriorate with smaller approximation intervals because in the limit we can assume that temperature is linear (in time) over an infinitesimal time interval and use a linear approximation function. This is in contrast with approximating in space which gets worse at small times because of the increasing non-linearity of the distribution. This property makes the technique of fictitious boundary conditions suitable for problems of thermal shock where stresses are more critical at short times after sudden changes in boundary conditions. With larger invervals of approximation, the approximation may become less accurate. However, the contribution of the transient term, the term being approximated, to the solution also becomes smaller. Therefore, the accuracy of the solution tends to remain

essentially invariant or may even decrease with larger approximation intervals.

The accuracy does not deteriorate for temperature at times far from the initial time of each phase, as happens in the conventional approximate method, because approximation is performed over an interval spanning from the beginning of the entire process up to the time considered. The approximation can thus be thought of as being continuously up-dated at each instant of time considered.

Another factor contributing to the higher accuracy of approximations in time is that, except for very peculiar cases, the surface temperature and its derivative are always monotonic in time within a thermal phase. This can be easily seen for the case where the thermal layers corresponding to each boundary do not overlap, that is, the effects of boundary conditions are uncoupled.

By integrating the partial differential equation for the i^{th} thermal phase over the thermal layer, after shifting time and space to the new coordinates,

$$\int_0^{\delta} \frac{\partial^2}{\partial x^2} T(x,t)dx + \frac{1}{k} \int_0^{\delta} g(x,t)dx = \int_0^{\delta} \frac{\partial}{\partial t} T(x,t)dx, \qquad (3.5.1)$$

where δ is the size of the thermal layer. Since $\partial T(\delta,t)/\partial x = 0$, we obtain

$$\frac{\partial}{\partial x} T(0,t) = \int_0^{\delta} \frac{1}{\kappa} \cdot \frac{\partial}{\partial t} T(x,t)dx - \frac{1}{k} \int_0^{\delta} g(x,t)dx. \qquad (3.5.2)$$

The first term on the right-hand-side is the rate of energy absorption by the material at time t and is in general either increasing or

decreasing (or constant) within a thermal phase, as the temperature distribution proceeds towards steady-state. Therefore, when g(x,t) is constant with time, the heat flux $\partial T(0,t)/\partial x$ is always monotonic with time. In the case where g(x,t) varies with time, a thermal phase may be subdivided into sub-intervals, each having the right-hand-side of Equation 3.5.2 monotonic with time.

Following the same line, the temperature at the boundary T(0,t) can be shown to be in most cases monotonic with time. Upon integrating the partial differential equation with respect to time and evaluating it at x = 0, we obtain after rearrangement of terms:

$$T(0,t) = f(0) + \int_0^t \frac{\partial^2}{\partial x^2} T(0,t')dt' + \frac{1}{k}\int_0^t g(0,t')dt', \qquad (3.5.3)$$

where f(0) is the initial condition evaluated at x = 0 and is a constant.

It can be seen that in general the second term on the right-hand-side, representing the net amount of energy transferred to (or from) the surface up to time t, is monotonic in time. If furthermore g(0,t) is constant with time, T(0,t) is monotonic in time. The same subdividing procedure suggested before is applicable in the case of time-varying g(0,t).

Another way to interprete the merits of the technique is to observe the differential equation, Equation 3.2.1.a. This form of the differential equation yields a solution with spatial distribution having the number of maxima and flexion points reduced upon differentiation. In other words, the spatial distribution can be approximated with polynomials. In this case, from the differential equation, it is observed

that the temporal distribution at a fixed point is "smoother" than the spatial distribution, in the sense that the former has fewer maxima or flexion points. This is another explanation why approximating in time is better than in space.

For the above reasons, the truncation errors in the proposed technique are not as large as in the conventional approximate technique. This implies that only simple forms of the approximating functions are needed to obtain highly accurate results. The round-off errors are also much smaller than those in the exact technique due to the reduced amount of computation performed. For the same reason, the proposed technique is computationally more efficient than the exact technique. These are essentially the main reasons for the development of the proposed technique.

The derivation of the technique was intentionally made to be as general as possible. Thermal properties and coefficients at the boundaries may differ from the bulk values of the material. Internal thermal generation can also undergo sudden changes from phase to phase. This allows for the applications of the method presented here to many possible combinations of boundary conditions and thermal generation that may be encountered in reality. Some examples of possible thermal patterns are heating with constant or time-varying heat flux, sudden change in surface temperature, change in surface temperature at constant rate with different rates for each thermal phase, alternating heating and quenching with different quenching temperatures for each thermal phase, etc. The only constraint is that the thermal properties of the material and the ratio h_i/k_i, with i denoting the two boudaries, must be invariant from phase to phase. Actually, the thermal properties may change from one phase to

another but all of them must change by the same factor, resulting in a linear rescaling of the problem. However, this uniform change of the thermal properties is not usually encountered in reality.

The solution is also intentionally derived for a finite geometry because it can be easily extended to the semi-infinite case by letting L go to infinity. In some instances, solutions for semi-infinite problems can be obtained from corresponding finite problems by straightforward routines. Appendix B illustrates such a case.

Although the technique has been derived in one dimension, it is easy to extend the technique to multi-dimensional problems. This can be done by first using the technique of seperation of variables and then applying the technique of fictitious boundary conditions to the resulting one-dimensional problems. However, the compounded truncation errors may become excessive after a certain number of thermal phases.

Other limitations of the proposed technique need to be considered. First, as already mentioned, the technique is limited to linear heat-conduction problems. For instance, in general, it cannot be used with problems involving radiative boundary conditions. Neither can it be used with the problems involving travelling waves. The reason is that, in this case, the spatial distribution does not have fewer maxima or flexion points upon differentiation.

As a final note, we would like to point out the possibility of further transformation of the problem. Namely, the boundary conditions may be transferred into the differential equation in the form of impulse internal thermal generations. This is obvious by considering Equation

3.2.2.c, in which $A_1(\beta m,t)$ represents the joint effects of boundary conditions and internal thermal generation.

Now, if the internal generation $g_1(t)$ is chosen as $(k/k_0)\phi_1(t)\delta(x)$, where $\delta(x)$ is an impulse function at $x = 0$, upon integration we obtain

$$\frac{\kappa}{k}\int_0^L K(\beta m_1,x')\frac{k}{k_0}\phi_1(t)\delta(x')dx' = \frac{\kappa}{k_0}K(\beta m_1,0)\phi_1(t), \tag{3.5.4}$$

where $K(\beta m_1,x)$ is the eigenfunction associated with the eigenvalue βm_1, both of which are given in reference [44] for each specific case.

That is, the boundary condition at $x = 0$ can be replaced by an impulse internal thermal generation of intensity $(k/k_0)\phi_1(t)$. The same is true for the boundary condition at $x = L$. In other words, Equation 3.2.1 can be rewritten as:

$$\frac{\partial^2}{\partial x^2}T_1(x,t) + \frac{1}{k_0}g_1(x,t) + \frac{1}{k_0}\phi_1(t)\delta(x) + \frac{1}{k_L}\psi_1(t)\delta(x-L) = \frac{1}{\kappa}\frac{\partial}{\partial t}T_1(x,t). \tag{3.5.5}$$

In general, the initial condition can be transformed into fictitious boundary conditions, which in turn can be transformed into impulse internal thermal generations in the differential equation. In this manner, all the non-homogeneities can be transferred into the differential equation. This result can also be derived by using Green's functions.

In summary, in this chapter a novel technique to solve heat-conduction problems with moving boundaries and sudden changes in boundary conditions was derived based on the introduction of fictitious boundary

conditions. The merits of the proposed technique were evaluated against those of the integral transform technique and the approximate technique by approximating the initial condition. Numerical results show the proposed technique to give highly accurate results and at the same time to be more computationally efficient compared to the other two techniques. The accuracy of the proposed technique is consistent with time. The basic concepts of the technique are simple and the technique itself is easy to implement. Two examples serve to illustrate the applicability of the proposed technique to different types of problems and its advantages over more conventional techniques even for very simple problems. Finally, the factors contributing to the merits of the technique were discussed along with its possible application in more complicated problems, and its limitations.

IV. THERMAL STRESSES PRODUCED BY UNCONFINED HEATING

In studying thermal spalling of brittle materials, it is common practice to assume that spalling is determined by a single stress component, i.e., either by shear, longitudinal, or lateral stress. Some authors [22,38,39,40] use an infinitely large body with uniform heating as model and consider induced shear stress as the main factor causing failure. Some others [12,32,33,34] work with finite dimensional models and consider longitudinal stress only. In a few papers [12,48], lateral stress is suggested to cause fracture parallel to the direction of heat flow.

Each of the above assumptions have been based on observations and backed up by qualitative discussion. No theoretical justification has been provided.

The main objective of this chapter is to study the individual contributions of each stress component and their combined effects on the risk of rupture of brittle materials, based on the modified Coulomb-Mohr theory of failure. Thermal stresses beyond the first spalling are also considered.

The numerical results show that the longitudinal and lateral, or radial, stresses change role as the dominant factor determining failure. At short times after heating, the tensile lateral stress is considerably larger than the longitudinal stress, except near the edge. As time passes, the tensile longitudinal stress increases rapidly and catches up with the lateral stress. At large time, the longitudinal stress becomes

dominant. Each of the assumptions mentioned above is therefore partially justifiable, depending on each specific problem.

Similar results for a more refined and realistic model will be presented in Chapter V and can be used in design.

1. FORMULATION OF THE THERMO-ELASTIC PROBLEM

The thermo-elastic problem is assumed to be separable into two uncoupled problems, allowing temperature to be computed first and then used to obtain stress. This assumption is especially good for rocks as discussed in reference [8] and illustrated in Appendix B.

The exact solution to the thermal problem is obtained by the technique of integral transform [44,46]. The solution is derived for a finite geometry with repetitive spalling. The model used in this chapter is illustrated in Fig. 4.1. The axi-symmetric object of radius R and length L is initially at ambient temperature T_0. At time t = 0, it is subjected to a constant and uniform heat flux q" over the entire front face. The edge is assumed to be perfectly insulated, resulting in a one-dimensional thermal problem. The length L is assumed to be large enough so as to maintain the back face at the ambient temperature. As for stresses, the only assumption is that of unconstrained boundaries. This assumption simplifies the stress state by reducing the end effects. The trivial assumption of $T_0 = 0$ is also made to simplify the derivation of the solution.

The problem can be formulated as the following differential equation and boundary conditions:

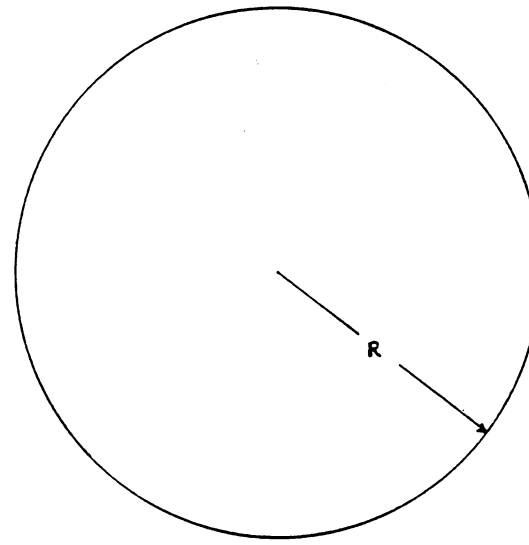

(a)

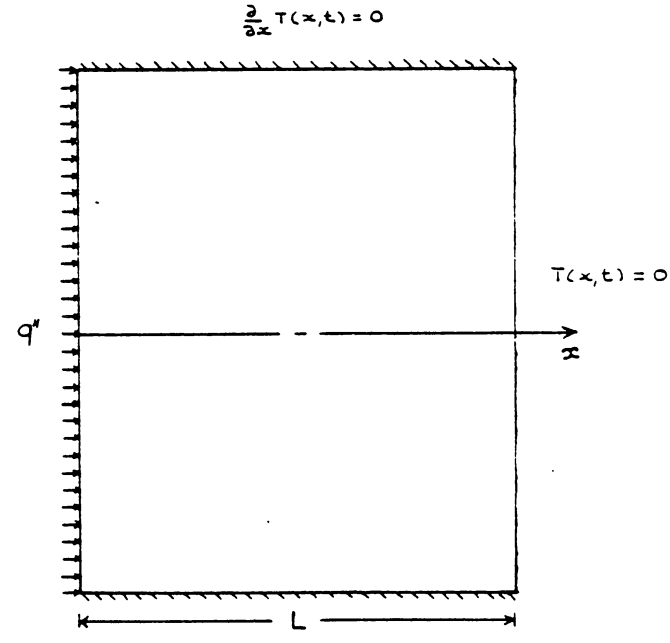

(b)

Figure 4.1 Illustration of the problem: (a) Front view and (b) side view of the axi-symmetric object of radius R subjected to heatflux q", insulated at the edge and the back surface maintained at ambient temperature.

$$\frac{\partial^2}{\partial x^2}T_1(x,t) = \frac{1}{\kappa}.\frac{\partial}{\partial t}T_1(x,t),\ 0 \le x \le L,\ 0 \le t, \qquad (4.1.1.a)$$

$$-k.\frac{\partial}{\partial x}T_1(x,t) = q'', \qquad \text{at } x = 0, \qquad (4.1.1.b)$$

$$T_1(x,t) = 0, \qquad \text{at } x = L, \qquad (4.1.1.c)$$

$$T_1(x,t) = 0, \qquad \text{at } t = 0. \qquad (4.1.1.d)$$

The solution is obtained by the integral transform method, i.e. from Equation 3.1.2, and is expressed as

$$T_1(x,t) = \frac{2}{L}.\frac{q''}{k}\sum_{m_1=0}^{\infty}\frac{(1 - e^{-\kappa\beta m_1^2 t})\cos(\beta m_1 x)}{\beta m_1^2}, \qquad (4.1.2.a)$$

where

$$\beta m_1 = \frac{2m_1 + 1}{2L}\pi, \quad m_1 = 1,2,3,\ldots . \qquad (4.1.2.b)$$

It can be shown that Equation 4.1.2.a can be separated into a steady state solution and a transient solution as follows:

$$T_1(x,t) = \frac{q''}{k}(L - x) - \frac{2q''}{kL}\sum_{m_1=0}^{\infty}\frac{e^{-\kappa\beta m_1^2 t}\cos(\beta m_1 x)}{\beta m_1^2} \qquad (4.1.3)$$

At time $t = t_1$ a thin layer of material of size x_1 is removed and the same heat flux q'' is applied to the new boundary. The temperature distribution at $t = t_1$ is the residual temperature distribution from the

preceding thermal phase. A thermal phase is defined as the time interval between any change in boundary conditions or locations.

The second thermal phase is formulated similarly to the first, with slight modifications:

$$\frac{\partial^2}{\partial x^2}T_2(x,t) = \frac{1}{\kappa}.\frac{\partial}{\partial t}T_2(x,t),\ x_1 \le x \le L,\ t_1 \le t, \qquad (4.1.4.a)$$

$$-k.\frac{\partial}{\partial x}T_2(x,t) = q'', \qquad \text{at } x = x_1, \qquad (4.1.4.b)$$

$$T_2(x,t) = 0, \qquad \text{at } x = L, \qquad (4.1.4.c)$$

$$T_2(x,t) = T_1(x,t), \qquad \text{at } t = t_1. \qquad (4.1.4.d)$$

In the case where the residual temperature $T_1(x,t_1)$ is negligible, the solution for the second thermal phase assumes the same form as that for the first thermal phase, with time and space shifted to t_1 and x_1. On the other hand, if the residual temperature is not small, the technique of integral transform [44] is again applied to obtain the exact solution. The same procedure is repeated for as many times as necessary. The general solution thus obtained for the n^{th} thermal phase is:

$$T_n(x,t) = -\frac{q''}{k}\frac{2^n}{\prod_{i=1}^{n}(L-x_i)}\sum_{m_n=0}^{\infty} e^{-\kappa\beta m_n^2(t-t_{n-1})}[X_n]\sum_{m_{n-1}=0}^{\infty} e^{-\kappa\beta m_{n-1}^2(t_{n-1}-t_{n-2})}[X_{n-1}]$$
$$\cdots \cdot\sum_{m_2=0}^{\infty} e^{-\kappa\beta m_2^2(t_2-t_1)}[X_2]\sum_{m_1=0}^{\infty} e^{-\kappa\beta m_1^2 t_1}[X_1] + \frac{q''}{k}(L - x),$$
$$x_n \le x \le L_1,\ t_n \le t, \qquad (4.1.5.a)$$

where

$$\beta m_n = \frac{2m_n + 1}{2L_n}\pi, \quad m_n = 1, 2, 3, \ldots n-1 \qquad (4.1.5.b)$$

$$[X_i] = \frac{1}{2}\left[\cos(\beta m_i x_i)L_i + \frac{\sin(\beta m_i(2L_i + x_i)) - \sin(\beta m_i x_i)}{2\beta m_i}\right] \qquad (4.1.5.c)$$

for $\beta m_{i-1} = \beta m_i$, or

$$[X_i] = \frac{\sin((\beta m_{i-1} - \beta m_i)L_i)}{2(\beta m_{i-1} - \beta m_i)} + \frac{\sin((\beta m_{i-1} + \beta m_i)L_i)}{2(\beta m_{i-1} + \beta m_i)}\cos(\beta m_{i-1} x_i), \qquad (4.1.5.d)$$

for $\beta m_{i-1} \neq \beta m_i$, and

$$[X_n] = \cos(\beta m_n(x - x_n)). \qquad (4.1.5.e)$$

In the above equations, $[X_1]$ is given in Equation 4.1.5.d but multiplied by $1/(\beta m_1)^2$. For comparison, the approximate solution for the n^{th} thermal phase by the technique of fictitious boundary conditions as developed in Chapter III is given in Appendix C.

The above temperature solution was then used with a finite element model to compute thermal stresses for each thermal phase.

The finite element model consists of an axi-symmetric body of radius R and thickness L. The mesh was designed to be finer in the region near

the central axis. The aspect ratio in this region is maintained below 3. The mesh is less fine in the region towards the edge and the back face, with aspect ratio of less than 7. In each case study, the mesh is gradually refined until the stresses throughout the model change less than 5 percent with successive refinements. This criterion of convergence assures reliable results in the region near the central axis, which is the region of interest.

2. NUMERICAL RESULTS.

In this section the results are presented in non-dimensional form. This is different from common practice in the field of thermal stress. However, in non-dimensional form, the results can be applied to many different problems if they can be reduced to the same type of problem considered here after normalization. The non-dimensionalization of the solutions also facilitate the comparison of different parameters in their contribution to failure, and gives more insight into the role of each factor involved.

Time is non-dimensionalized as $\kappa t/R^2$, which is the Fourier number. Non-dimensional stresses are defined as $(k/q''R)\sigma_i(1-\nu)/E\alpha$ where the subscript i of σ is replaced by r, x, t, and rx for radial, longitudinal, tangential and shear stresses, respectively. The different stress components are illustrated in Fig. 4.2. The term radial stress is used interchangeably with lateral stress in this context. The thermal stress resistance R_{th} is defined as $(k/q''R_q)(S_t(1-\nu)/E\alpha)$. Temperature is non-

dimensionalized as $kT(x,t)/Rq''$. All geometrical dimensions are normalized against R.

The values of R_s and R_{th} used in this chapter are 0.05 and 0.02, respectively.

Three dimensional distributions of each stress component are first plotted at three different times in the first thermal phase to show the separate effects of each component. The combined effects of the stress components are then considered with the use of the failure factor, defined as the inverse of the safety factor used in the modified Coulomb-Mohr theory of failure. A detailed definition of the failure factor is offered in Appendix D. These numerical results form the basis for the discussion on the validity of using a single stress component in the study of spalling as often done in the literature.

Figure 4.3 displays the distributions of radial stress at $t^* = 0.001$, 0.03, and 0.25 respectively. It is seen that shortly after heating, as shown in Fig. 4.3.a, the compressive stress is highly localized to the region near the surface. It is largest on the central axis and decrease towards zero at the edge. At a short distance beneath the surface, the radial stress rapidly becomes tensile and then decreases to zero longitudinally. At a later time, as shown in Fig. 4.3.b, both the compressive and tensile maxima increase in magnitude with the tensile maximum increasing at a greater rate. The stress distribution also becomes rapidly less uniform. The same trend is observed at $t^* = 0.25$, as shown in Fig. 4.3.c.

The tangential stress distributions are plotted in Fig. 4.4. At $t^* = 0.001$, as shown in Fig. 4.4.a, the tangential stress distribution is

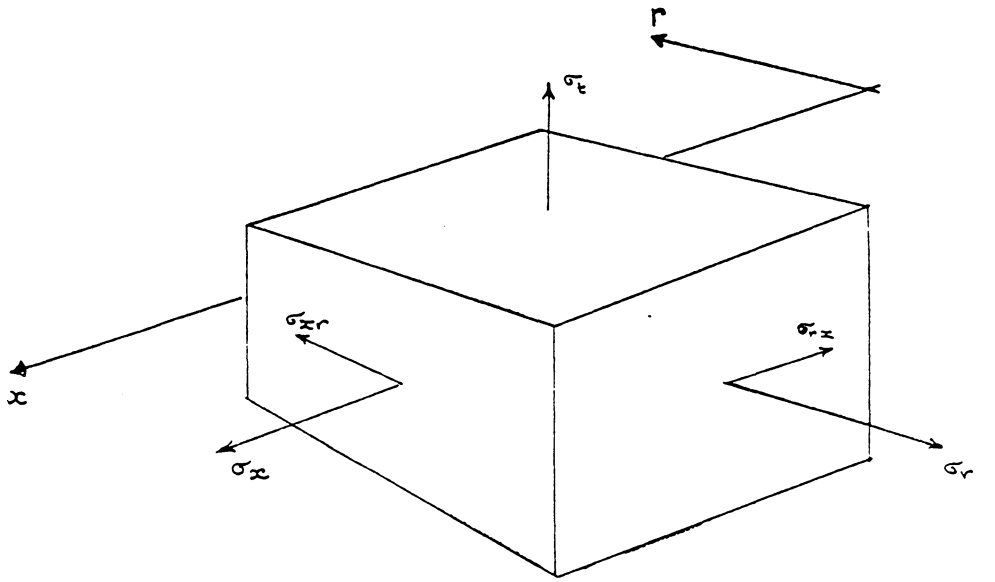

Figure 4.2 Illustration of the stress components: σ_r, σ_t, σ_{rx}, σ_x stand for radial, tangential, shear and longitudinal stresses, respectively.

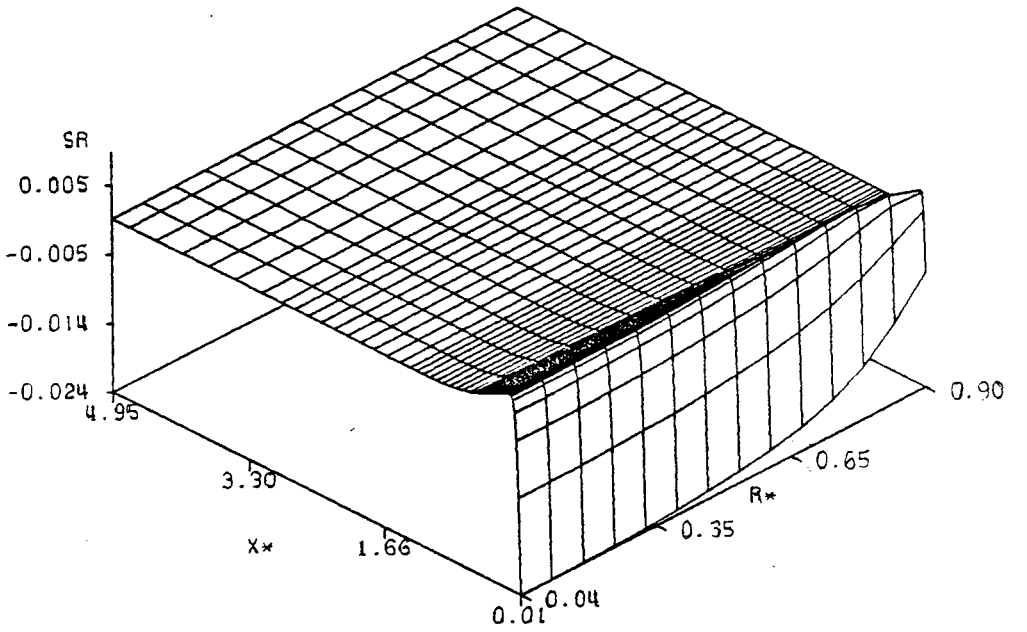

(a)

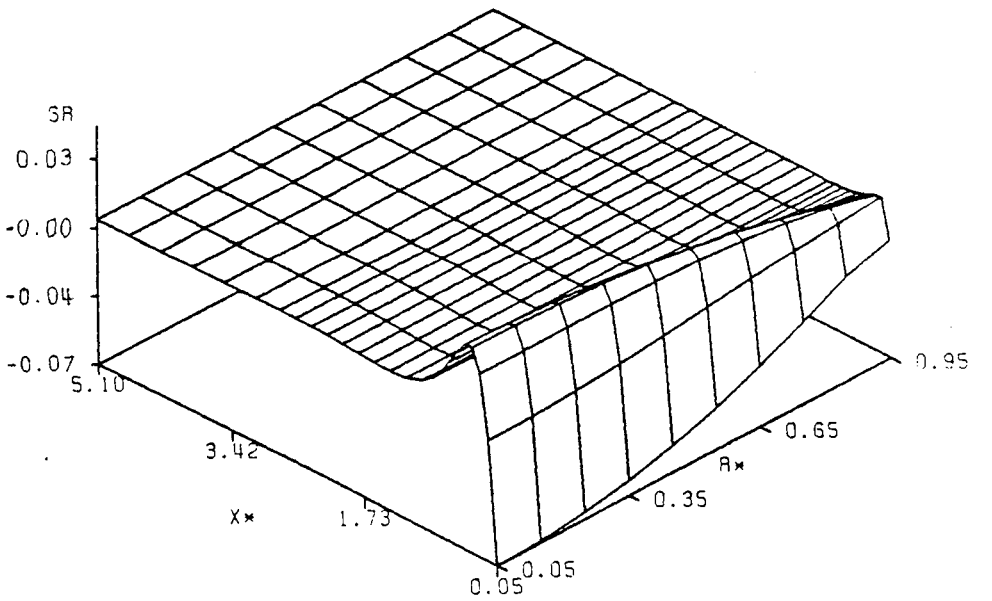

(b)

Figure 4.3 Non-dimensional radial stress: (a) at $t^* = 0.001$, (b) at $t^* = 0.03$, and (c) at $t^* = 0.25$ (next page).

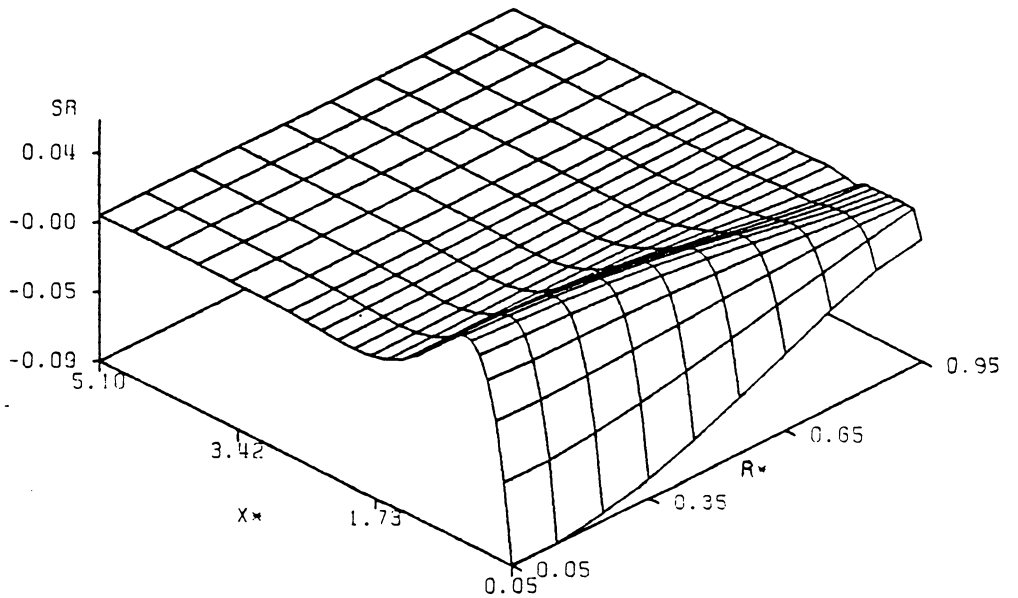

(c)

Figure 4.3 (Continued)

very similar to that of the radial stress, except that the former is radially more uniform. This similarity decreases with time. At $t^* = 0.03$, as shown in Fig. 4.4.b, the tangential stress is considerably more uniform in the radial direction than the radial stress and hence has larger magnitude towards the edge. The same trend is observed in Fig. 4.4.c, i.e., at $t^* = 0.25$. It is noted that along the central axis, the radial and tangential stresses are equal in magnitude.

Similar plots for shear stress are presented in Fig. 4.5. The shear stress distributions are much more complex than those of the other stresses. This reflects the interaction between different stress components. In Fig. 4.5, the shear stress displays a maximum magnitude near the edge and the front face at $t^* = 0.001$. This maximum migrates towards the central axis as time passes, as shown in Fig. 4.5.b and c. There is no shear stress along the central axis.

The longitudinal stress distributions for $t^* = 0.001$, 0.03, and 0.25 are plotted in Fig. 4.6. The longitudinal stress at $t^* = 0.001$, shown in Fig. 4.6.a, displays a region of complex stress state close to the edge. However, the results close to the edge are numerically unreliable due to the assumption of unconstrained boundaries and perfect insulation at the boundaries. In the region far from the edge, the longitudinal stress distribution is rather uniform radially. A positive maximum is observed to be located at about one radius R deep inside the body. Figures 4.6.b and c show that at larger times the radial stress increases more rapidly in magnitude than the other stress components.

An interesting point to note from the above figures is that the location of the maximum longtitudinal stress on the central axis is essen-

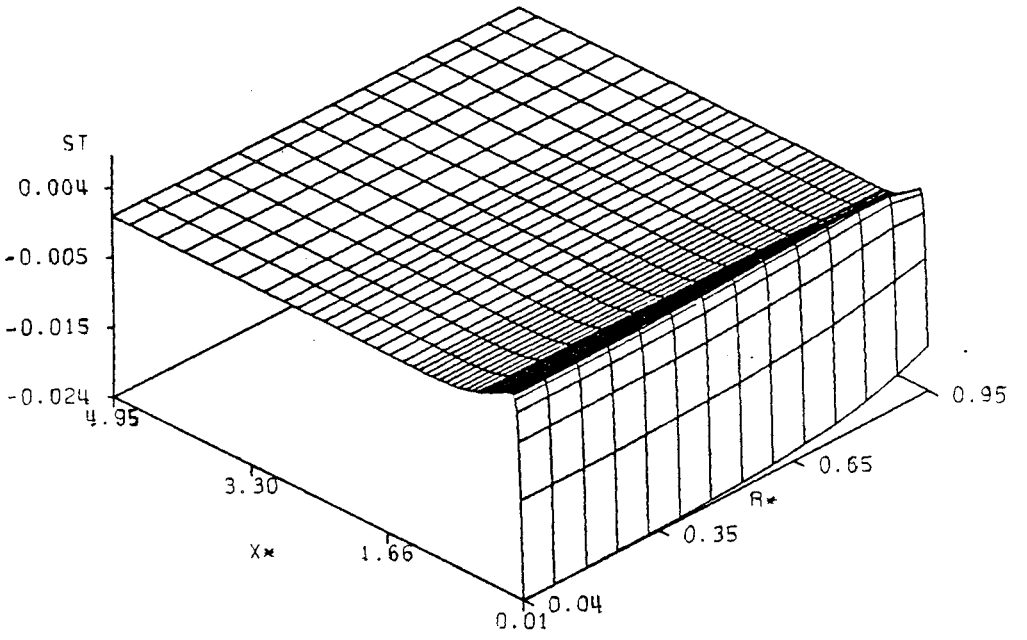

(a)

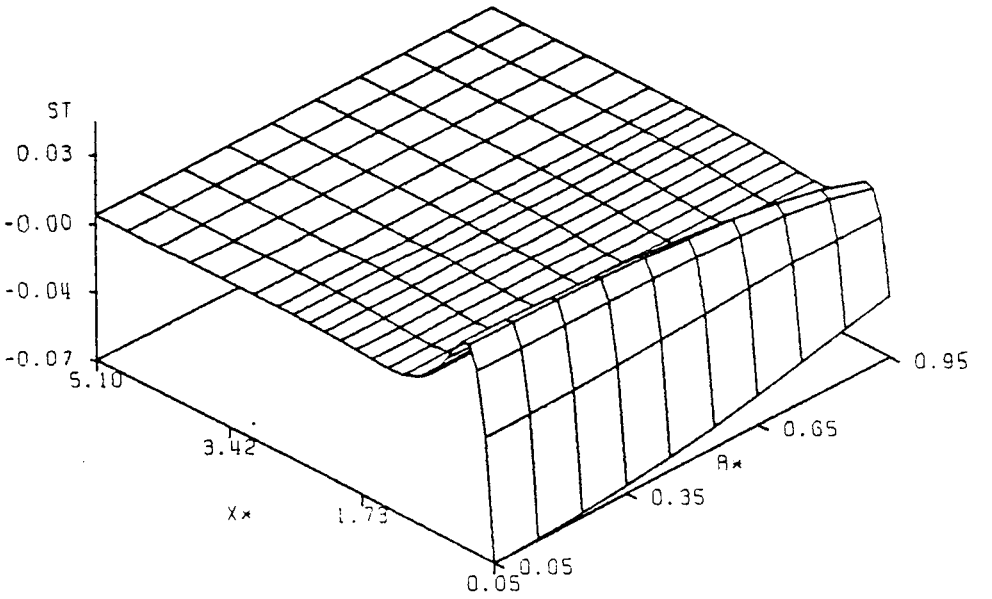

(b)

Figure 4.4 Non-dimensional tangential stress: (a) at t* = 0.001, (b) at t* = 0.03, and (c) at t* = 0.25 (next page).

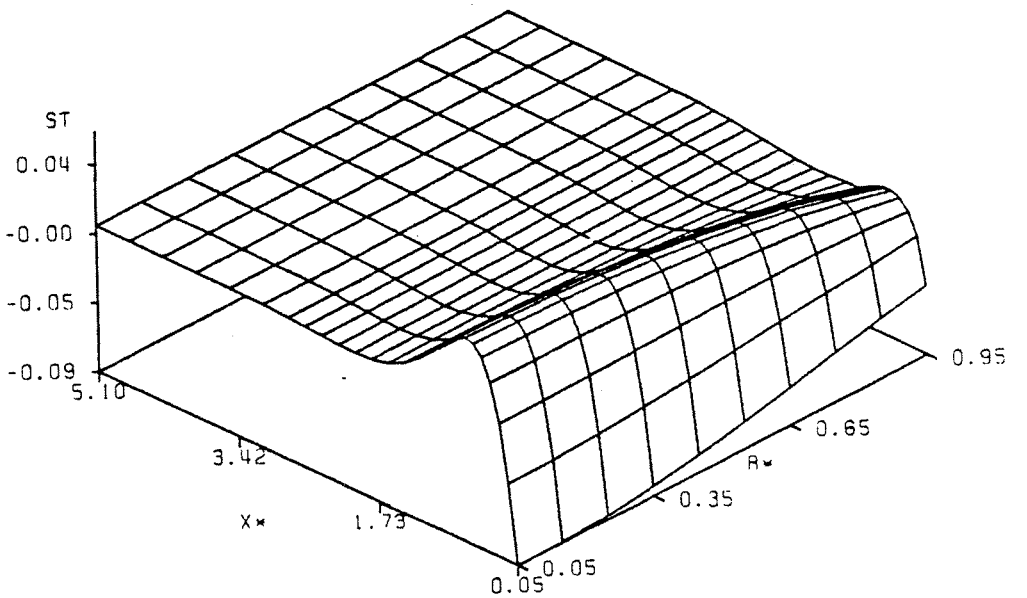

(c)

Figure 4.4 (Continued)

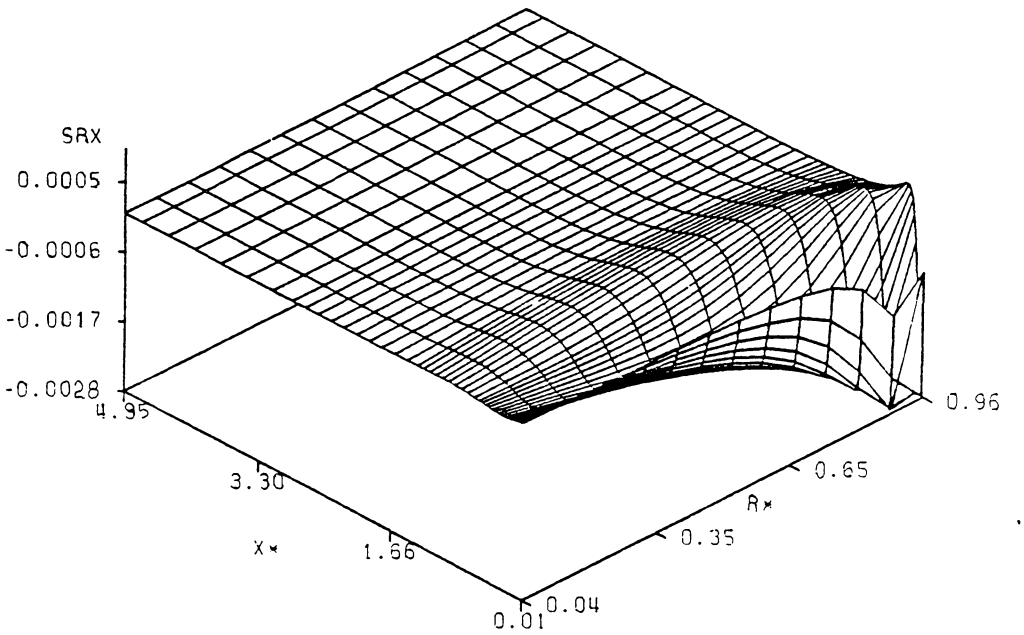

(a)

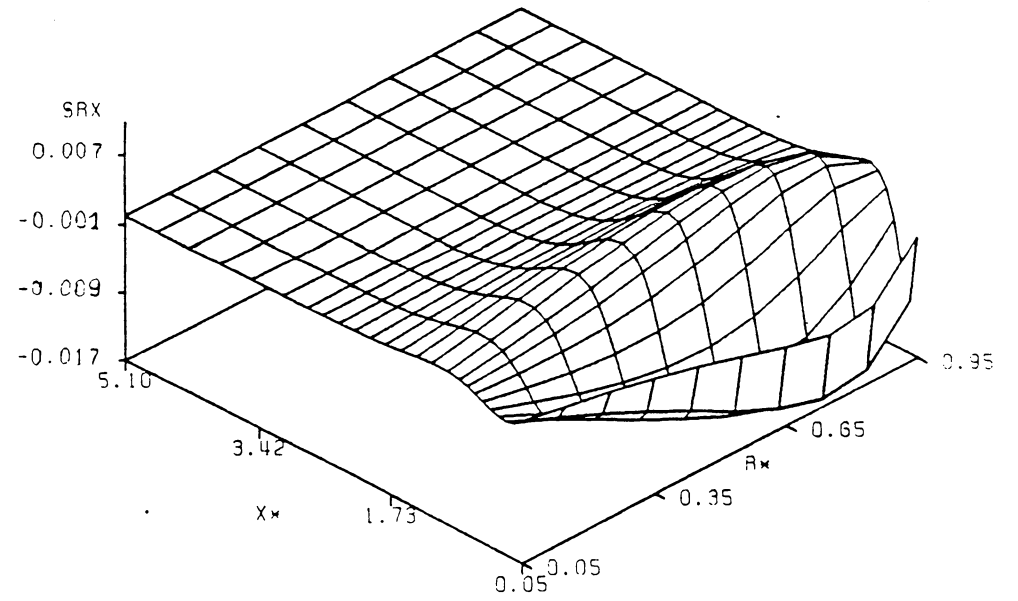

(b)

Figure 4.5 Non-dimensional shear stress: (a) at t* = 0.001, (b) at t* = 0.03, and (c) at t* = 0.25 (next page).

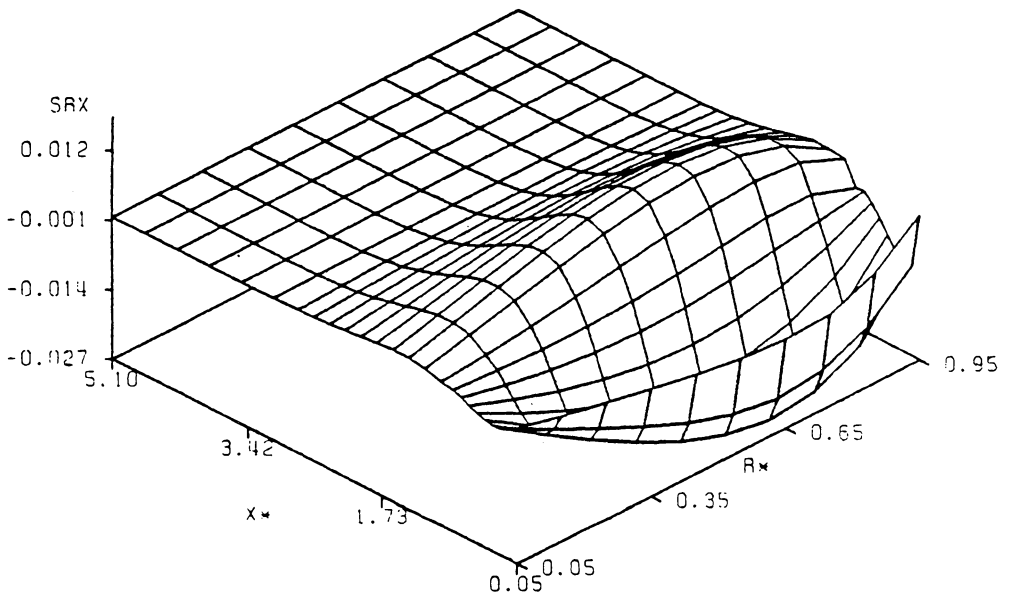

(c)

Figure 4.5 (Continued)

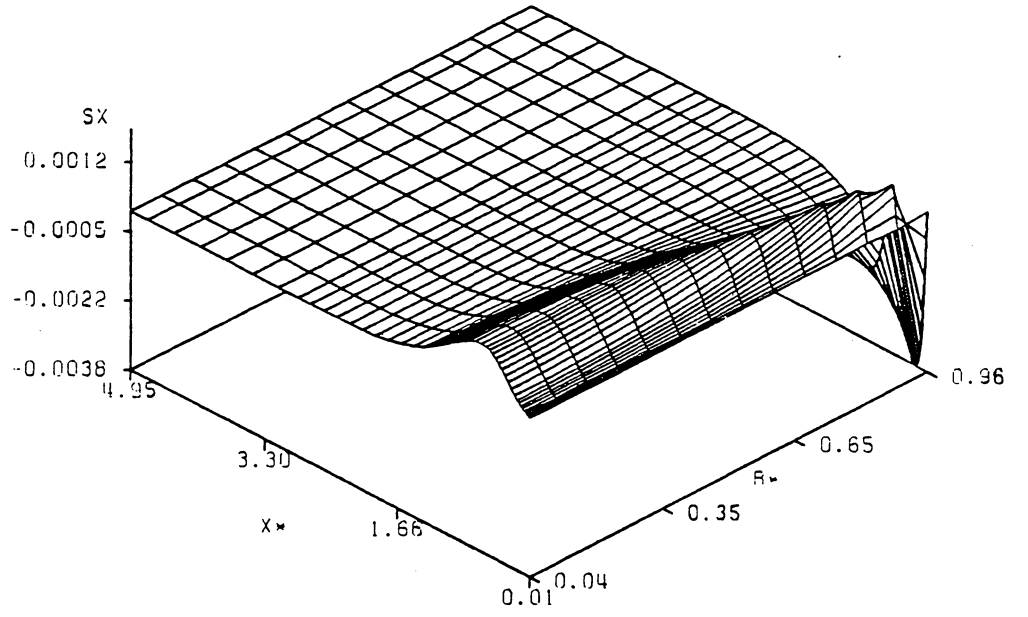

(a)

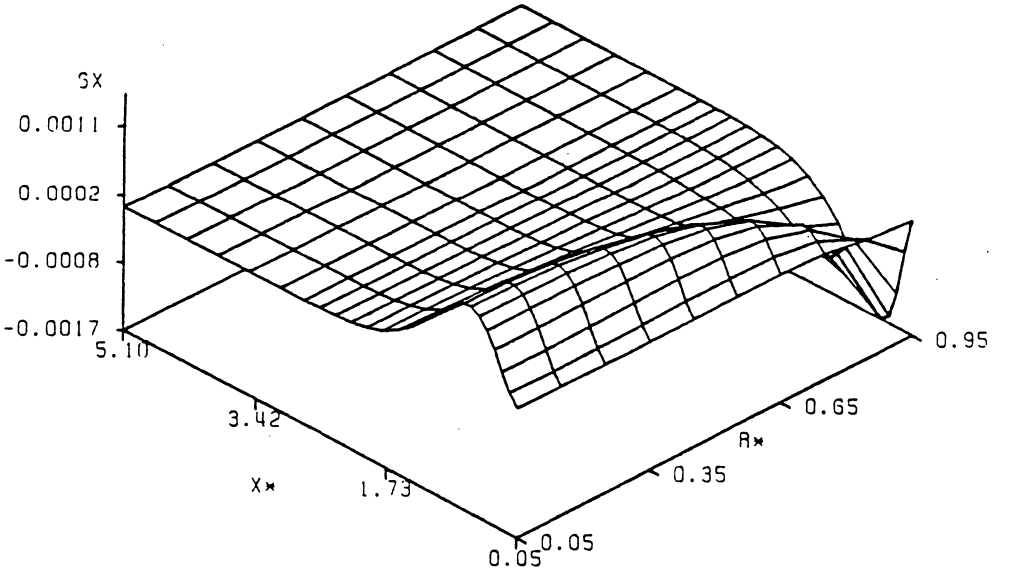

(b)

Figure 4.6 Non-dimensional longitudinal stress: (a) at t* = 0.001, (b) at t* = 0.03, and (c) at t* = 0.25 (next page).

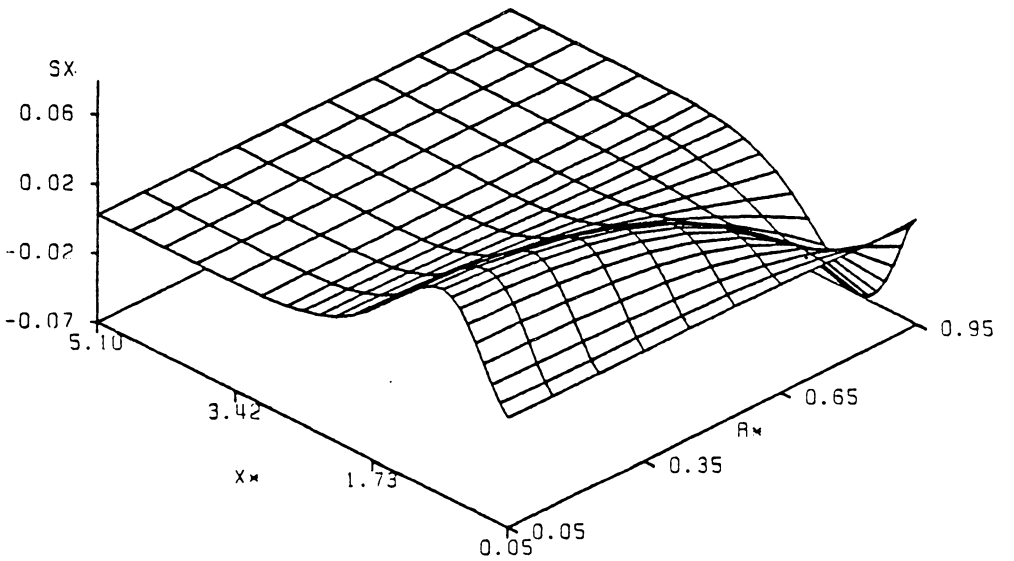

(c)

Figure 4.6 (Continued)

tially invariant within the time interval considered and is far beyond the thermal layer even at the start of the heating. This fact is more clearly depicted in Fig. 4.7 where the longitudinal stress distribution along the central axis is plotted for different values of t^*. This intriguing behavior of thermal stresses is discussed by Emery [19] and can be observed in the work of Jaunzemis and Sternberg [27], and Chang, et al. [12].

To study the combined effects of several stress components, the modified Coulomb-Mohr theory of failure is used to obtain the failure factor, which describes the risk of rupture of the material under stress. The failure factor is defined as the safety factor used in the modified Coulomb-Mohr theory of failure. Failure is assumed to occur as the failure factor reaches unity from below. The failure factor in three dimensions are plotted in Fig. 4.8 for the same values of t^* as before. At $t^* = 0.001$, Fig. 4.8.a shows that the region of highest risk of failure is near the edge. Closer to the central axis, the distribution displays three peaks. The first peak is on the surface. The second is the largest and is at some distance inside the body. At a greater depth inside the body is the third peak. At $t^* = 0.03$, the first peak becomes negligible relative to the other two and is not observable in Fig. 4.8.b. The second peak is still the largest but is being caught up by the third peak which increases most rapidly. It is also observed that the region near the edge now has less risk of failure than the region close to the central axis. This trend is again observed at $t^* = 0.25$. The third and the second peaks now merge into one, forming a region of highest risk of failure on the central axis.

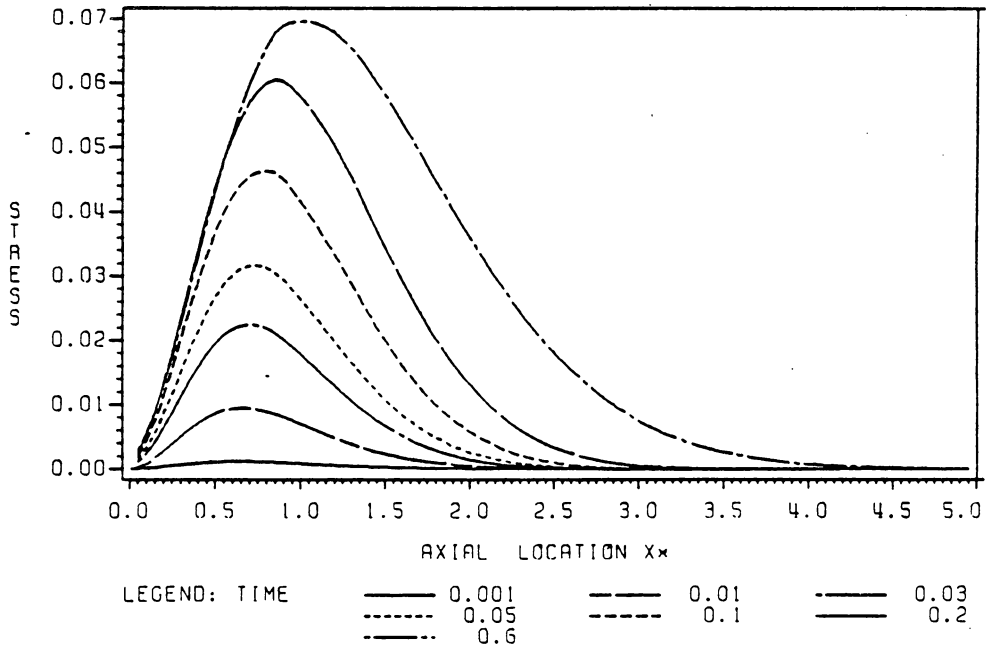

Figure 4.7 Non-dimensional longitudinal stress along the central axis at different times.

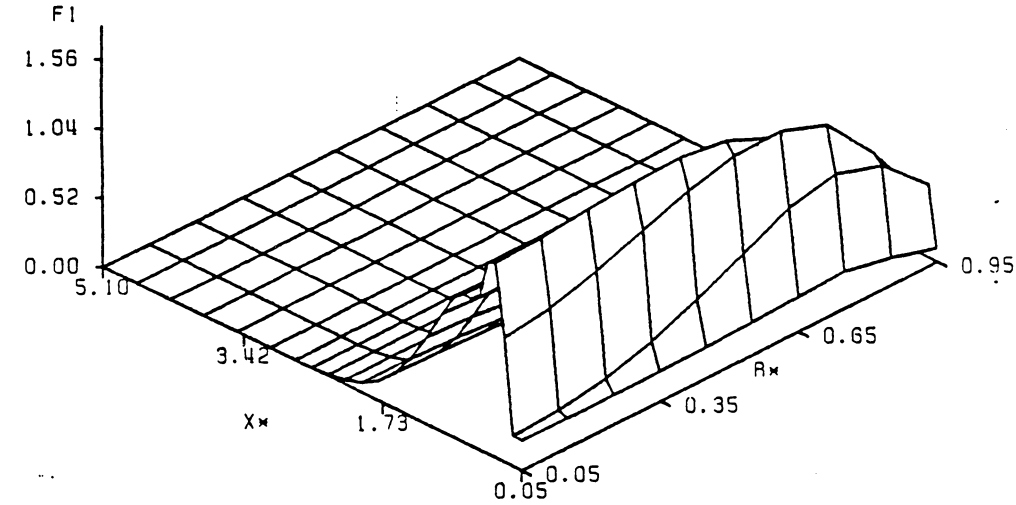

(a)

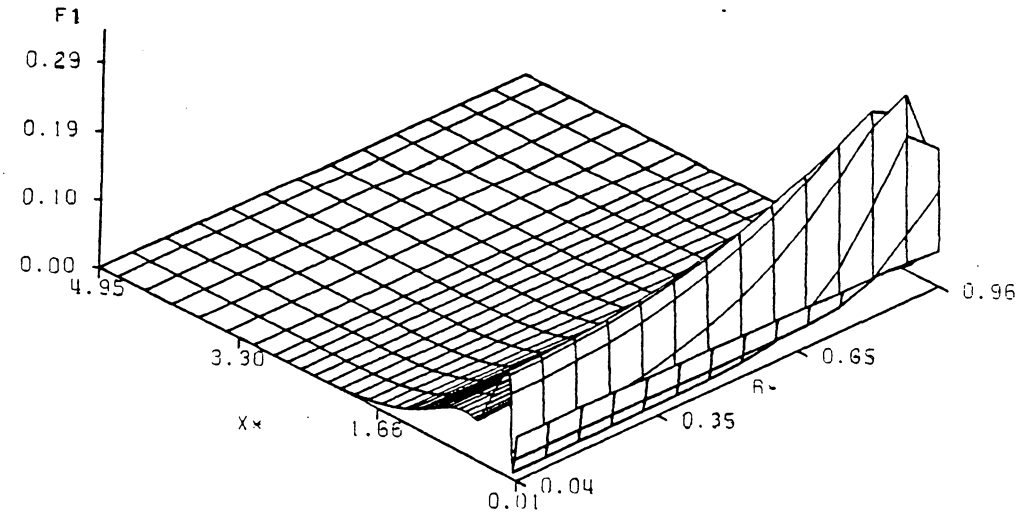

(b)

Figure 4.8 Failure factor distributions: (a) at t* = 0.001, (b) at t* = 0.03 and (c) at t* = 0.25 (next page).

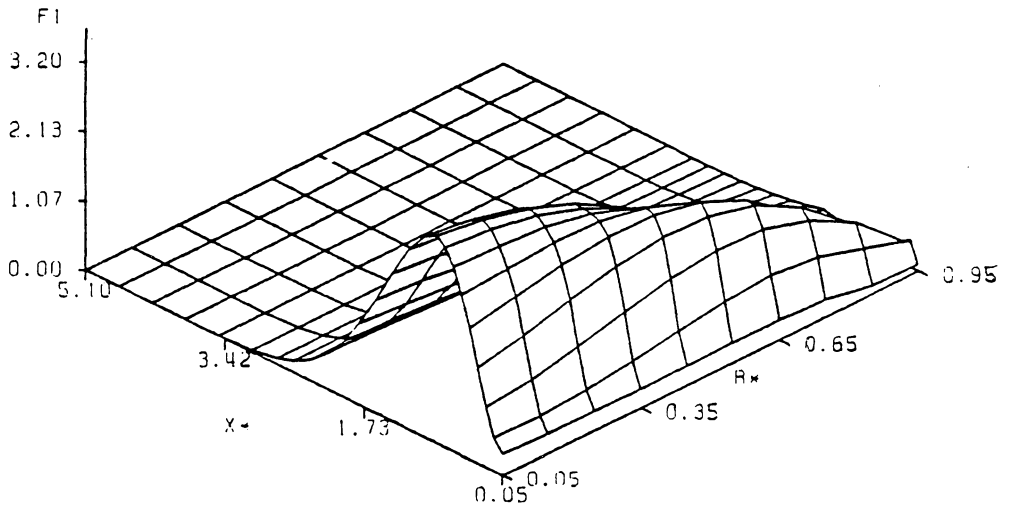

(c)

Figure 4.8 (Continued)

The relative magnitudes of the three peaks as functions of time are better depicted in Fig. 4.9 where the failure factor along the central axis is plotted for different values of t*. It can be estimated that the third and second peaks merge together at about t* = 0.1. The location of the third peak reminds us of the longitudinal stress. The second peak is observed to be close to the surface at short times after heating. It moves gradually deeper into the body and finally merges with the third peak. On the other hand, the first peak is always located on the surface and the location of the third peak is almost invariant.

A comparison of Figs. 4.8 and 4.9 with Figs. 4.3-4.6 suggests that the first peak on the surface of Fig. 4.8 reflects the effects of the compressive radial stress. Similarly, the second peak indicates the dominance of the tensile radial and tangential stresses in the region, and the third peak the dominance of the tensile longitudinal stress.

The contribution of each stress component to the risk of failure can be more easily observed in Figs. 4.10-4.12, where the cross sectional distribution of each stress component is plotted along with the failure factor for t* = 0.001, 0.03 and 0.25, at the location of the maximum failure factor along the central axis.

In figures 4.10.a and 4.10.b we can compare the distribution of the failure factor with those of the stress components at t* = 0.001. At this value of t*, the peak failure factor is located at x* =0.13 on the central axis. It is clear that at short time after heating, the tensile radial stress and tangential stress are the dominant contributors to the risk of failure. The high risk of failure near the edge is obviously due to the combined effects of all stress components.

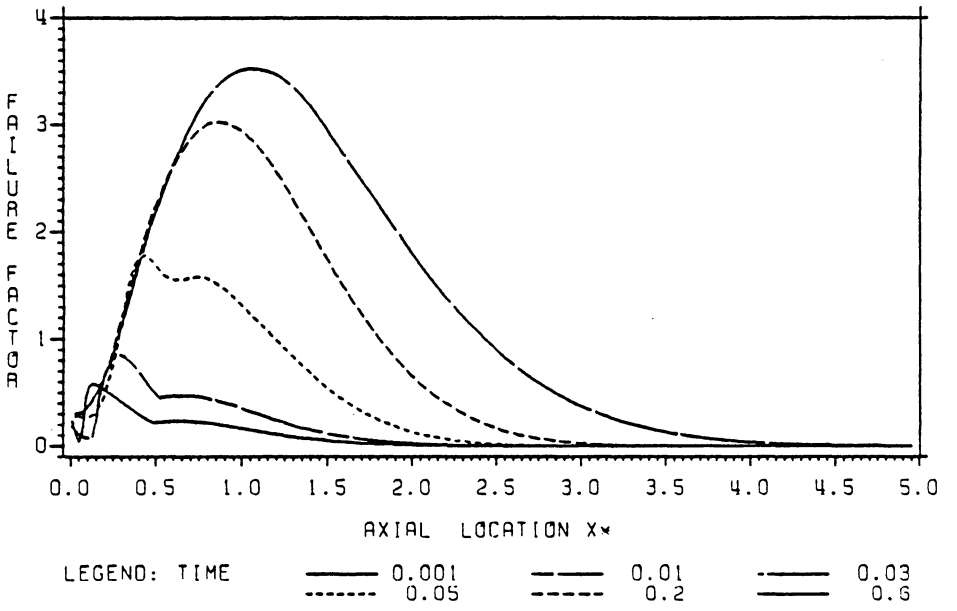

Figure 4.9 Failure factor along the central axis at different times.

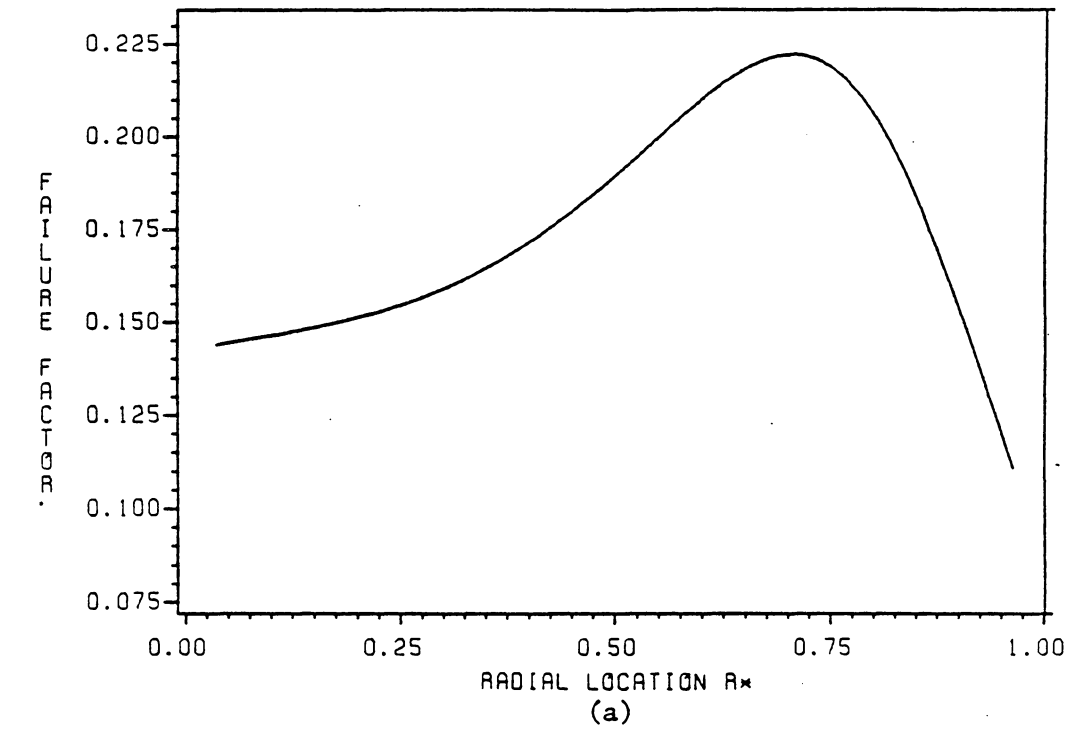

(a)

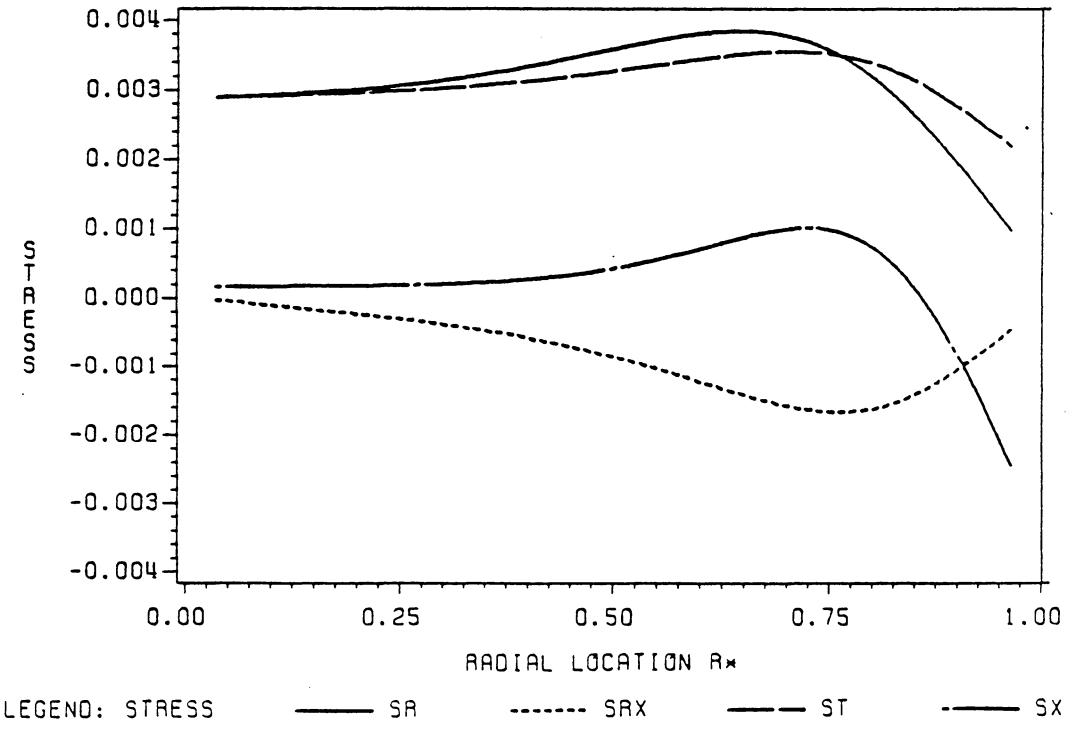

(b)

Figure 4.10 Failure factor and stresses at $t^* = 0.001$ and $x^* = 0.13$: (a) failure factor and (b) radial, tangential, shear and longitudinal stresses.

As the heating continues, the contribution of the other stress components becomes more significant. In Fig. 4.11, the failure factor and stress components are plotted along a cross-sectional plane for $t^* = 0.03$. At this time, the peak failure factor is at $x^* = 0.35$. By comparing Fig. 4.11.a and Fig. 4.11.b, we observe that the failure factor is not determined by any single stress component, and the relative contribution of each stress component again varies with the radial location.

At a still later time, as shown in Fig. 4.12, the longitudinal stress becomes more dominant in the region of high risk of failure. At $t^* = 0.25$, the peak failure factor is at $x^* = 0.9$. The region of high risk of failure is also observed to be more and more localized to the central region. This trend continues with the heating. At very large time after heating, the other stress components eventually become negligible relative to the longitudinal stress.

However, at times larger than 0.3, the peak stress changes very slowly, causing the maximum failure factor to be almost invariant with time as shown in Fig. 4.13. It is also observed that the region of high risk of failure becomes more localized, and failure is less likely to occur. Also, from the results not shown here, it is observed that at large time the maximum longitudinal stress moves perceptibly deeper into the body with time.

As mentioned before, some work has been done to study the stress distribution in the second thermal phase, i.e., after the first spalling. From preliminary results, a spall size of 0.9 and a spalling time of 0.25 were chosen for a case study. The justification for this choice is that at smaller times, the residual temperature distribution is neglible and

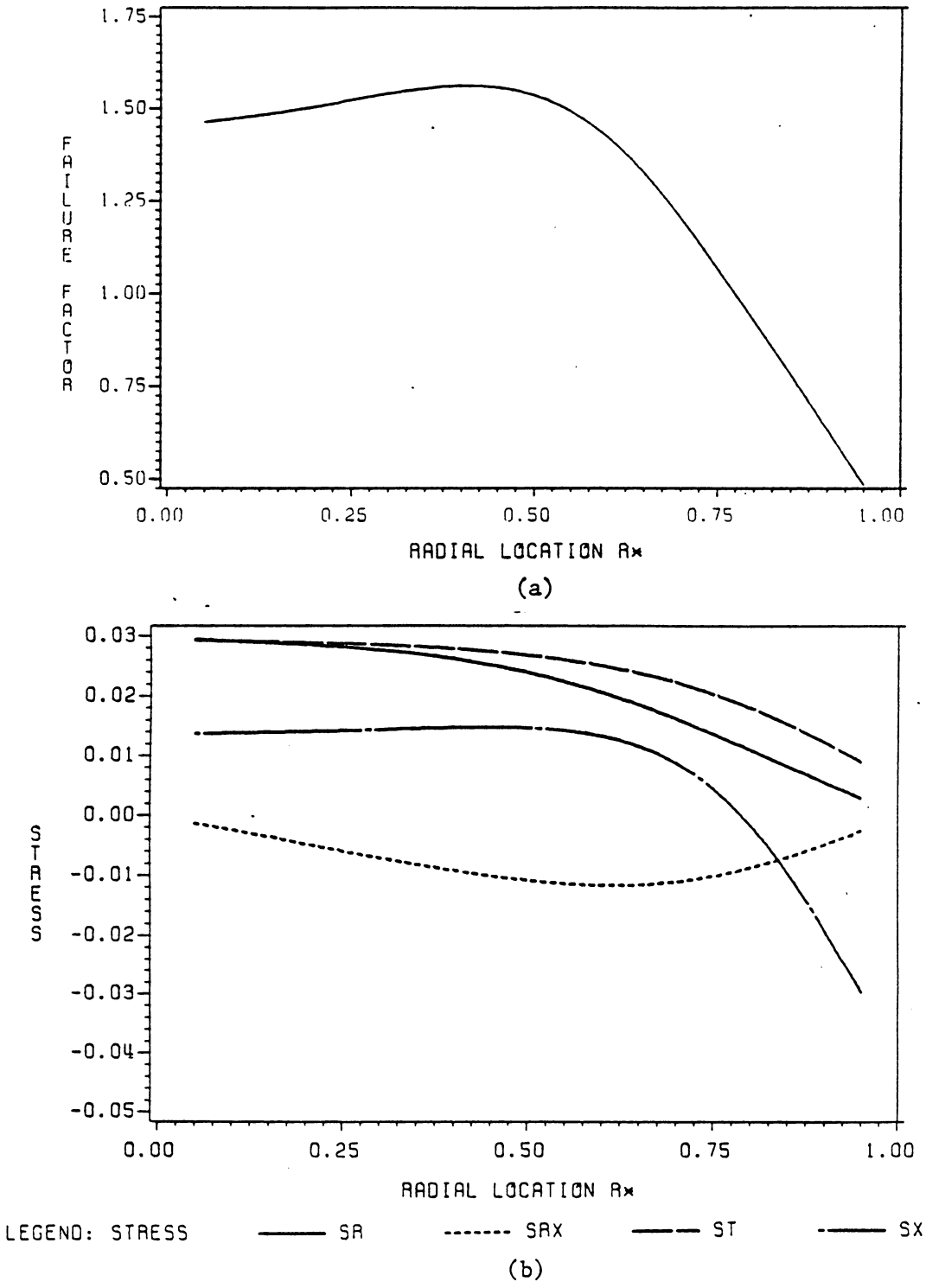

Figure 4.11 Failure factor and stresses at t* = 0.03 and x* = 0.35: (a) failure factor and (b) radial, tangential, shear and longitudinal stresses.

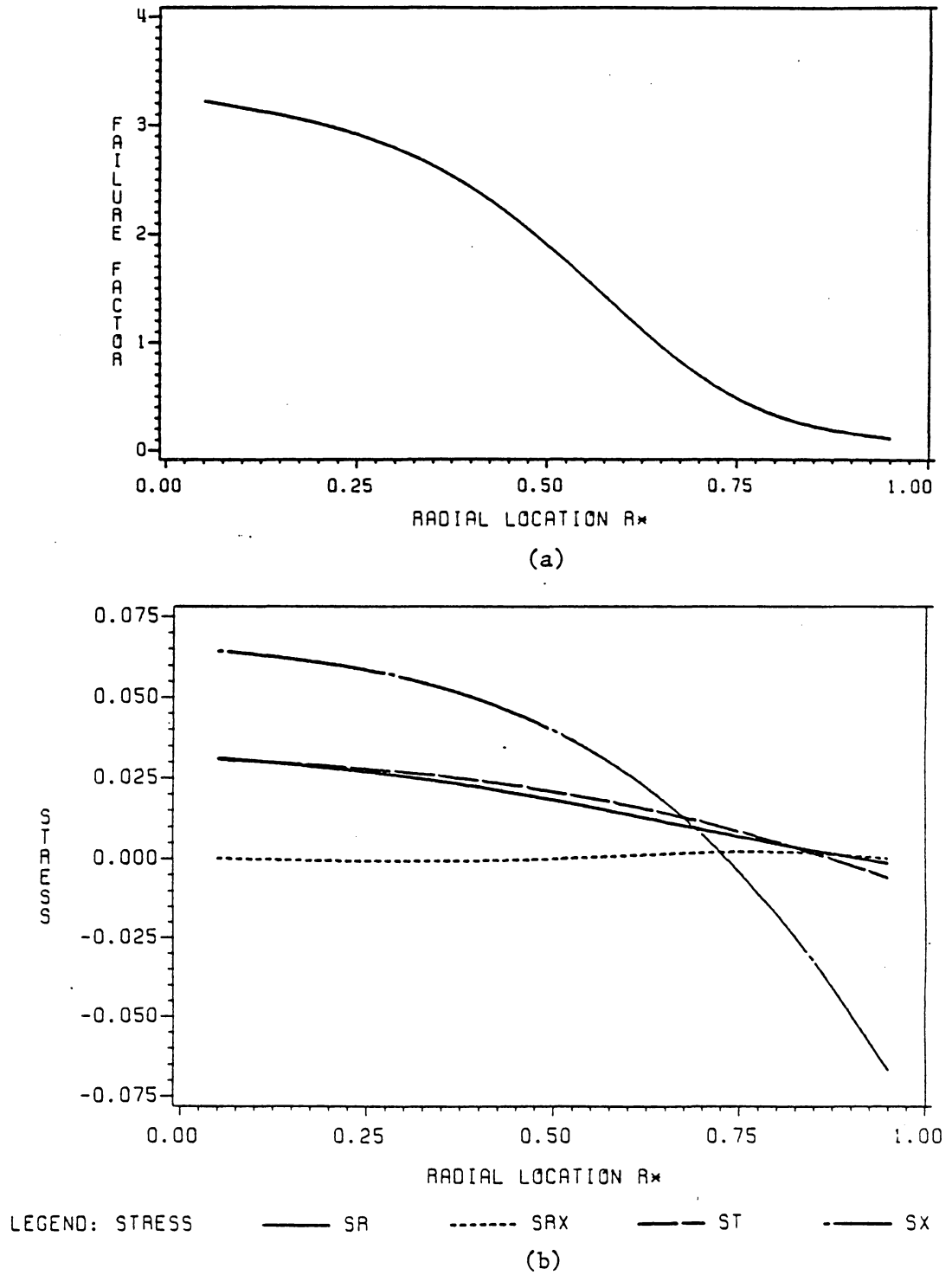

Figure 4.12 Failure factor and stresses at $t^* = 0.25$ and $x^* = 0.13$: (a) failure factor and (b) radial, tangential, shear and longitudinal stresses.

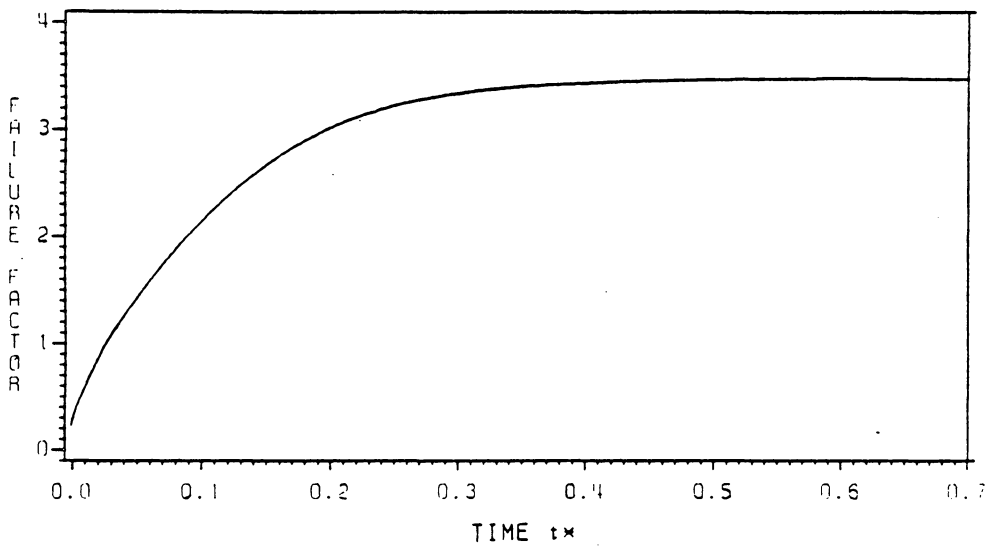

Figure 4.13 Time history of the peak failure factor along the central axis.

the thermo-elastic problems in all subsequent thermal phases are exactly the same as that of the first thermal phase.

In Figure 4.14 are plotted the stress distributions at time $t^* = 0.251$ or at a time of 1.05×10^{-3} into the second thermal phase. The stress distribution of each stress component shows the effect of the residual temperature from the previous thermal phase. As time passes, the residual stresses decrease, whereas the stresses caused by the heat flux at the new boundary keep increasing. The residual effects of the previous thermal phase soon become negligible. The presence of considerable residual temperature from the preceding phase allows subsequent thermal phases to reach the same critical value of failure in less time. Even in the case of non-negligible initial temperature distribution, the spalling process was found to reach steady state in a few thermal phases. At steady state the initial temperature distribution is almost invariant from one thermal phase to another. In the few cases considered here, the time for the failure factor to reach its highest value is reduced by as much as 10 percent at steady state as compared to the first thermal phase.

The residual effects of the previous thermal phase are more clearly observable in Figure 4.15 where the failure factor is plotted at the same value of t^*. The second peak is now less dominant than the third peak. In this case, the third peak is dominant both at small and at large times after heatings.

The numerical results in this section contain much useful information and implications which will be discussed in detail in the next section.

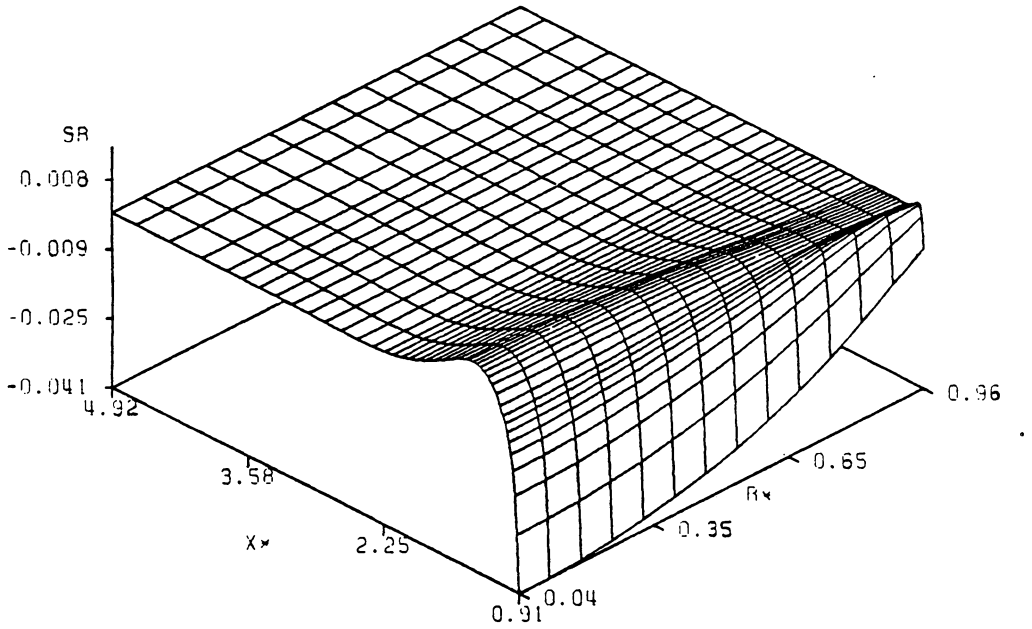

(a)

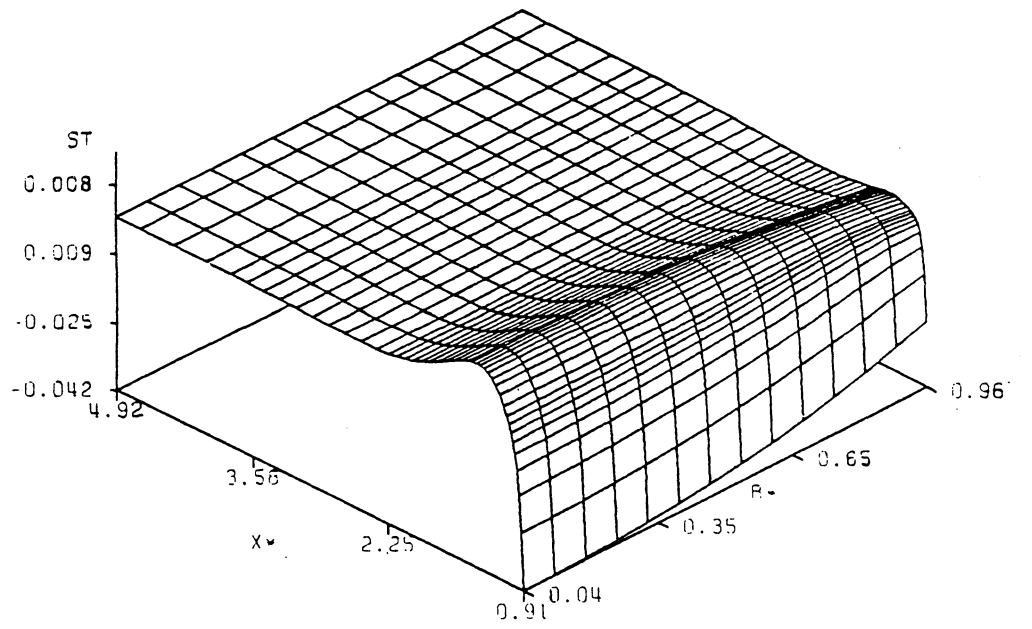

(b)

Figure 4.14 Stresses at t* = 0.001 into the second thermal phase: (a) radial stress, (b) tangential stress, (c) shear stress (next page), and (d) longitudinal stress (next page).

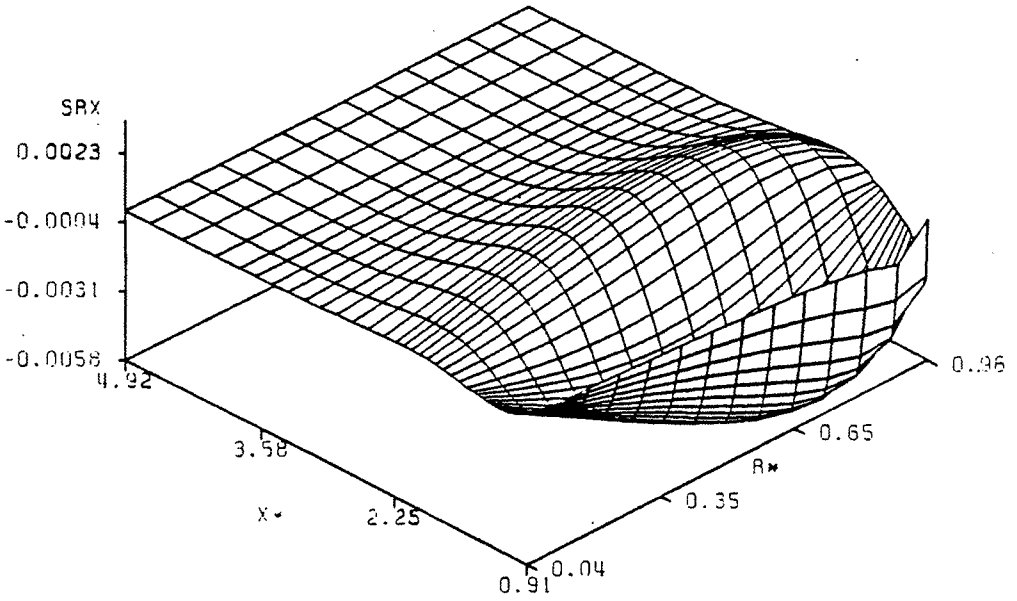

(c)

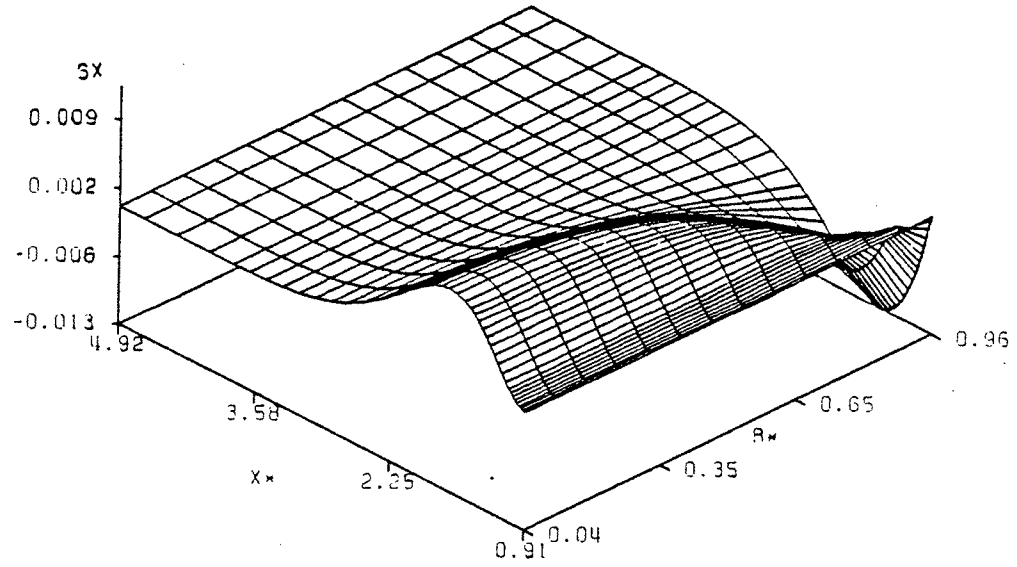

(d)

Figure 4.14 (Continued)

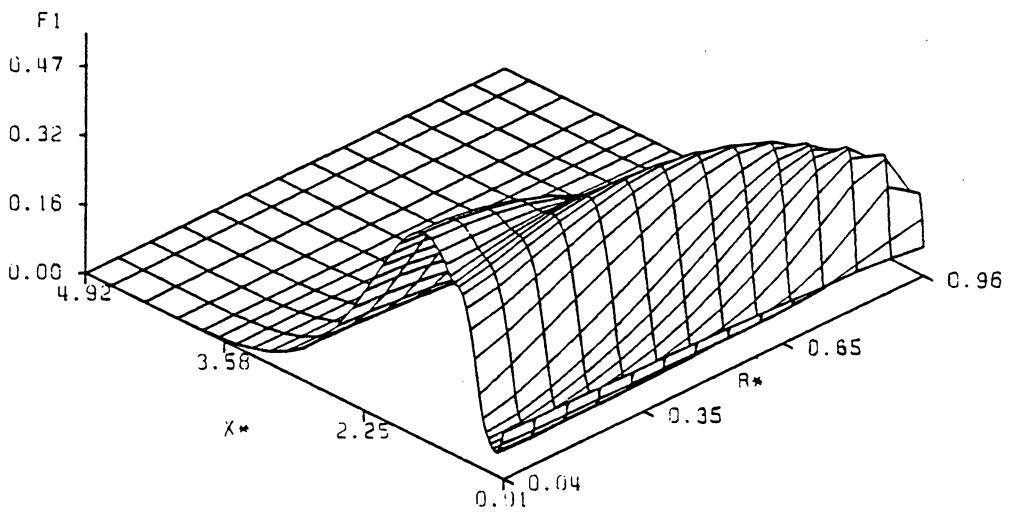

Figure 4.15 Failure factor at t* = 0.001 into the second thermal phase

3. DISCUSSION

The main objective of this chapter is to consider the combined effects of several stress components and to examine the validity of using a single stress component in studying thermal spalling in brittle materials.

From the numerical results in the previous section, it is obvious that considering any single stress component is conditional upon each specific problem and the time range of interest. As can be seen from the definition of non-dimensional time, $t^* = \kappa t/R^2$, the dominance of a stress component depends on thermal diffusivity and the characteristic dimension of the object as well as on the actual heating time.

For the geometry considered here, to use radial stress alone in the study of thermal spalling is only justifiable for small Fourier numbers. This corresponds to considering the time range where the second peak is rather close to the surface. This condition is often satisfied in problems of thermal shock, where the heat flux is intense and spalling occurs shortly after heating. In this case, failure by tensile radial stress is likely to result in cracks propagating parallel to the direction of heat flow, which is often observed in the literature [31-33,48].

A point to note is that the models based on a fully constrained or infinite object used in the literature take into account only the compressive lateral stress on the surface, corresponding to the first peak of the failure factor distribution in Fig. 4.6. This is not a correct approach for our specific problem because the risk of rupture on the surface is always negligible.

On the other hand, under slow heating where spalling only occurs at a very late time, it is more or less justifiable to consider longitudinal stress only, although the risk of failure so predicted is lower than in reality. In this case, another factor should be taken into account in predicting failure. Failure is not determined solely by the local maximum stress but by the stress distribution in the entire body. This is the basis of the Weibull statistical theory of failure and is discussed in detail by Manson [31,32].

At large times, as can be observed in Fig. 4.4.d, the region of high risk of failure is very localized to the region around the central axis. In this case, considering the peak failure factor alone is insufficient. A statistical approach similar to Weibull's is thus required.

For intermediate values of t*, no stress component is absolutely dominant. Failure results from the contribution of all stress components. The relative contribution of each stress component varies with time and location. In this case, it is necessary to take into account the combined effects of all stress components with the use of an appropriate theory of material failure. Otherwise, erroneous predictions of spalling may result.

One interesting example is to consider longitudinal stress only. A characteristic of the longitudinal stress is to have its maximum located far inside the body even immediately after heating starts. Under intense heat flux, this maximum stress may well exceed the material tensile strength. A criterion for failure based on longitudinal stress alone would predict a spall of thickness of about R. This is obviously unreasonable. On the other hand, using the failure factor as the criterion

for failure, the thickness of the spall is much smaller, which agrees better with what happens in reality.

In our attempt to study the process of repetitive spallings, we observe that in most cases, the residual temperature from the preceding thermal phase is negligible. Only when spalling occurs at large t^* do we observe non-negligible residual temperature distribution. These effects of the residual temperature distribution are, however, soon dominated by the effects of the new boundary condition. In all the cases considered, the residual temperature becomes invariant from phase to phase after the second thermal phase, implying that the spalling process has reached a steady state very soon. From our preliminary study, it is also observed that the failure factor in the subsequent thermal phases reaches the same critical value in considerably less time than in the first thermal phase. It is therefore expected that in general the steady state spalling rate is higher than the initial spalling rate, if no other factors are involved. In reality, it is reported [22] that the steady state spalling rate is lower than the initial rate due to a certain degree of fusion involved. However, fusion is not our concern here, and will be discussed in the following chapter.

In summary, this study shows that each stress component has its own contribution to the risk of failure and none is at all times dominant. It is therefore necessary to use a comprehensive criterion of failure, e.g., the modified Coulomb-Mohr theory of failure used here, which takes into account the effects of several stress components in the study of thermal stresses and thermal spalling. In the case where such an approach is not computationally feasible, care should be taken to determine the

validity of considering any single stress component as being dominant from preliminary studies. For instance, in the problem considered here, there is a range of t^* where considering radial stress only is more or less justifiable. Similarly, at very large t^*, the inaccuracy of considering longitudinal stress alone would not be excessive. However, at intermediate values of t^*, there is no other choice than to consider the combined effects of all the stress components.

V. SURFACE SPALLING PRODUCED BY CONFINED HEATING

A simple model is intentionally used in chapter IV to study the interrelations between different stress components. However, since the model is simplistic, the results obtained are highly theoretical and can hardly find any application in reality. In this chapter a more realistic model is used to simulate the many operations involving thermal spalling. The model consists of a large axi-symmetric object. The heat flux is assumed to be confined to a circular area on the surface. This assumption more or less simulates the heating condition induced by jet flames used in jet-piercing operations on a large body of rock, and allows the assumption of axi-symmetry to be used.

In the case of axi-symmetrically confined heating, the temperature distribution becomes two-dimensional. Although the technique of fictitious boundary conditions can be extended to two-dimensional problems, the inaccuracy involved in the approximation of the initial condition makes the technique less attractive. As an alternative, an exact solution could be obtained for temperature. However, for convenience, a finite element model has been used to obtain both temperature and stress distributions. The purpose, in addition to studying the combined effects of different stress components as before, is to determine the effects of material properties, in conjunction with external factors, on the spallability or tendency to spall, and spalling rate of brittle materials. It will be seen that these two parameters are related through the char-

acteristic dimension, which is the radius of the heat flux area in this case.

A risk-of-rupture criterion, the failure factor, is used as a design parameter. Plots of the failure factor along the central axis, the location of the peaks along the central axis, the maximum surface temperature, and the depth of the thermal layer are presented with a suggestive example to illustrate their use in design.

1. FINITE ELEMENT MODEL

The problem is illustrated in Fig. 5.1. A large body of radius R and of thickness L as shown in Fig. 5.1.a and b, is subjected to a heat flux of intensity q'' confined to a circular area of radius R_q. The edge at $r = R$ is assumed to be insulated. The back face at $x = L$ is maintained at T_0, the ambient temperature and also the bulk temperature of the body. This boundary condition on the back face is always satisfied if L is large enough compared to the thermal layer, defined as the distance over which the temperature rise is negligible. For stress, the model is assumed to be fully constrained at the edge and the back face.

The finite element model is axi-symmetric, with R_q fixed while R and L are adjusted in order to approximate an infinite body of rock. In other words, R and L are chosen such that the thermal layer is smaller than the geometrical dimensions and the edge effects on stresses are negligible. The values of R and L thus depend on the intensity of the heat flux and the length of time the body is heated. The aspect ratio of the elements in the mesh is consistently maintained at below 3 in the region of in-

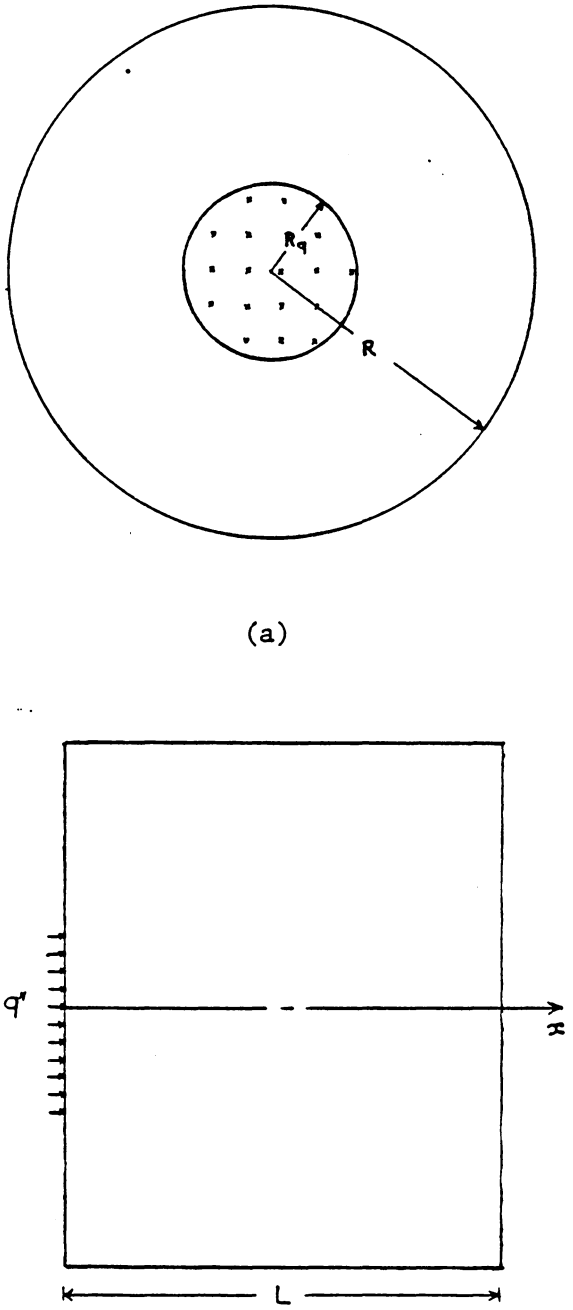

Figure 5.1 The finite element model: (a) a large body of radius R and thickness L subject to a constant heat flux q", (b) stress components on a differential element.

terest (heated area and neighborhood) and below 7 in the outer regions. The dimensions R and L are therefore chosen as compromises to satisfy constraints on both the aspect ratio and the negligibility of edge effects.

In this context, the x-axis will be referred to as the central axis and locations on this axis referred to as axial locations. Because many quantities exhibit maxima both in time and space, "maximum" will be used to refer to spatial maximum unless stated otherwise in cases of possible confusion.

The stress components pertinent to this model are the same as in Chapter IV and are depicted in Fig. 4.2. The normal stress in the x-direction is called the longitudinal stress, σ_x, and the one in the r-direction the radial stress, σ_r. The tangential stress, σ_t, is normal to the r-x plane and is a principal stress. The shear stress on the plane normal to the r-axis and parallel to the x-axis is denoted by σ_{rx}.

Non-dimensional parameters are used. Many of them are defined similar to those used in chapter IV. The non-dimensional time, t*, defined as $\kappa t/R_q^2$, is actually the Fourier number. In this context, time and Fourier number are used interchangeably if not otherwise stated. The thermal stress resistance, R_{th}, is defined as $(k/q''R_q)(S_t(1-\nu)/E\alpha)$. The strength ratio R_{st} is again the ratio between the tensile and compressive strengths, S_t/S_c. The failure factor F assumes the same form as before, and it is the inverse of the safety factor used in the modified Coulomb-Mohr theory of failure [52,58]. All geometrical dimensions are non-dimensionalized based on the radius of the heat flux area, R_q. Non-dimensional stresses are defined as $(k/q''R_q)\sigma_i(1-\nu)/E\alpha$, where the

subscript i of σ is replaced by r, x, t, and rx for radial, longitudinal, tangential, and shear stress components, respectively. Temperatures are non-dimensionalized as $kT(x,t)/R_q q''$. An asterisk as superscript refers to non-dimensional quantities.

Since the failure factor is more sensitive to the mesh size and boundary effects than stresses, care has been taken to consider the convergence of the failure factor. Convergence is assumed at the level of 3 percent or less difference between successive refinements.

Numerical results are obtained for a specific case of $R_{st} = 0.05$ and $R_{th} = 0.02$, and are presented in the following section in the form of non-dimensional quantities as defined above. These values of R_{st} and R_{th} are chosen to give good clarity of plots and to be within the range of actual values found for rocks.

2. NUMERICAL RESULTS

Three-dimensional plots of each stress component and of the failure factor at three typical values of the Fourier number are presented first to give a better insight to the stress distribution in the body and to possibly allow some conjectures on the contribution of each stress component to the overall picture of failure. The maximum failure factor and its location along the central axis is also plotted as a function of time for use in design. The surface temperature and the depth of the thermal layer are given as additional information to predict the quality of spalling, i.e., the degree of fusion involved, and the initial condition of the next thermal phase.

Figures 5.2-5.5 show radial, tangential, shear, and longitudinal stresses, respectively, for 3 values of the Fourier number; namely 0.001, 0.03, and 0.25. These values represent short, intermediate and long times after the heating starts. This classification of the Fourier number into different ranges is by no means rigorous and will be made clear later in connection with the results for the failure factor. This classification parallels the one in the preceding chapter. The plots are geometrically truncated to show the regions of interest with better clarity and to provide roughly comparable drawing scales for ease of comparison between figures. It should be noted that for all three-dimensional plots in this section, the x-axis is the axis of revolution of the axi-symmetric object, and the radius of the heat flux area is located at $r^* = 1.0$.

Figure 5.2.a displays the radial stress distribution at $t^* = 0.001$. The radial stress is compressive at the front face and becomes slightly tensile at some distance beneath the heated surface. It is observed that, as for other stress components, the radial stress distribution is essentially uniform over the heated region and localized to this region. The uniformity and localization of the stress distributions imply that right after the heating starts, the problem can be approximated with unconfined heating over an infinite surface, resulting in a state of plane stress, as assumed by some authors mentioned in the literature review [22,30]. Figure 5.2.b displays the radial stress distribution at a time of $t^* = 0.03$. The radial stress at the surface becomes more compressive and less uniform across the surface. The magnitude of both the compressive stress on the surface and the tensile stress beneath the surface are largest on the central axis and decrease towards the boundary of the heated area.

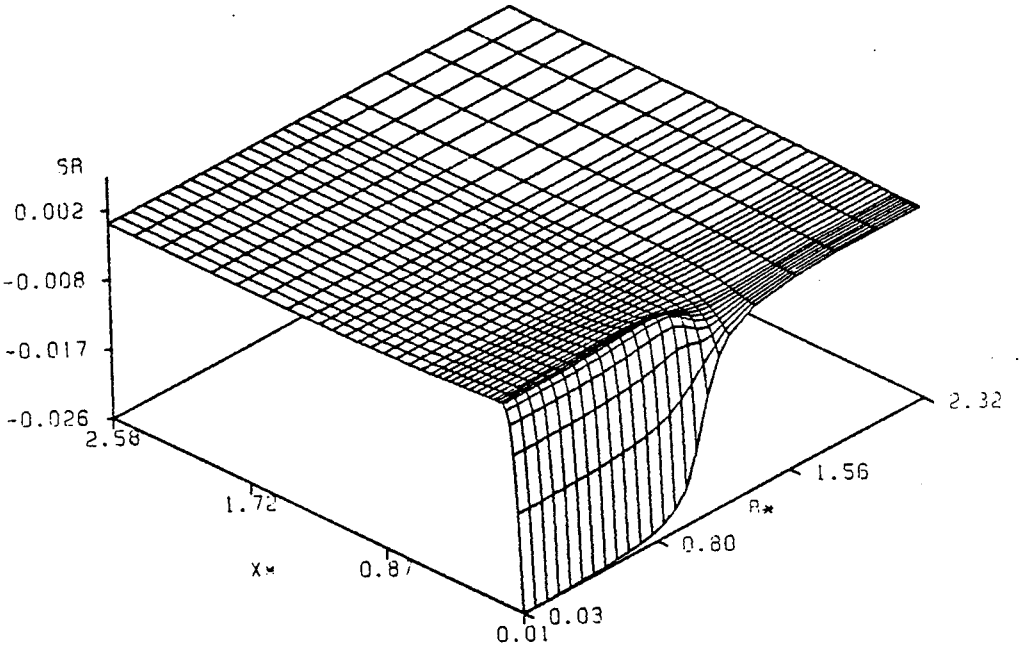

(a)

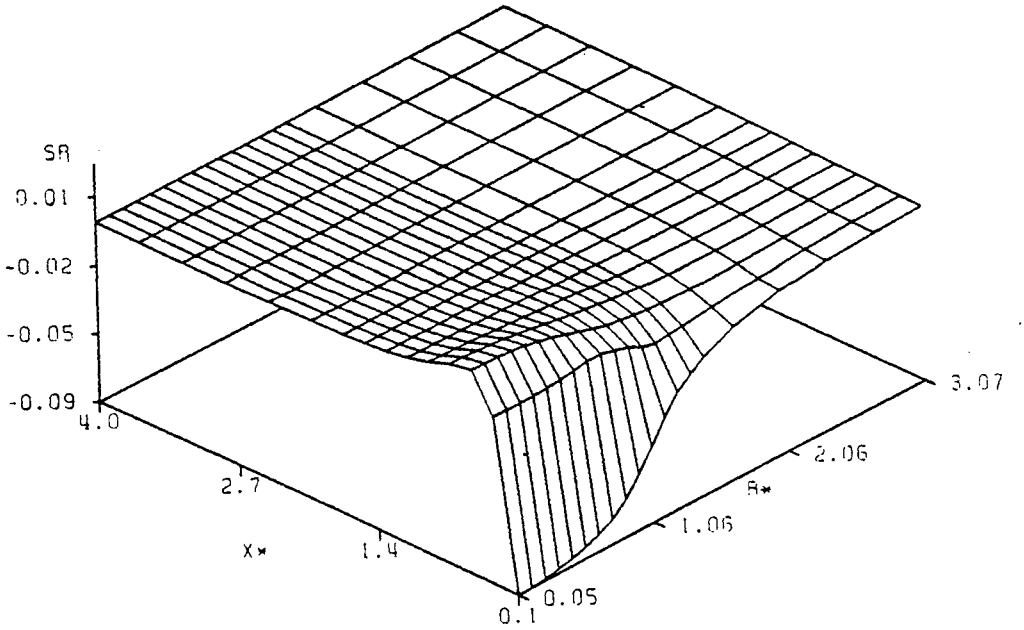

(b)

Figure 5.2 Non-dimensional radial stress: (a) at t* = 0.001, (b) at t* = 0.03, and (c) at t* = 0.25 (next page).

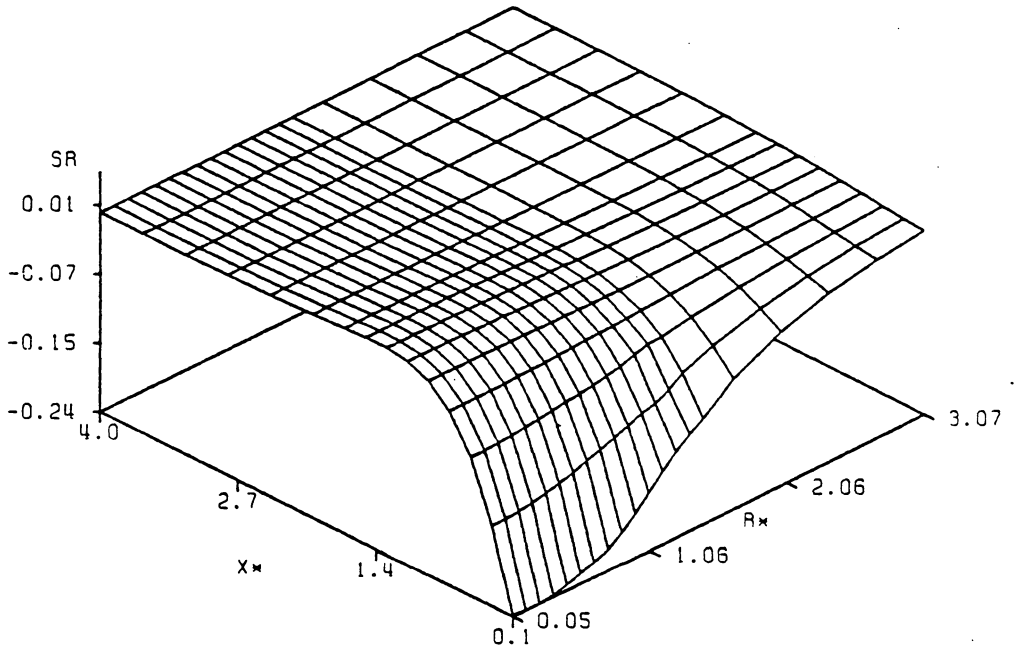

(c)

Figure 5.2 (Continued)

The spatial maximum of the tensile stress increases in magnitude with time at a rate higher than that of the compressive stress, and migrates deeper into the body. Figure 5.2.c shows that at a still larger time, $t^* = 0.25$, the same trend continues, i.e., the maximum tensile stress increases in magnitude as it moves deeper into the body. It is noted that at $t^* = 0.25$, the stressed region on the surface has spread to a radius of $2R_q$.

A point to note here and to be discussed later is that the maximum compressive stresses are always located on the surface. If failure were caused by the compressive stresses or their induced shear stresses alone, it would not yield a finite spall thickness as described in the literature [22].

Figure 5.3 displays the tangential stress for the same Fourier numbers as in Fig. 5.2. The tangential stress has distributions very similar to those of the radial stress. In fact, on the central axis the two stresses are identical from axi-symmetry. A noticeable difference is that at small times, as shown in Fig. 5.3.a, the tangential stress changes more abruptly in the region around $r^* = 1.0$.

Shear stress distributions are presented in Fig. 5.4. Of all stresses, shear stress is the most complex. At $t^* = 0.001$, Fig. 5.4.a shows that a large negative shear stress develops on the surface near the circumference of the heated region, probably because of the sudden change in the distributions of the other stress components. This shear stress becomes positive at some distance beneath the surface, forming a positive bulge. At $t^* = 0.03$, Fig. 5.4.b, the positive bulge migrates deeper into the body. At the same time, a negative bulge close to $r^* = 1.0$ grows to considerable size. The same trend is observed at $t^* = 0.25$, as shown in

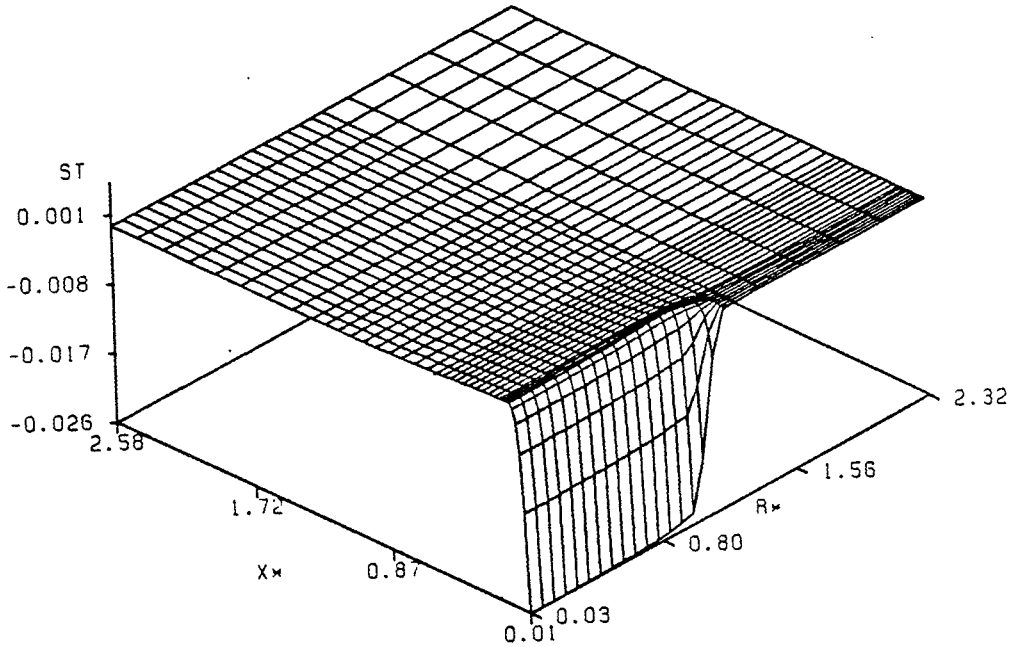

(a)

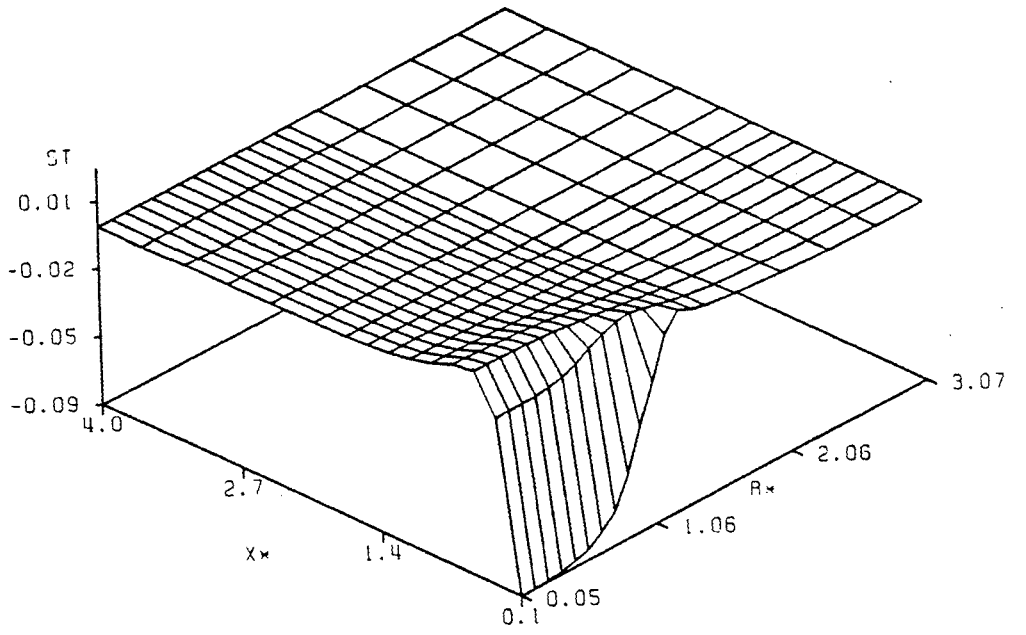

(b)

Figure 5.3 Non-dimensional tangential stress: (a) at t* = 0.001, (b) at t* = 0.03, and (c) at t* = 0.25 (next page).

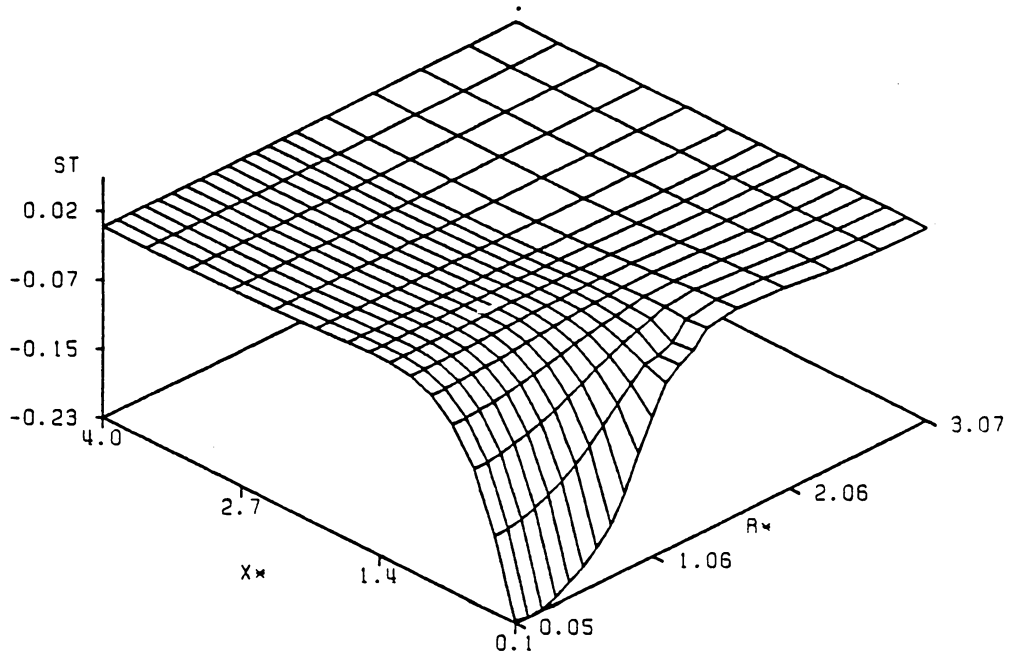

(c)

Figure 5.3 (Continued)

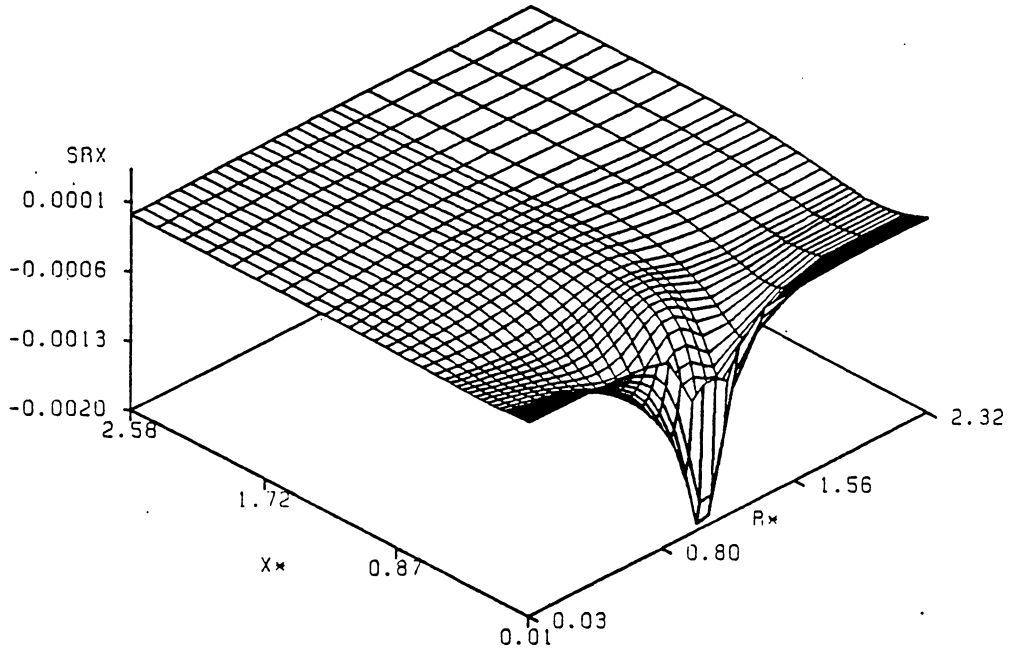

(a)

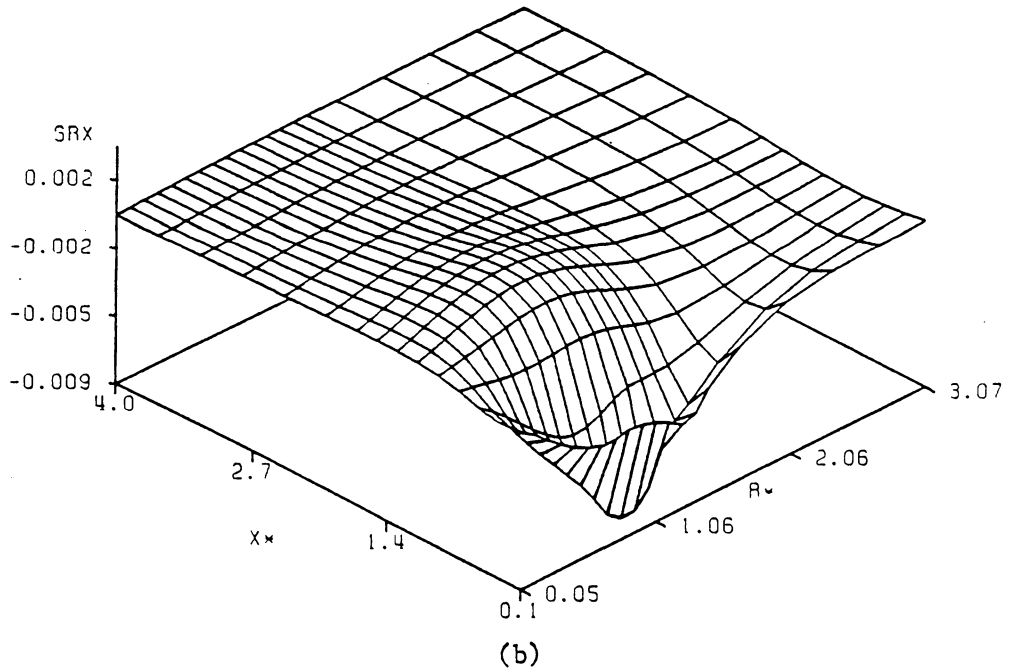

(b)

Figure 5.4 Non-dimensional shear stress: (a) at t* = 0.001, (b) at t* = 0.03, and (c) at t* = 0.25 (next page).

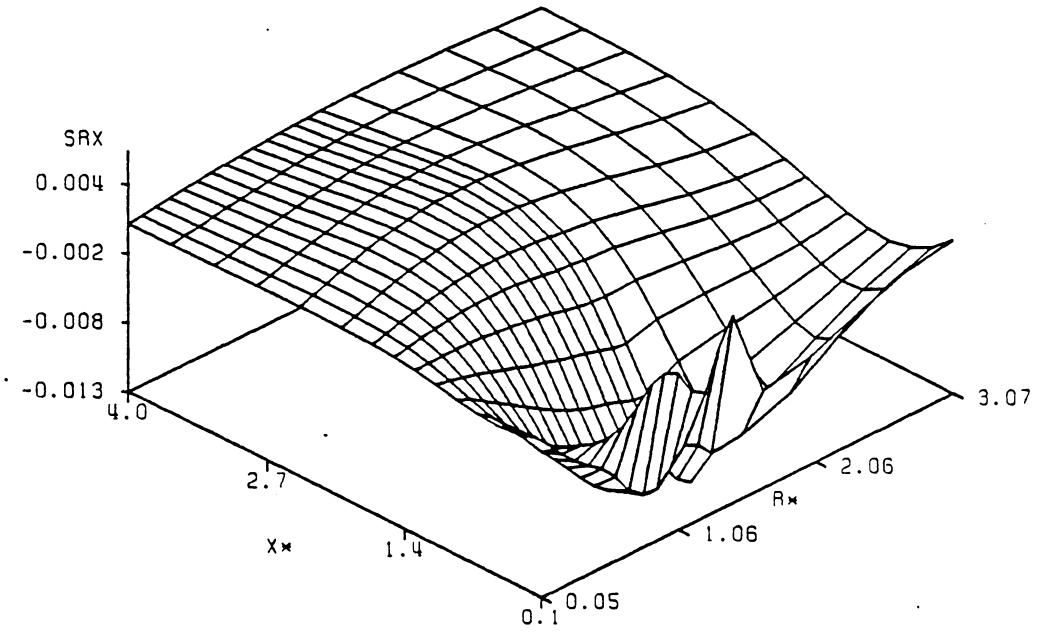

(c)

Figure 5.4 (Continued)

Fig. 5.4.a, with the effects of the heating felt well beyond the region under direct heat flux. From axi-symmetry it is known that shear stress on the central axis is zero.

In Fig. 5.5, longitudinal stress distributions are presented for the same three Fourier numbers. At $t^* = 0.001$, Fig. 5.5.a, the longitudinal stress along the central axis is positive and has a maximum at a location rather deep inside the body, namely, at a distance of about R_q beneath the front face, and is rather uniform across a plane parallel to the front face. Close to the boundary of the heated area, the stress state is rather complex and displays an abrupt sign reversal due to the temperature gradient in the radial direction. At $t^* = 0.03$, Fig. 5.5.b shows that the maximum longitudinal stress on the central axis increases in magnitude and becomes the global maximum. As shown in Fig. 5.5.c, at $t^* = 0.25$, this maximum, still a global maximum, has started to decrease in magnitude while a larger portion of the material comes under stress. Unlike the other normal stress components, which have a tensile maximum close to the surface at small times and moving deeper into the body with time, the longitudinal stress along the central axis has a maximum at a location of about R_q beneath the surface, even at the very beginning of the heating, and this location is almost invariant over a large interval of time. This same behavior has already been observed for the case studied in chapter IV.

Since assuming failure by tensile longitudinal stress is still a controversial issue, this behavior of the longitudinal stress deserves more thorough inspection, especially when the current model is used to study jet-piercing operations.

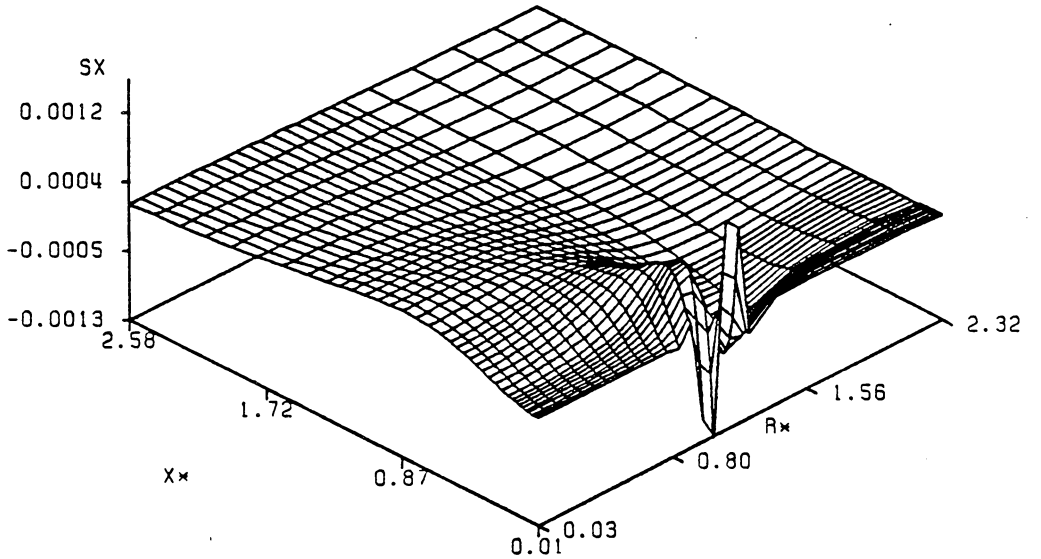

(a)

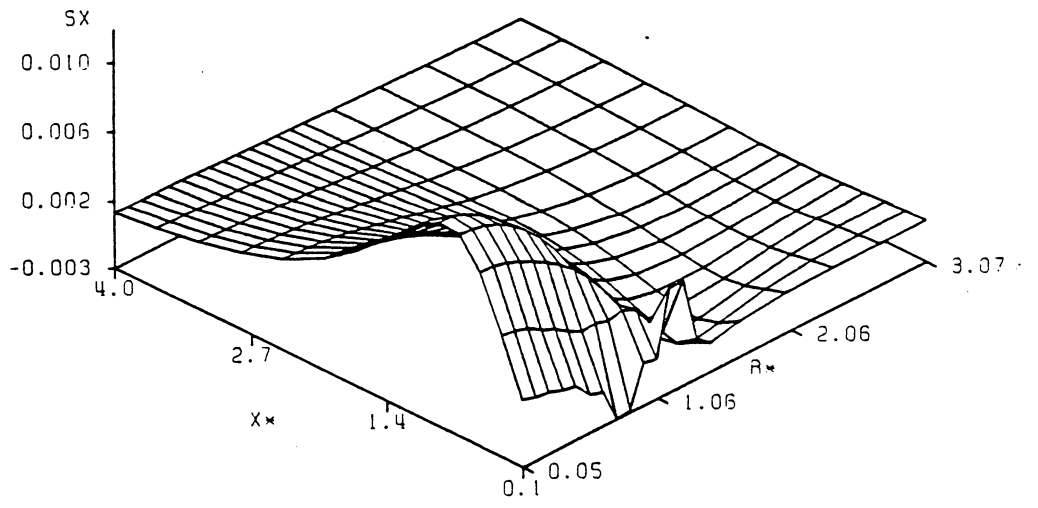

(b)

Figure 5.5 Non-dimensional longitudinal stress: (a) at t* = 0.001, (b) at t* = 0.03, and (c) at t* = 0.25 (next page).

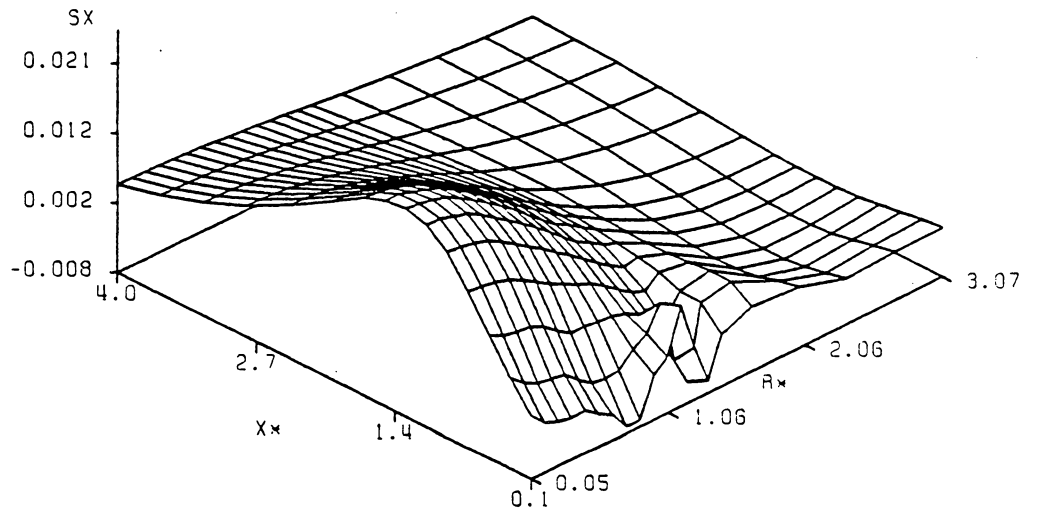

(c)

Figure 5.5 (Continued)

The behavior of the longitudinal stress is better viewed in Fig. 5.6 where the longitudinal stress along the central axis is plotted for various Fourier numbers. It is observed that the maximum longitudinal stress reaches a peak at about $t^* = 0.2$ and $x^* = 1.3$. At larger Fourier numbers the stress profile becomes flatter with a larger region being stressed. As noted before, the location of the maximum stress is situated at a depth of about one radius R_q even at the beginning of the heating, and is essentially invariant for a large range of Fourier numbers, namely, from the start up to 0.1. This observation agrees with the analytical results obtained by Jaunzemis and Sternberg [27] for a similar case of confined heating. This behavior of the longitudinal stress implies that if failure were due to tensile longitudinal stress alone, the thickness of the spall would be of about the size of the radius of the heated zone, which is not realistic and not observed in tests or in actual operations [22]. On the other hand, the existence of considerable longitudinal stress at large times suggests that the assumption of plane stress, i.e., neglecting longitudinal stresses, for the case of confined heating is good only at short times after heating starts. Another interesting point to observe is that the maximum longitudinal stress occurs far beyond the extent of the thermal layer. This is obvious from comparing Fig. 5.6 with Fig. 5.7, which shows the non-dimensional temperature profiles along the central axis at various times. The possibility of having maximum stresses in regions beyond the reach of the thermal layer has been observed in the literature [19,37] and will be discussed in more detail.

In summary, the assumption of failure by tensile longitudinal stress alone, commonly made in the literature, does not constitute a good model

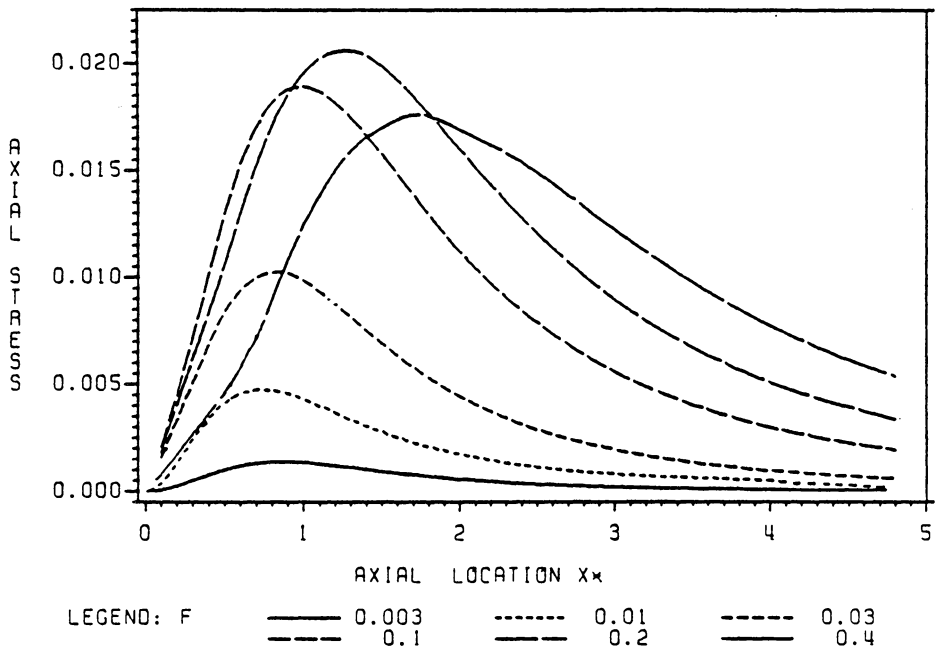

Figure 5.6 Non-dimensional longitudinal stress along the central axis at various times.

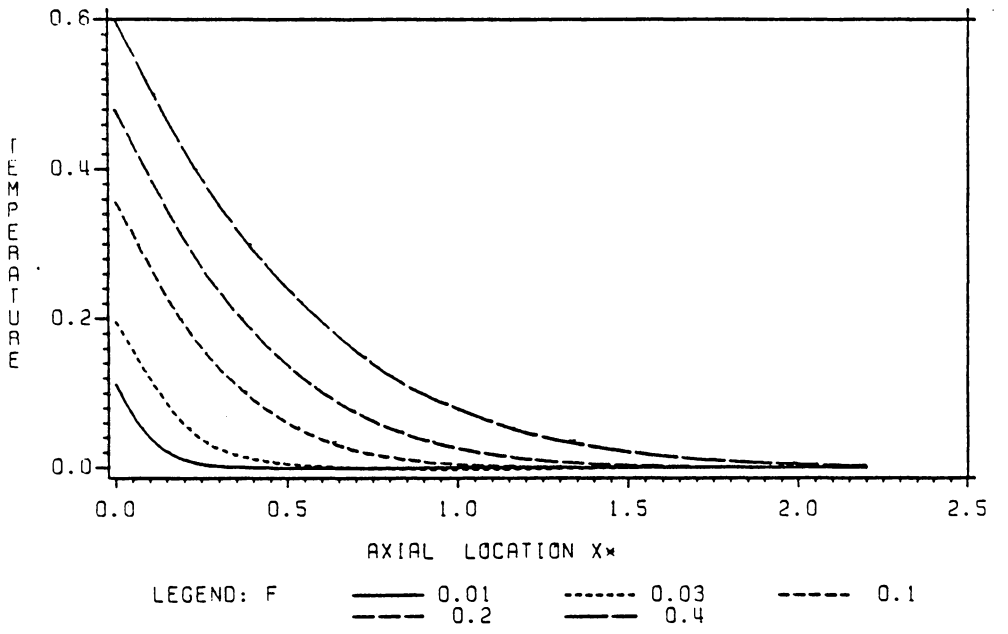

Figure 5.7 Temperature profile on the central axis at various times.

for the case of confined heating. On the other hand, neglecting the longitudinal stress altogether by assuming plane stress is valid only for short times after heating. In fact, failure is caused by the combined effects of many stress components, requiring a more comprehensive theory of failure.

Here the modified Coulomb-Mohr theory, which considers only principal stresses, is chosen because of its well known suitability for the study of fracture in brittle materials [58,61]. In this theory of failure the safety factor is defined as the largest ratio of principal stresses over the compressive and tensile strengths of the material. The reciprocal of the safety factor is used here as a measure of the risk of rupture and is called, in this context, the failure factor. A more detailed definition of the failure factor is presented in Appendix D. Failure is considered likely when the failure factor reaches unity from below. The use of this failure factor actually reduces a tensorial quantity to a positive scalar parameter, the failure factor, simplifying the task of predicting failure.

Figure 5.8 shows three-dimensional distributions of the failure factor for the same three values of the Fourier number used in Figs. 5.2-6.5. At $t^* = 0.001$, Fig. 5.8.a, the failure factor distribution displays a maximum at the boundary of the heated region on a plane parallel to and near the front face. At regions near the central axis, the distribution is rather uniform on cross-sectional planes parallel to the front face. Considering the failure factor along the central axis, we observe the existence of three peaks, one on the surface, another rather sharp peak some distance beneath the surface, and a third, which is

blunter, deeper inside the body. At $t^* = 0.03$, Fig. 5.8.b shows that the second peak becomes the largest of the three; and the region of dominant failure factor now surrounds the central axis instead of being around the boundary. At a still larger time, Fig. 5.8.c, the second peak vanishes, or rather, merges into the third peak. Another region of high risk of failure is outside the heat flux area, at about $r^* = 2.0$ and close to the surface. However, the global maximum is still located on the central axis.

The time-dependent behavior of the failure factor distribution is better depicted in Fig. 5.9 where the failure factor at different radii is plotted at different times. Figure 5.9.a displays the failure factor distribution along the central axis for various values of the Fourier number. The peak at the surface is observed to be as large as the second peak for this specific case, and to increase consistently with time. At some later time, the second peak, rising very fast, becomes dominant. Unlike the first peak which is always located on the surface and the third peak which is almost invariant over the time range considered, the second peak starts from very close to the front face and migrates deeper into the body with time. At large times, the second peak is caught up by the third peak. The two finally merge together, pass through a maximum and decrease afterwards. Comparing Fig. 5.9.a with Fig. 5.6, we see that the failure factor distribution from the third peak and beyond follows exactly the same pattern as the longitudinal stress, suggesting that beyond a certain depth the longitudinal stress is the dominant contribution to the risk of failure. On the other hand, from Figs. 5.2 and 5.8 it is clear that the first peak on the surface is principally determined by the

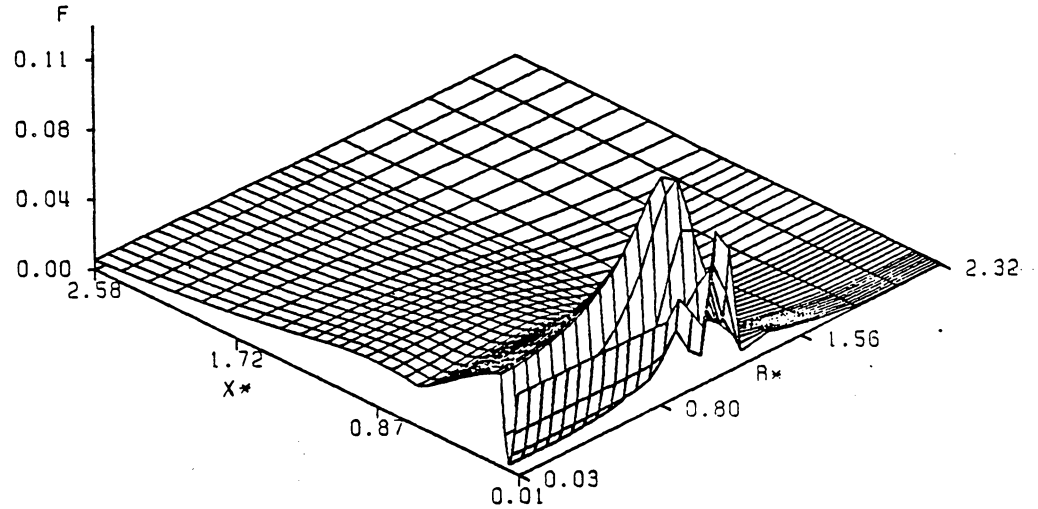

(a)

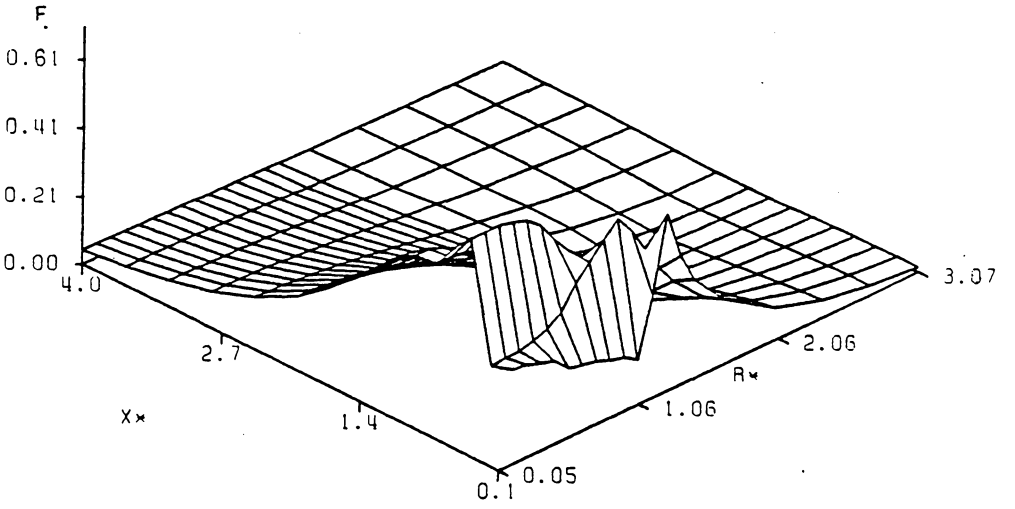

(b)

Figure 5.8 Failure factor distribution: (a) at t* = 0.001, (b) at t* = 0.03, and (c) at t* = 0.25 (next page).

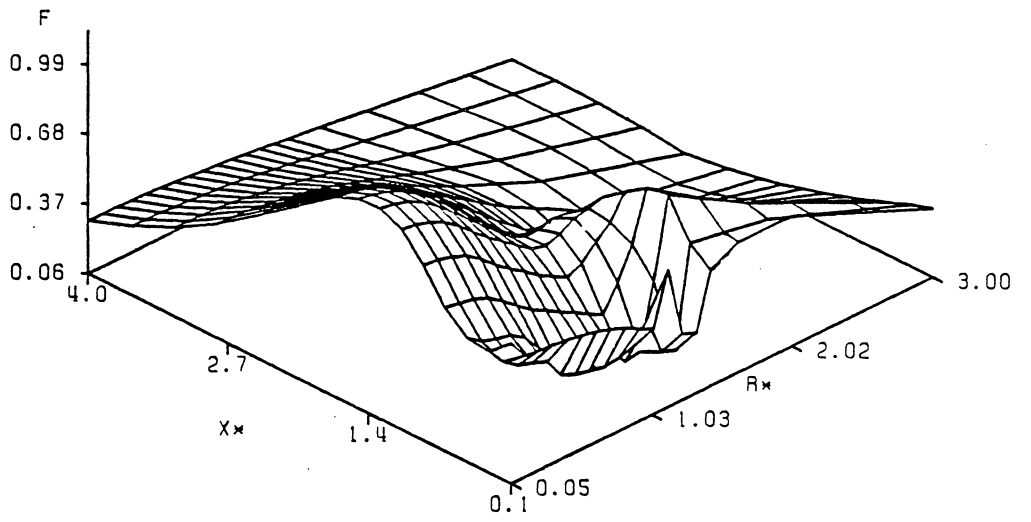

(c)

Figure 5.8 (Continued)

compressive longitudinal and tangential stresses, the longitudinal stress being always zero at the surface. For the second peak, the situation is more complex because the partial contribution of each stress component to the risk of failure varies with time and location. This will be discussed in more detail later.

In Fig. 5.9.a, the difference in relative magnitude between the first peak and the other two is seen to depend on the strength ratio. A higher strength ratio increases the relative magnitude of the first peak. For instance, doubling the strength ratio will double the magnitude of the first peak, i.e, the one at the surface, relative to the other two. In other words, the higher the strength ratio, the larger the first peak is relatively to the other two maxima. For the specific values of R_{th} and R_{st} used here, the first peak starts out at a rather high magnitude compared to the other two, increases rather slowly but steadily, and may become dominant at very large time when the other two peaks already pass their maximum and decrease in magnitude with time. However, this dominance of the failure factor on the surface at large times, beyond those considered in this study, is of little interest to us because the same dominance at small times can be achieved by choosing large values of R_{st}, as will be discussed shortly.

Figures 5.9.b-d show the failure factor distributions at radii r = 0.5, 1, and 1.5. The same time-dependent behavior as in Fig. 5.9.a is observed. However, the second and third peaks take more time before they merge together creating a flat plateau instead of a distinct peak. One noteworthy point to make is that on any cross-sectional plane bounded by $r^* = 1.5$ the failure factor on the central axis is largest. This allows

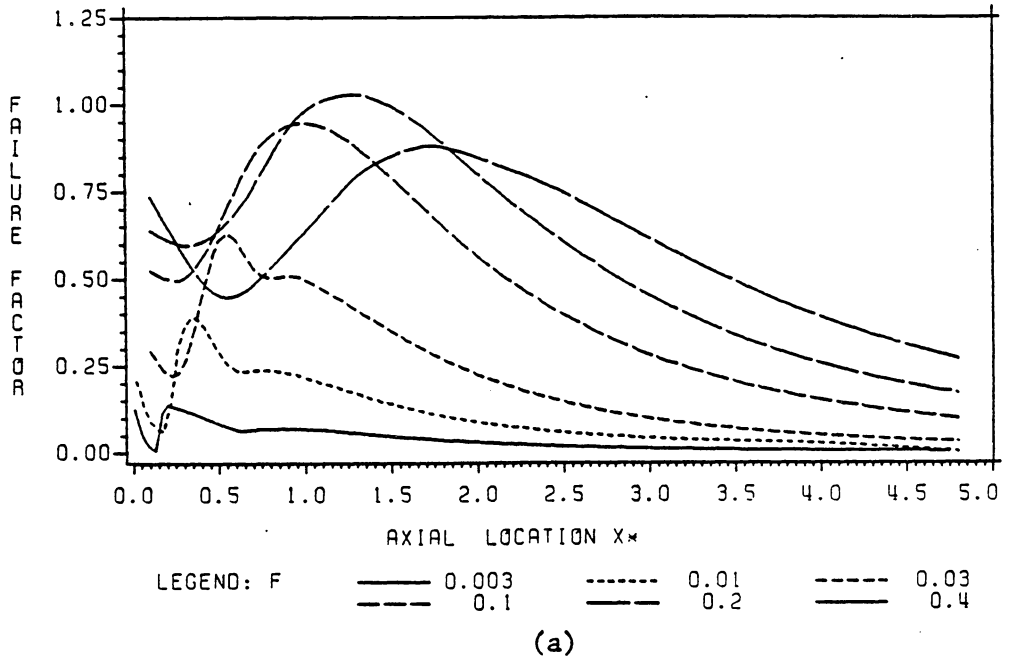

(a)

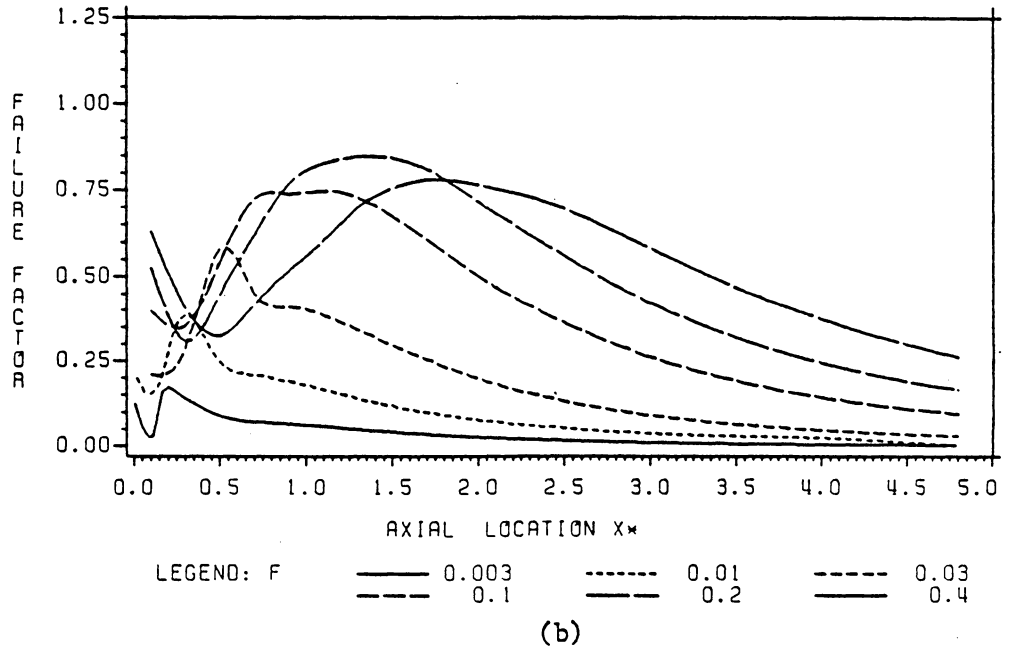

(b)

Figure 5.9 Failure factor parallel to the central axis (a) at r* = 0.0, (b) at r* = 0.5, (c) at r* = 1.0 (next page), and (d) at r* = 1.5 (next page).

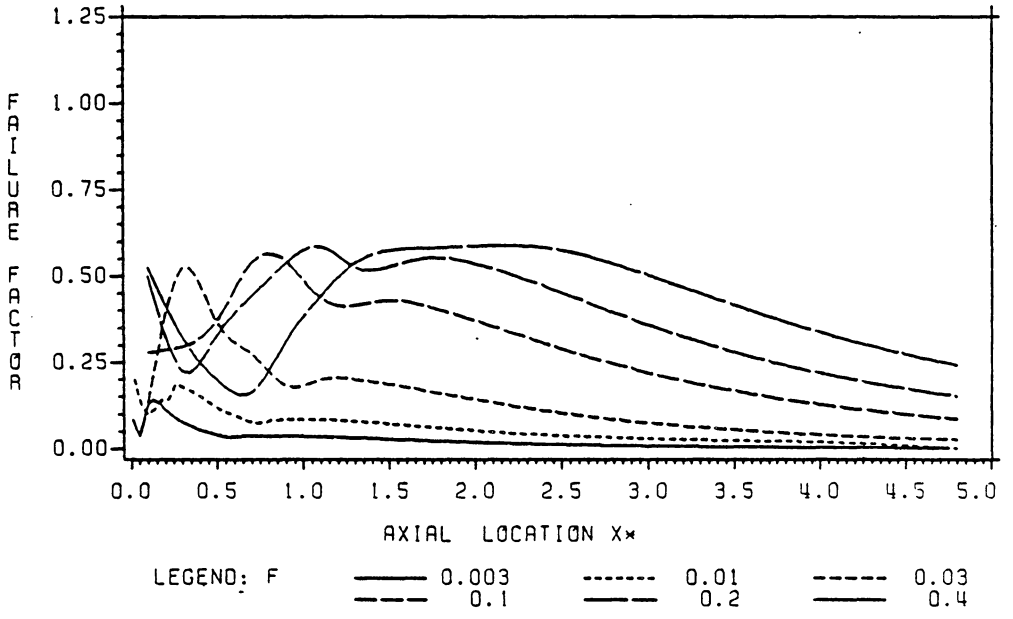

(c)

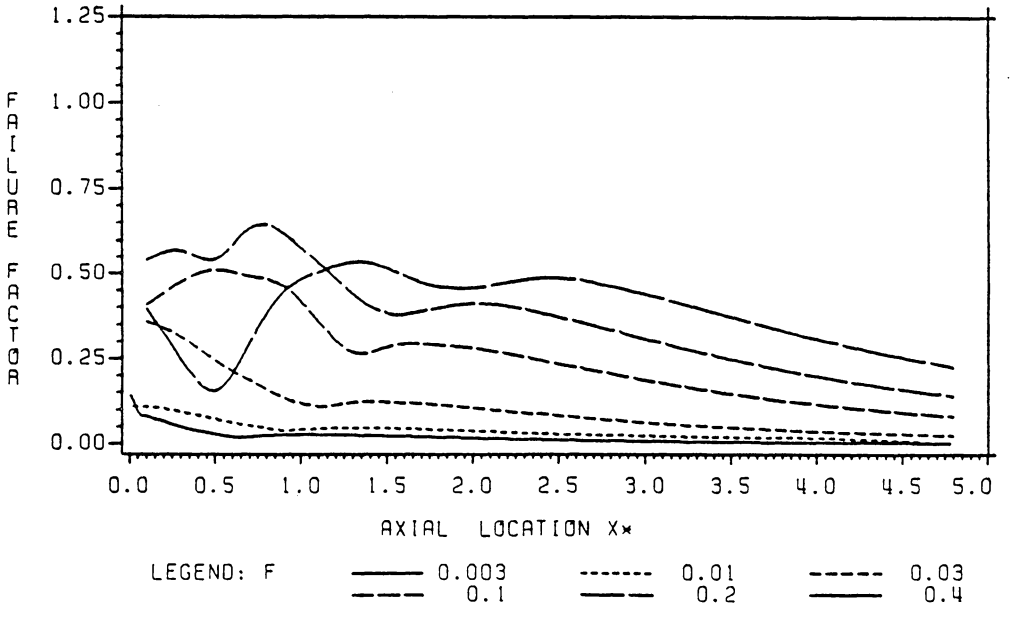

(d)

Figure 5.9 (Continued)

us to consider the failure factor along the central axis as a typical indicator of the risk of failure.

As previously mentioned, we know that the first peak, the one on the surface, is totally determined by the tangential and radial stresses, and that the third peak is largely determined by the longitudinal stress. On the other hand, in the region containing the second peak, failure is not determined by any single stress component but by the contribution of all stresses. The dominance of each stress component varies with time and location. The contribution of each stress component to the maximum failure factor is best observed in Fig. 5.10, where the profiles of the failure factor and stress components on the cross-sectional plane at the axial location of the second maximum are plotted at $t^* = 0.001$. At this time, the maximum failure factor on the central axis is located at $x^* = 0.11$. Comparing Fig. 5.10.a with Fig. 5.10.b, we see that close to the central axis, the failure factor is almost exclusively determined by the tensile radial and tangential stresses. Closer to the boundary of the heated area, the radial stress makes dominant contribution but those of the other stress components are not negligible. This makes the failure factor profile not parallel to that of either the radial stress or the tangential stress. A high risk of failure at the boundary of the heated area suggests that at short times after heating, if failure occurs, it initiates from the boundary and propagates towards the central axis.

Plotted in Fig. 5.11 are the failure factor and stress components at $t^* = 0.03$ and $x^* = 0.5$, the location of the maximum failure factor on the central axis. Close to the central axis, the contributions of the three stress components to the failure factor are comparable. At some

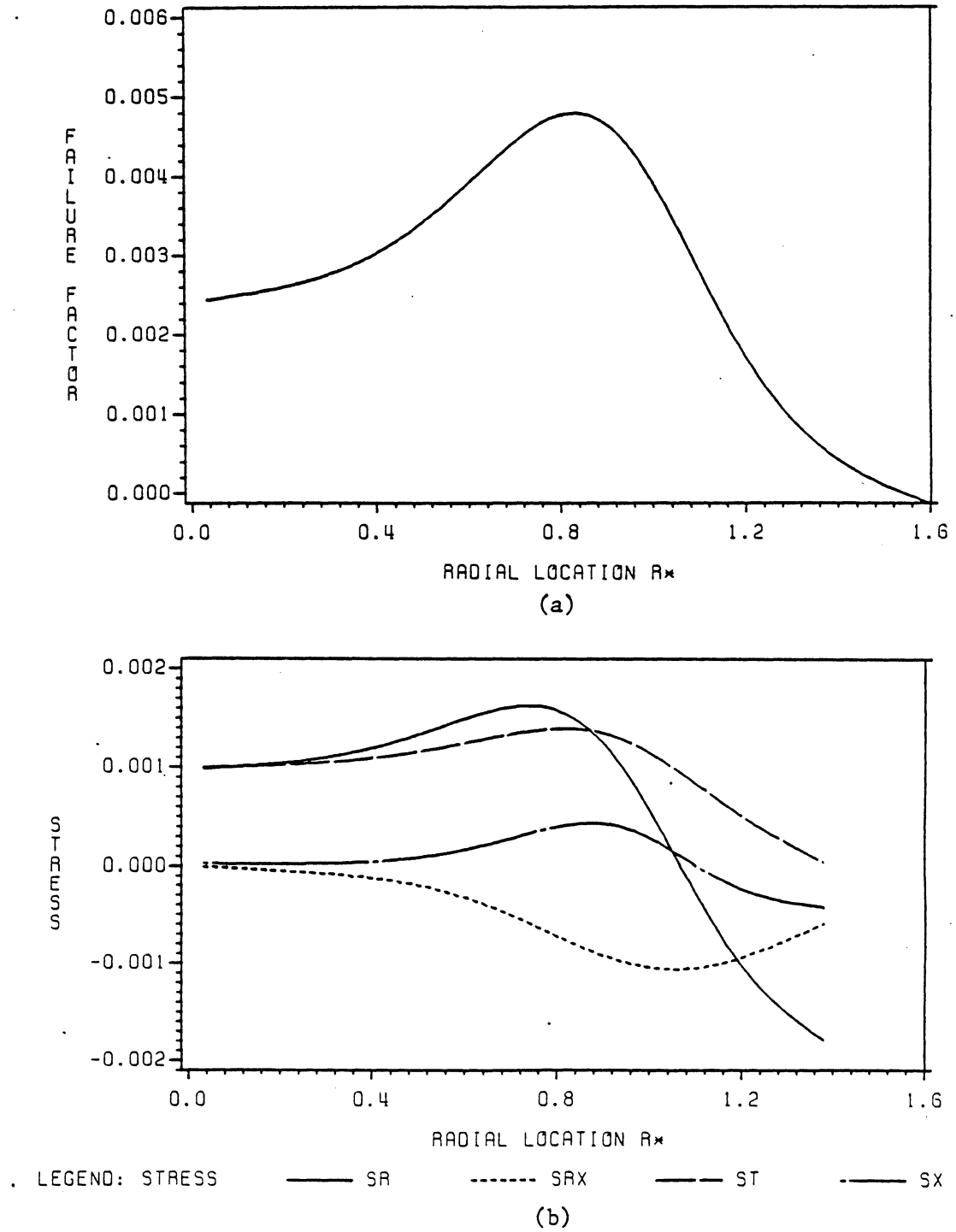

Figure 5.10 Cross-sectional failure factor and stressesat $x^* = 0.11$ and $t^* = 0.001$.

distance from the central axis, the tangential stress becomes more dominant. It is noted that along the central axis the normal stress components are principal stresses and the failure factor is determined solely by the largest stress component. In the other regions, the risk of failure is determined by the combined effects of several stress components. These combined effects of the different stress components make the failure factor profile more uniform across a cross-sectional plane than that of the dominant stress itself.

Figure 5.12 shows the cross-sectional profiles of the failure factor and the stress components at $t^* = 0.25$ and $x^* = 1.5$. In this case it is clear that the longitudinal stress is dominant. This is expected because we are in the region of the third peak, i.e., at a depth of R_q or more. The scales for stresses and failure factor are quite different in this figure, making the stress profiles look much flatter than that of the failure factor.

In general, for the second peak, the smaller the Fourier number the more dominant the tensile radial and tangential stresses are. As the heating proceeds, the relative contributions of all stress components become comparable. At even later time, the tensile longitudinal stress becomes dominant.

Based on this relative contribution of each stress component to the failure factor, we can classify the Fourier number into three typical regimes corresponding to small, intermediate, and large times after heating.

Referring to Fig. 5.9.a and from the above discussion, we note that in general the failure factor displays three peaks, each determined by

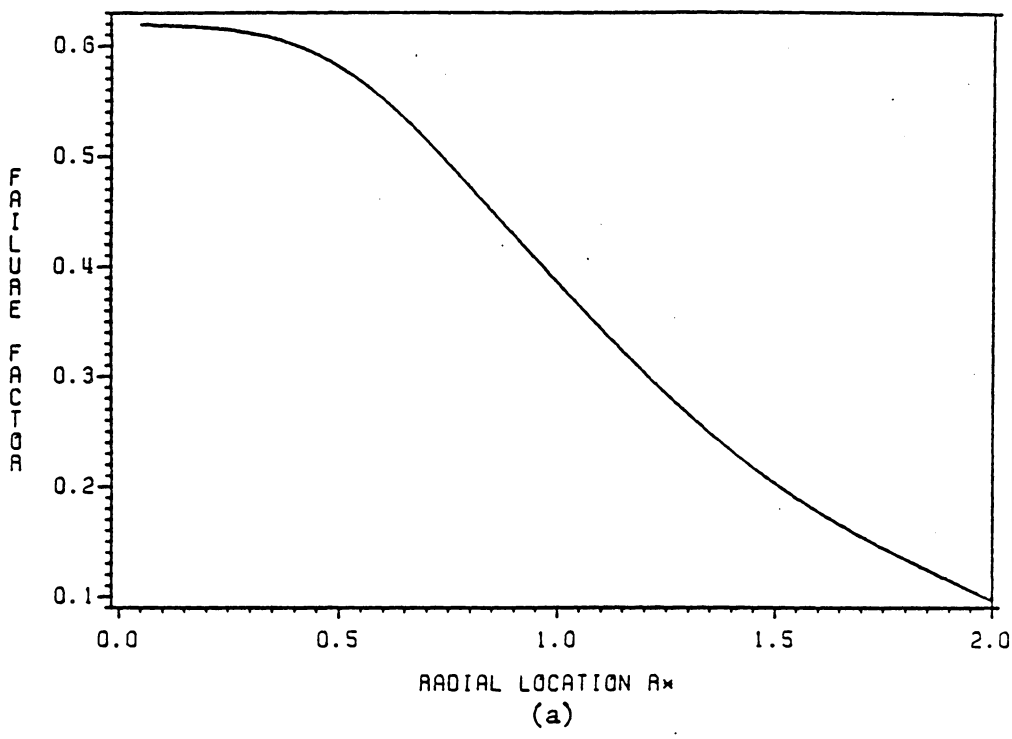

(a)

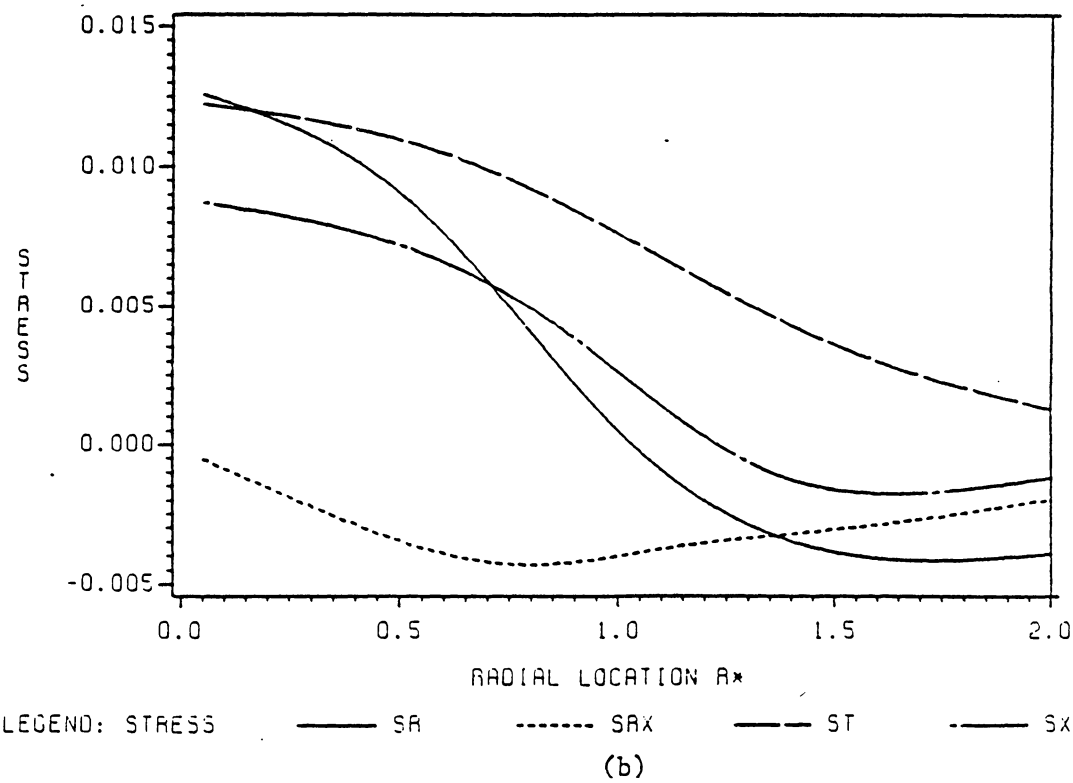

(b)

Figure 5.11 Cross-sectional failure factor and stressesat $x^* = 0.5$ and $t^* = 0.03$.

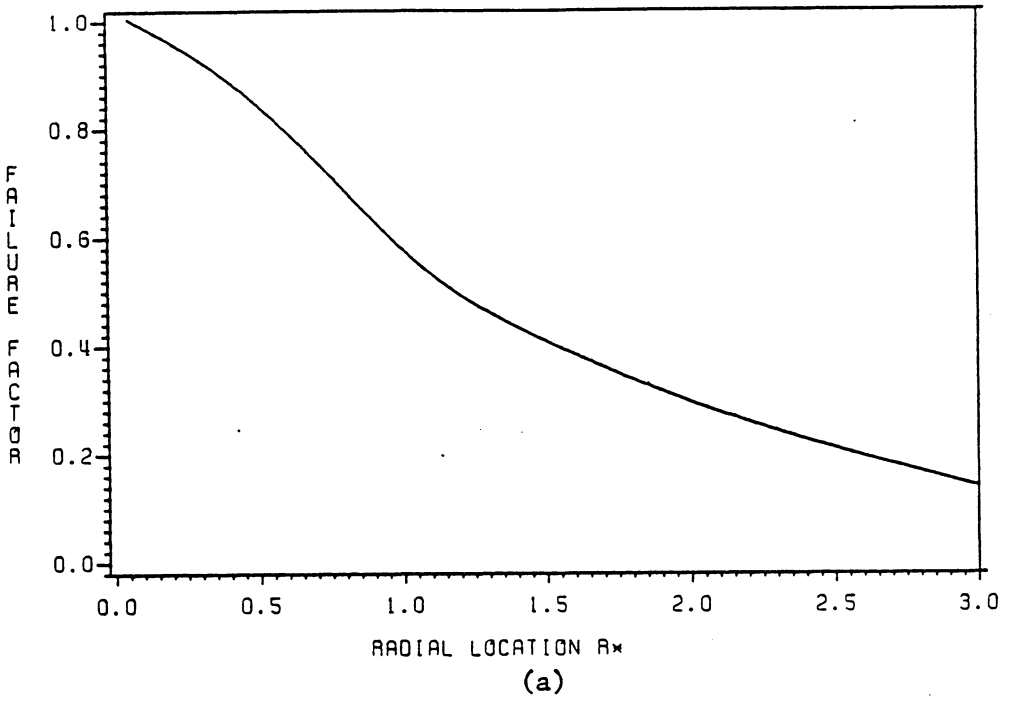

(a)

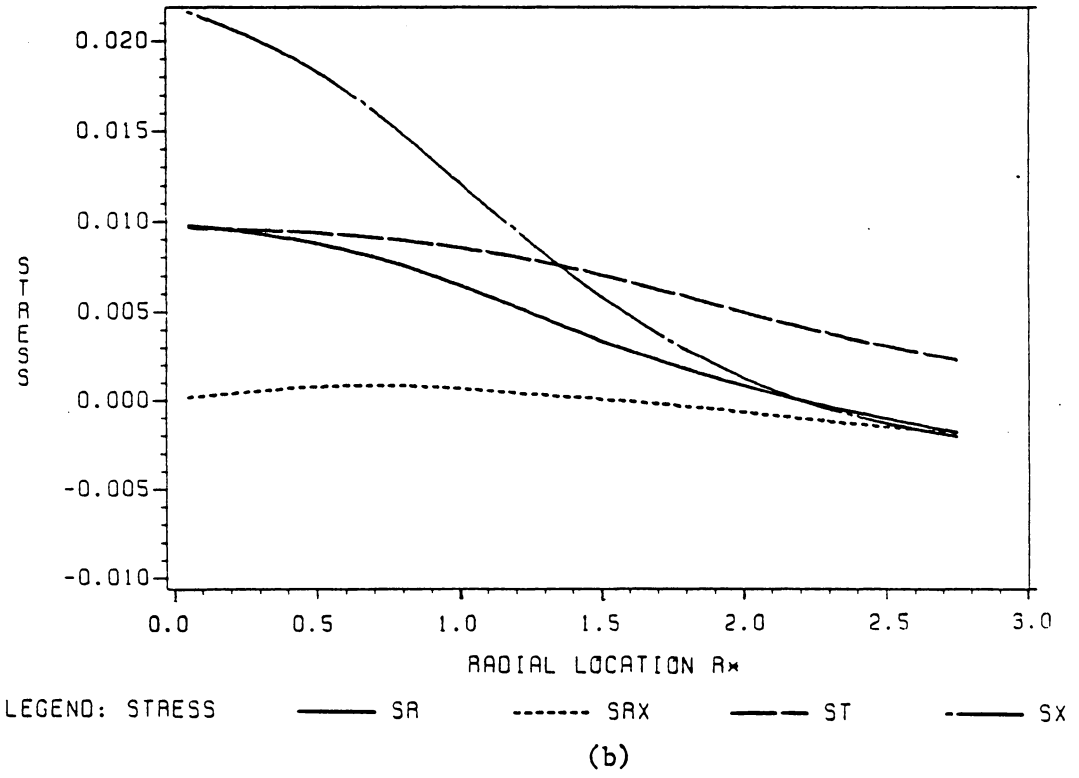

(b)

Figure 5.12 Cross-sectional failure factor and stressesat x* = 1.5 and t* = 0.25.

different stress components. These peaks are, however, not always distinct. At the very beginning of the heating, the first two peaks are very close to each other, and in the limit are not discernable from each other. We consider this as being in the small-time range. In this time range, failure is solely determined by the radial and tangential stresses. In other words, at small times a state of plane stress may be assumed as has often been done in the literature [22,30] by assuming unconfined heating over an infinite surface.

The second range of the Fourier number corresponding to intermediate times after heating is defined as the range in which the three peaks are clearly distinct, as seen in Fig. 5.8.b or 5.9.a. In this range, failure is determined by the combined effects of all stress components, as seen in Fig. 5.11, and the assumption of plane stress is invalid. The relative contribution of each stress component may vary but none is negligible. These combined effects of the stress components cause the sharp peak as observed in Figs. 5.8.b and 5.9.a.

Finally, the third range of the Fourier number corresponding to large times after heating is defined as the range in which the second and third peaks are not clearly discernable. In this range, failure is uniquely determined by the tensile longitudinal stress, as shown in Fig. 5.12.

The above classification is not rigorous in the sense that the borderlines between the defined ranges cannot be accurately determined. However, we will arbitrarily suggest nominal values to use in determining the different ranges to ease the discussion to come. Based on Fig. 5.9.a and numerical results at times other than those plotted in Fig. 5.9.a, we suggest that the range of small times corresponds to Fourier numbers

less than 0.001. Similarly, the range of intermediate t* is between 0.001 and 0.05. At t* = 0.05 the two maxima start to merge together. For t* beyond 0.05 we are in the range of large times.

The above temporal classification of the Fourier number has its spatial equivalence. We already mentioned that the first peak is always located on the front face. Therefore, in the range of small times, the second peak is also very close to the front face. In the range of large times, the second peak must be about one radius beneath the surface because the third peak is always about one radius R_q deep. When the second peak is in the intermediate region, we consider it to be in the intermediate time range. We can determine the spatial boundaries corresponding to the above suggested temporal boundaries between the three ranges by determining the location of the second maximum for each of the above nominal Fourier numbers. The first range is found to be between x* = 0 and 0.01, the second between 0.01 and 0.8, and the third from 0.8 and beyond.

It should be reminded again that these values are only suggestive. For values that are too close to the above suggested boundaries, we will consider them as being in an ambiguous region. Note that although we described Fig. 5.2 as typical of small times, it is actually only approaching the small time range from above, and may well be in the ambiguous region. Had a smaller Fourier number been chosen, the first and second maxima would not be discernable for illustration.

For design, the maximum failure factor and its location on the central axis is plotted in Fig. 5.13 as a function of the Fourier number. Two curves are presented, denoted by (i) and (ii). Curve (i) depicts the

larger of the second and third maxima, called F_{in}, as a function of time for $R_{st} = 0.05$ and $R_{th} = 0.02$. Curve (ii) depicts the failure factor on the surface, F_s, as function of time. The relative magnitudes of these two curves depend on the strength ratio R_{st}. Curve (i) is observed to increase with time, have a peak at about $t^* = 0.15$, and decrease afterwards. Curve (ii) increases sharply at first and keeps increasing at a lower rate.

A noteworthy point to underline is that the maximum failure factor represented by curve (i) is totally determined by the tensile stresses beneath the surface, either radial, tangential, or longitudinal, and the one by curve (ii) by the compressive stresses on the surface. Hence, a higher strength ratio increases the magnitude of curve (ii) relatively to curve (i). This is because a higher strength ratio corresponds to a lower compressive strength and thus higher risk of failure by compression. Although Fig. 5.13 is plotted for the specific case of $R_{st} = 0.05$ and $R_{th} = 0.2$, the same plot can be used for other values of R_{st} and R_{th} with appropriate rescaling. For example, if R_{th} is half the one of Fig. 5.13.a, i.e., $R_{th} = 0.01$, both curves must have their magnitude doubled, or equivalently, the scale on the vertical axis must be halved. This is also equivalent to halving the critical value of the failure factor, with other things fixed and with the critical value for the specific case of Fig. 5.13.a being unity. Changing the nominal value of the critical failure factor turns out to be most convenient because no rescaling of the plots is needed.

If in addition, the strength ratio is also doubled, the magnitude of curve (ii) should also be doubled. It should be remembered that the

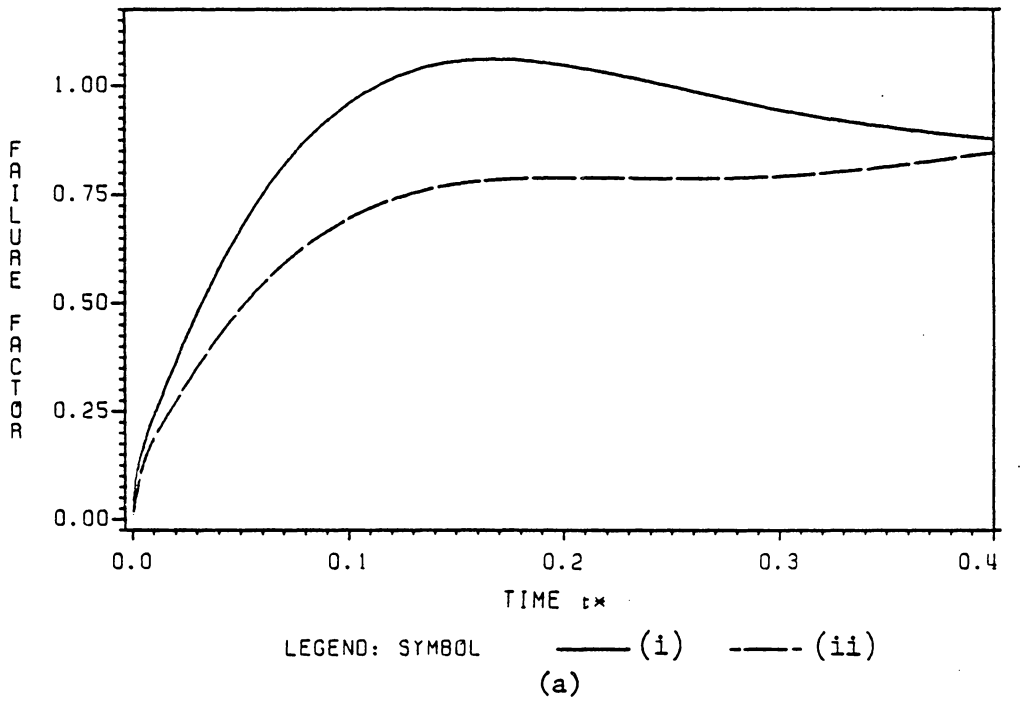

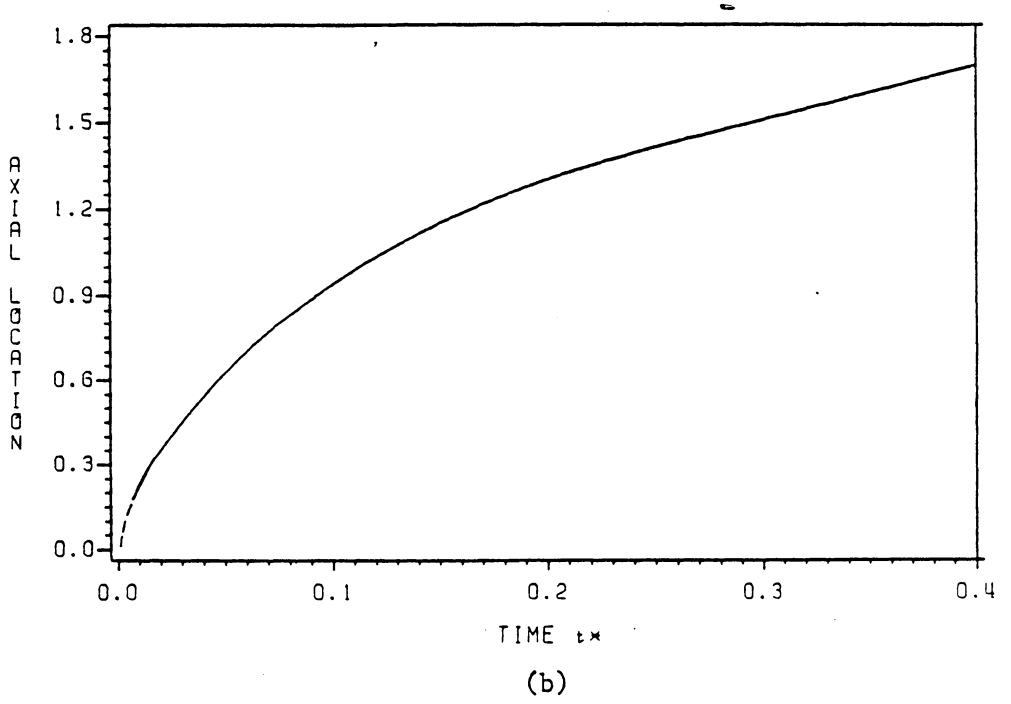

Figure 5.13 Maximum failure factor on the central axis: (a) magnitude of the larger of the second and third peaks (i) and magnitude of the first peak (ii), and (b) location of the larger of the second and third peaks as function of time.

strength ratio only determines the relative magnitude between the two curves, not their absolute values.

The location of the larger of the two peaks beneath the surface along the central axis is plotted as a function of time in Fig. 5.13.b. This plot allows us to estimate the location of the maximum failure factor and thus predict the spall thickness and the spalling rate.

Figure 5.14 gives the non-dimensional surface temperature at $r^* = 0$ as a function of time. It can be used to determine the spalling quality. If the surface is close to the melting point of the material, a mixture of fusion and spalling may be expected. At temperatures well above the melting point of the material, there is no spalling but pure fusion.

Figure 5.15 displays the location for fixed temperature rises along the central axis as function of time. This information is needed to determine the initial state of the following thermal phase. If the temperature of the newly exposed surface is only negligibly higher than the bulk temperature of the object, all the subsequent phases are almost identical to the first and no more analysis needs be done. The same information as in Figs. 5.14 and 5.15 can be obtained from Fig. 5.7.

For convenience, the regression of the curves in Figs 5.13-5.15 are given below:

Failure factor inside the body, curve (a) of Fig. 5.13.a:

$$F_{in} = 0.798 - 0.74E8(0.145 - t^*)^{9.5}, \quad 0.5E\text{-}3 < t^* < 0.2, \qquad (5.2.1)$$

Failure factor on the surface, curve (b) of Fig. 5.13.b:

$$F_s = 0.742 - 0.282E4(0.25 - t^*)^{6}, \quad 0.5E\text{-}3 < t^* < 0.3, \qquad (5.2.2)$$

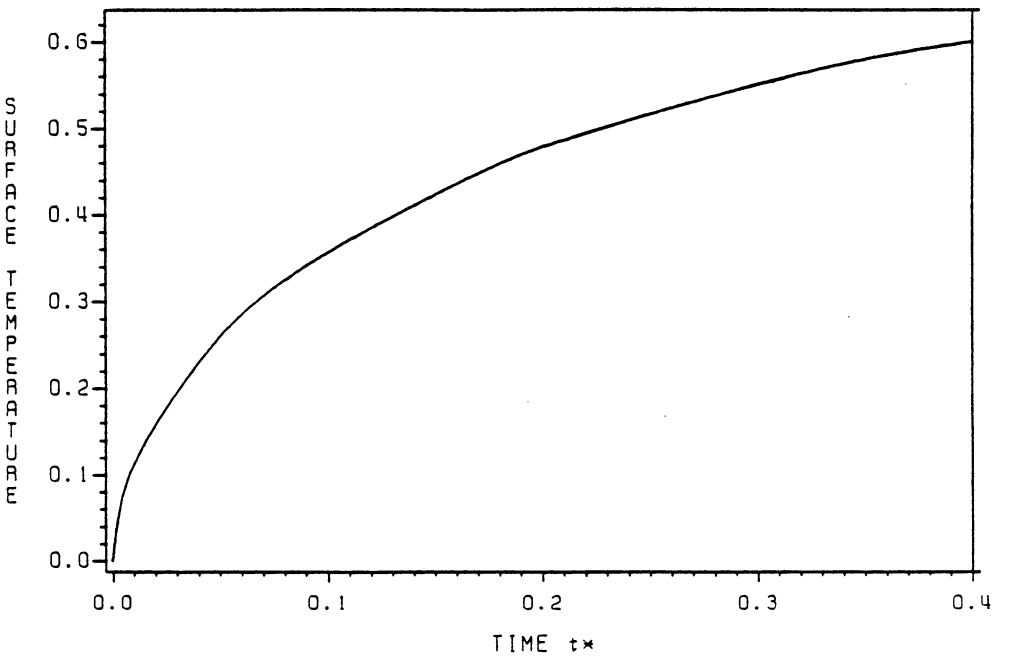

Figure 5.14 Non-dimensional surface temperature as function of time.

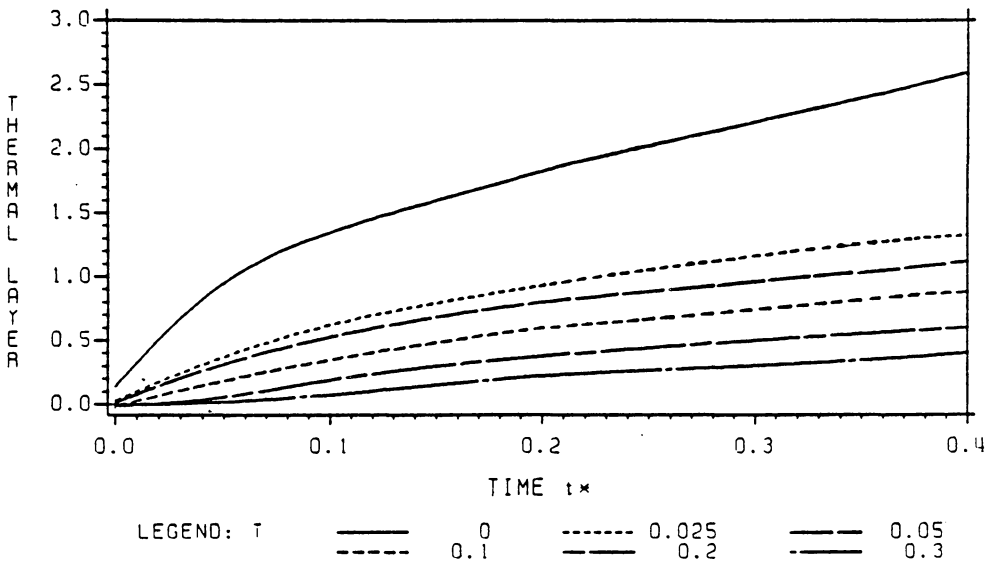

Figure 5.15 Thermal layer on the central axis as function of time.

Location of F_{in}, Fig. 5.13.b:

$$x_{in}^* = -0.343E\text{-}2 + 2.6t^{*0.45}, \quad 0.2E\text{-}3 < t^* < 0.4, \tag{5.2.3}$$

Surface temperature, Fig. 5.14:

$$T_s^* = -7.11E\text{-}2 + 0.965t^{*0.35}, \quad 0.5E\text{-}3 < t^* < 0.4, \tag{5.2.4}$$

Thermal layer, first curve in Fig. 5.15 (T = 0):

$$\zeta^* = -0.254 + 4.03t^{*0.4}, \quad 0.5E\text{-}3 < t^* < 0.4. \tag{5.2.5}$$

The subscripts "in" and "s" refer to the maximum and the peak on the surface, respectively.

The maximum error in all the above regressions is less than 8 percent, except for F_{in} which has a maximum error of 15 percent at the upper end.

The application of the above results is best illustrated with an example.

3. EXAMPLE

The following example will illustrate the design application of the results in the previous section to predict the spalling rate of materials.

In a jet-piercing operation on granite, predict the spalling rate for a heat flux of intensity $q'' = 5x10^4$ watt/m^2 confined to a circular area of radius $R_q = 0.01$ m. The bulk temperature of the rock body is at ambient temperature $T_o = 25^oC$. The material properties of granite are obtained from [51,52,61], and are given in Table 5.1.

Table 5.1 Material Properties of Granite

MATERIAL PROPERTIES	NOTATION	NOMINAL VALUES	UNITS
Thermal Conductivity	k	2.	$W/m^{\circ}C$
Lin. Thermal Exp. Coef.	α	2.E-5	$1/^{\circ}C$
Heat Capacity	C_p	820	$J/kg^{\circ}C$
Density	ρ	2640	kg/m^3
Young's Modulus	E	6.E10	N/m^2
Poisson's Ratio	ν	0.2	
Compressive Strength	S_c	1.E8	N/m^2
Tensile Strength	S_t	1.E7	N/m^2

From the above table we can compute the thermal diffusivity, the strength ratio and the thermal stress resistance as follows.

Thermal diffusifity: $\kappa = k/\rho C_p = 9.24E\text{-}7\ m^2/s$,

Strength ratio: $R_{st} = S_t/S_c = 0.1$,

Thermal stress resistance: $R_{th} = (k/R_q q'')S_t(1-\nu)/E\alpha = 0.026$.

Since $R_{th} = 0.026$, or 1.3 times greater than the one used to obtain the results in the previous section, the critical value of the failure factor must be up-scaled by a factor of 1.3 from unity to 1.3. From Fig. 5.13.a we see that the failure factor never reaches the critical value for failure. Therefore no spalling is expected and melting would occur if the rock were heated long enough.

To remedy this, the intensity of the heat flux is doubled to 10^5 J/m^2. The thermal stress resistance is now 0.013 and the critical value of the failure factor is 0.65. First let us consider the risk of failure on the surface. Since the strength ratio is now 0.1, twice the one used in Fig. 5.13.a, the relative magnitude of curve (b) in Fig. 5.13.a must

be doubled. From Fig. 5.13.a it is observed that the failure factor at the surface reaches the critical value at a time of 3.2 s. However, since the first maximum is highly localized to the surface, no spalling is expected.

We next consider the risk of failure in regions beneath the surface. By inspecting curve (a) of Fig. 5.13.a and Fig. 5.13.b, we observe that this critical value is reached at $t^* = 0.04$, or at an actual time of $R_q^2 t^*/\kappa = 4.3$ s, and $x^* = 0.52$ or $x = x^*/R_q = 5.2$ mm. This value of t^* is in the ambiguous region between intermediate and large times. The maximum failure factor on the central axis is therefore highly localized and no spalling is expected.

From Fig. 5.14, the non-dimensional surface temperature rise at $t^* = 0.04$ is $T^* = 0.24$, corresponding to an actual temperature rise of $(T^* q'' R_q)/k = 120^{\circ}C$, well below the melting point of granite, which is between 1000 and $1200^{\circ}C$ [56]. Finally, Fig. 5.15 shows that the temperature at $x^* = 0.52$ is 0.005 or $3^{\circ}C$ above ambient temperature, and the corresponding non-dimensional thermal layer is 0.56, or 5.6 mm in nominal value.

Since $q'' = 10^5$ watts/m^2 lands us in the ambiguous region between two ranges of the Fourier number, we will use another value of q", say 2×10^5 watts/m^2. Following the same line of computations as before, the results for $q'' = 2 \times 10^5$ watts/m^2 are computed and listed below:

Thermal Stress Resistance: $R_{th} = 0.065$,

Critical Value of F: $F_c = 0.325$,

Time at F_c: $t_c^* = 0.016$, $t = 1.7$ s,

Location of F_c: $x_c^* = 0.3$, $x = 3$ mm,

Surface Temperature: $T_s^* = 0.14$, $T_s = 140 + 25 = 165^oC$,

Temperature at F_c: $T^* = 0.005$, $T = 5 + 25 = 30^oC$,

Thermal Layer: $\zeta^* = 0.45$, $\zeta = 4.5$ mm.

As can be seen, with $q'' = 2x10^5 watts/m^2$ we are sure to be in the region of intermediate time range and would expect spalling to occur. The spall thickness may be approximated to be of the same size as the depth where the failure factor first reaches the critical value. That is, the thickness can be approximated to be 3 mm for a heat flux of intensity $2x10^5$ watts/m^2 over an area of radius 1 cm. From Fig. 5.8.b, the radius of the spall may be estimated to be $1.5R_q$ or 1.5 cm.

It can be seen that the same non-dimensional results can be obtained by modifying R_q instead of q". The actual results are, however, not the same. For instance, if we double R_q instead of q", the location of critical failure factor is twice and the actual spalling time is four times those obtained by doubling q".

There are two definitions of the spalling rate used in the literature. The first is the linear spalling rate defined as the progression rate of the heat source and in average can be computed as

$$R_l = \frac{\text{spall thickness}}{\text{spalling time}}. \qquad (5.3.1)$$

The second is the volumetric spalling rate defined as the volume of material removed per unit time, or

$$R_v = \frac{(\text{spall thickness})(\text{cross-sectional area of spall})}{\text{spalling time}}. \qquad (5.3.2)$$

The linear and volumetric spalling rates for this example are 0.007 m/s and 2.2×10^{-7} m^3/s respectively, assuming a spall radius of 1 cm.

4. DISCUSSION

First we need to explain our definition of the thermal stress resistance because it is defined differently from those used by many other authors. In most cases, thermal stress resistance is defined as a material property [22,28,30-34,38]. In addition to material properties, our definition also includes two external factors: q'' and R_q. The thermal stress resistance thus defined is an operational parameter rather than a material property. This definition is justified by observing that the temperature is proportional to q''/k [35], i.e., a change in k corresponds to a change in q'', with thermal diffusivity remaining constant. A larger q'' or a smaller k enhance the spallability of the material in the same manner. The radius of the heat flux area R_q is in this case the characteristic dimension to use because all other dimensions are approximately infinite. R_q is the only factor that affects both the spallability and the spalling rate. A change in R_q corresponds to a change in q'' or k and also a change in κ.

Another difference is that our definition does not include the thermal diffusivity κ. The reason is that κ by itself, i.e., with k kept constant, does not influence the tendency to spall nor the spall size and shape, but only determines the time required for spalling to occur. For instance, doubling κ will halve the spalling time because only half the time is now needed to reach the same temperature profile, hence the same

stress state. This point has been discussed by Preston [48]. Since we deal only with non-dimensional quantities, the effect of the thermal diffusivity is buried in the Fourier number and is therefore immaterial in the analysis and the non-dimensional numerical results.

The observation that, in reality, thermal diffusivity does affect the tendency to spall implicitly accounts for the effects of k, which is the actual parameter that influences the spallability of materials. For this reason, k has been included in our definition of the thermal stress resistance, instead of κ.

The thermal stress resistance alone does not give enough information on the spallability and the spalling rate of a material but needs to be used in conjunction with the strength ratio because failure in the case of confined heating may be either in tension or compression, depending on the time range in which spalling occurs and on the strength ratio. The strength ratio is therefore needed.

In fact, our classification of the Fourier number into different time ranges is implicitly based on the interplay between tensile and compressive stresses.

As mentioned before, in the first range of Fourier numbers, failure is more likely to occur near the surface and to be caused by the tangential and radial stresses. Whether failure is by compression or tension, or both, depends on the strength ratio. A high strength ratio may lead to failure in compression with the material on the front face disintegrating into dust. At a low strength ratio, failure is more likely in tension, caused by the tensile radial or tangential stresses at some distance beneath the surface, resulting in very thin spalls. At some

intermediate strength ratio, both modes of failure may co-exist. The compressive strength therefore plays an important role in determining the spallability of a material in the small time range. Similarly, the tensile strength determines the spallability in the other two time ranges. At intermediate times, the risk of failure is caused by the combined effects of all stress components that are all tensile. At large times, the risk of failure is solely determined by the tensile longitudinal stress.

It is of interest to note that the combined effects of the stress components at intermediate times are rather localized to a plane parallel to the front face, creating a more or less sharp peak as observed in Figs. 5.2.b and 6.8.

Although the compressive strength does not contribute to the second peak of the failure factor distribution, that does not mean its role is unimportant in the actual spalling process. When the first and second peaks are comparable in magnitude, cracks may initiate at the surface at the same time as a plane of high risk of failure develops beneath the surface. These cracks on the surface may propagate inwards and help break the spall loose.

It is noted that the strength ratio of most rocks is between 0.05 and 0.1, or the compressive strength is from 10 to 20 times the tensile strength. In Fig. 5.13, we observe that for R_{st} greater than 0.07 the failure factor at the surface, curve (ii), is almost always larger than those inside the body, curve (i). This suggests continuous disintegration of rock occurs at the surface until F_{in} reaches the critical value, resulting in a spall of finite thickness. This finite thickness can be approximated with Fig. 5.14 under the assumption of a negligible

progression rate of disintegration. Under this circumstance, two modes of spalling may coexist, in forms of thin dust and spalls of finite thickness, as observed in the literature [22,51].

We should keep in mind that failure does not depend only on the local stress state but also on the overall distribution of stress in the body as expressed in Weibull's statistical theory of failure. It is therefore suggested that the first peak, which is highly localized to the surface, is not likely to cause spalling, nor does the third peak, which is localized to the central axis.

Therefore, spalling is most likely to occur in the intermediate time range for a reasonably high-intensity heat flux due to tensile stresses. From Fig. 5.8.2, the plane of high risk of rupture is observed to be more or less parallel to the front face and intersected by another plane of high risk of rupture, at some angle to the surface. This suggests a thin spall with bevelled edge as observed in reference [51]. At larger spalling times, the spall will assume a more curved shape. This is also noticed by Gray in [22].

The complexity of the interplay between different stress components in causing failure as described above suggests that assuming failure by any single stress component is over-simplistic. For instance, assuming failure by compressive stress on the surface is only valid at the very beginning of the heating and for certain strength ratios, and does not predict spalls of finite thickness. The assumption of failure by tensile longitudinal stress is also unrealistic for the case of confined heating because, as already mentioned, the longitudinal stress has the peculiar behavior of having a maximum at a depth of about R_q even at the very be-

ginning of the heating. If failure were by longitudinal stress alone, a very high intensity heat flux would instantly produce a spall of thickness of about R_q, which is unreasonable.

We have no satisfactory explanation for this behavior of the longitudinal stress. Jaunzemis and Sternberg's analytical results [27] also show the same behavior of the longitudinal stress for a similar case of heating, namely, heating confined to an infinitely long strip on the surface. The authors did not offer any explanation. Emery [19] also reported this unexpected behavior of thermal stresses without explanation.

We speculate that this behavior reflects the boundary effects, i.e., the effects from the thermal boundary at $r = R_q$. More work needs be done to get a satisfactory explanation for this seemingly significant behavior of the longitudinal stress.

This behavior of the longitudinal stress implies that maximum stress may occur in the region well beyond the thermal layer, which contradicts Kienow's conjecture that thermal stress is proportional to the second derivative of the temperature [12]. Although Kienow's conjecture only applies for one-dimensional cases, i.e., at very short times after heating, such a large and fundamental discrepancy at larger times is not expected.

With the modified Coulomb-Mohr theory used here, the location of maximum failure factor is at about the same depth as the thermal layer, that is, in a region where the curvature of the temperature distribution is almost nil. The example gives a temperature rise of only $5^{\circ}C$ for the newly exposed surface. This also agrees with observations made in ref-

erence [51]. Each subsequent thermal phase can therefore be considered as almost identical to the first, if no fusion is present. It is observed in the literature [22] that with partial fusion the continuous spalling rate is somewhat less than the initial spalling rate.

It is also interesting to note that, from the example, when the failure factor first reaches the critical value, the surface temperature varies little for a large change in heat flux intensity. This also agrees with observations made by Gray [22]. Based on Soles and Geller's experimental data, Gray observed that the temperature rise of the surface required for spalling is almost independent of the rate of heating. The surface temperature measured for a wide variety of rocks ranges between 150 and 350^{o}C, compared to a surface temperature of 165^{o}C (140 + 25) from the example. Thirumalai [56] also experimentally obtained a surface temperature at spalling between 167 and 350^{o}C for a variety of quartzite and granite. The explanation for this quasi-independence of the surface temperature on the heating rate is that, at higher heating rate, failure occurs sooner, allowing less time for the surface to be heated. This counter-balances the higher rate of increase in surface temperature.

We can also compare the ratio between the thickness and the radius of the spall obtained in the example with that observed in the literature [22]. From the example, this ratio is computed to be 0.10 (3mm/30mm), compared to a ratio between 0.04 and 0.08 for granite in a gas-exhaust tunnel, as observed in [22]. The discrepancy may result from differences in geometrical configuration, heating regime, and type of rock. The discrepancy may also come from our assumption that failure occurs at the time and location where the failure factor first reaches the critical

value without regards to rock mechanics and the overall stress distribution. We know that after crack initiation the state of stress is drastically changed [20,22], and the propagation of cracks can only be determined by a more appropriate approach [23,42].

From the numerical results, attempts can also be made to study the effects of material properties and external factors on some of the performance parameters often used in jet-piercing operations [50,51]. These are linear and volumetric spalling rates and energy input per unit volume of material removed. The linear and volumetric spalling rates have been mentioned in the example. They can be rewritten in terms of x_c^* and t_c^* as $S_l = (x_c^*/t_c^*)(\kappa/R_q)$ and $S_v = (x_c^*/t_c^*)r_c\kappa/R_q$, assuming a cylindrical spall shape of thickness x_c and radius r_c.

It is observed that for the same non-dimensional parameters, the linear spalling rate is improved by reducing the radius of the heat flux area and by increasing the thermal diffusivity. The volumetric spalling rate only depends on the thermal diffusivity.

Another operational parameter is the energy input per unit volume of material removed, ε, defined as the ratio of total energy input for spalling over the volume of the spall:

$$\varepsilon = \frac{q''t_c}{x_c} \quad . \tag{5.4.1}$$

Equation 6.4.1 shows that the energy efficiency cannot be improved via changes in the area of the heat source, but can be improved by changes in the intensity of the heat source and the material properties which determine the spalling rate x_c/t_c.

In terms of non-dimensional quantities evaluated at spalling, ε can be rewritten as $\varepsilon = (t_c^*/x_c^*)(q''R_{q/\kappa})$, where the non-dimensional term (x_c^*/t_c^*) can be evaluated from the regressions given in section 5.2 as follows: From the material properties and the external factors q'' and R_q, we can determine the critical value for the failure factor, F_c. Equate F_{in} from Equation 6.2.1 with F_c to solve for t_c^*, the time at which the failure factor first reaches F_c. Knowing t_c^* we can compute x_c^* using Equation 6.2.2 and hence the above ratio.

Although the above expressions are obtained for a cylindrical spall shape we expect these expressions would help predict the performance of actual operations with the introduction of a proper correction factor which must be experimentally measured.

As conclusion, we see that for the case of confined heating, failure is not determined by any single stress component but by a rather complex combination of all stress components. The relative contribution of each component varies with time, location, and strength ratio. To cope with this complex stress state we have used the modified Coulomb-Mohr theory of failure.

The model we use gives results that are comparable to experimentally observed facts and data. The model helps explain the facts that the temperature rise for spalling is almost invariant with the heating rate, and that the plane of high risk of failure is located far beyond the region of steepest temperature gradient, yielding a temperature of the newly exposed surface only negligibly higher than the bulk temperature of the body. The surface temperature rise predicted is within the range of observed data for a variety of rocks. The temperature rise at the newly

exposed surface is also negligible for all the cases considered, implying that the spalling process reaches steady-state within the first few thermal phases.

At moderate heating rates, the model suggests thin spalls with bevelled edge and increasingly curved back face for larger spalling times, which agrees with on-site observations. Under very intense heating, disintegration may occur right on the surface in form dust. At rather low heating, disintegration may again occur at the surface after a long heating time, possibly with crack formation deep inside the body from the central axis. However, in this case, fusion is more likely.

The plots in Figs. 5.13-5.15 with their associated regressions can be used in design to predict the operational conditions to cause spalling in a given material. For given operational conditions, it is also possible to predict the time of spalling, if spalling ever occurs, the thickness and the size ratio of the spall, the surface temperature, and the temperature at the newly exposed surface. The quality of spalling can also be estimated by considering the surface temperature. If it is well below the melting point of the material, clean spalls would be expected. The temperature of the newly exposed surface also allows us to conjecture on the state of the next heating process. If the newly exposed surface is at a temperature not appreciably higher than the bulk temperature of the material, all subsequent spallings can be predicted based on the first spalling.

From the plots and their regressions it is also possible to tentatively compute the optimal operational conditions for a specific type of material.

VI. CONCLUSIONS AND SUGGESTIONS

1. CONCLUSIONS

In the previous three chapters, results that can be used in analysis as well as in design of thermal spalling have been obtained. The technique of fictitious boundary conditions has been specifically developed for linear heat-conduction problems with moving boundaries and/or with stepwise changes in boundary conditions. The technique has many merits. It is more computationally efficient and has less round-off error than the integral transform technique [44], or any exact technique, as the number of thermal phases considered becomes large. The technique has less truncation error and more consistent accuracy than the approximate initial condition technique or the integral method [44]. The other advantages of the technique are its ease of implementation and the fact that it offers a different interpretation of the physical system under study.

Thermal spalling in rocks under jet-piercing operations has been studied with a finite element model. The results show that there are three modes of failure. Failure shortly after heating is principally determined by the compressive radial or tangential stresses. On the other hand, failure at large times after heating is principally determined by the tensile longitudinal stress. At intermediate times, the tensile radial, tangential, and longitudinal stresses all contribute to failure.

The results based on the modified Coulomb-Mohr theory of failure suggest that under intense heating, the rock disintegrates in the form

of thin dust as observed in reference [51]. Under moderate heating, the spalls are in the form of thin disks bevelled at the edge. The spalls become thicker and more curved in the back as the heating intensity is decreased. At very low heat flux, there is partial or total fusion instead of clean spalling. These results agree with experimental observations [51]. .

The temperature rise at the heated surface upon spalling was found to be almost invariant with heating rate, in agreement with experimental results [22]. This temperature rise in a case study on granite was found to be within the range experimentally observed [23,56]. The temperature rise at the newly exposed surface was computed to be negligible. This indicates that the spalling process reaches steady state in the first thermal phase, in agreement with experimental results reported in reference [51], and contradicts the theoretical results reported by Gray [22].

From the non-dimensional form of the stresses, it can be easily seen that the spalling rate increases with increasing thermal diffusivity, in agreement with other analytical and experimental work [20,26,35].

The results are plotted in a form suitable for design use.

2. SUGGESTIONS

To improve the results of this study, more work is needed. Many interesting extensions are possible. Also, despite our effort to relax some of the simplifying assumptions which abound in the models used in the literature, the present approaches still have many limitations.

First, the approximate technique of fictitious boundary conditions is only derived for linear heat-conduction problems. In general, the technique can be applied to parabolic partial differential equations. For other categories of problems, the technique may lose its advantages over existing techniques. However, for some cases, e.g., hyperbolic partial differential equations, it is conjectured that the technique may still offer simple and accurate solutions under certain conditions. It is therefore of interest to evaluate the technique for other categories of problems and study the necessary modifications. The extension of the technique to two and three-dimensional problems is also a topic for research. The analytical steps for this are straightforward but the numerical evaluations are non-trivial.

Second, the criterion for failure based on the modified Coulomb-Mohr theory assumes a perfectly elastic isotropic model. Many parameters, e.g., petrographic properties, creep, fusion, etc., have been ignored because they differ for each specific application. Some of these are implicitly and partially reflected in the thermal-elastic properties of the material but for a specific design these parameters have to be explicitly considered. For this purpose, statistical approaches may be needed. A statistical approach similar to the Weibull theory of failure may also be used in conjunction with the failure factor distribution to predict failure more accurately. Another limitation of the present models is the assumption of axi-symmetry. For other geometries, the results from this study should therefore be viewed only as a qualitative basis to predict the mode of failure, and not as quantitative read-off-the-chart data for design.

Third, the orientation of the plane of the major principal stress was not computed. This information contributes to the prediction of the path of crack propagation and plane of fracture. It also helps explain the shape of the spalls.

Finally, the behavior of the longitudinal stress remains unexplained. Some authors mentioned without explanation this peculiar behavior of thermal stresses, i.e., considerable stresses may exist in regions far beyond the reach of thermal effects. Intuitively, this can be explained as the result of boundary effects. However, a rigorous theoretical explanation is still lacking. A study of this behavior of thermal stresses will no doubt further our understanding of thermal stresses and the related problems of thermal shock and thermal spalling.

APPENDICES

APPENDIX A. UNIQUENESS THEOREM

Let us consider the following heat conduction problem:

$$\frac{\partial^2}{\partial x^2}T_2(x,t) + \frac{1}{k}\, g_1(x,t) = \frac{1}{\kappa}\cdot\frac{\partial}{\partial t}T_2(x,t), \quad 0 \le x \le L,\ 0 \le t, \tag{A.1.a}$$

$$-k\frac{\partial}{\partial x}T_2(x,t) + hT_2(x,t) = -k\frac{\partial}{\partial x}T_1(x,t) + hT_1(x,t), \text{ at } x = x_1, \tag{A.1.b}$$

$$k\frac{\partial}{\partial x}T_2(x,t) + hT_2(x,t) = k\frac{\partial}{\partial x}T_1(x,t) + hT_1(x,t), \text{ at } x = L, \tag{A.1.c}$$

$$T_2(x,t) = T_1(x,t), \quad \text{at } t = t_1, \tag{A.1.d}$$

where $T_1(x,t)$ is the solution of

$$\frac{\partial}{\partial x}T_1(x,t) + \frac{1}{k}g_1(x,t) = \frac{1}{\kappa}\,\frac{\partial}{\partial t}T_1(x,t), \quad x_1 \le x \le L,\ 0 \le t, \tag{A.2.a}$$

$$-k\frac{\partial}{\partial x}T_1(x,t) + hT_1(x,t) = \phi_1(t), \text{ at } x = 0, \tag{A.2.b}$$

$$k\frac{\partial}{\partial x}T_1(x,t) + hT_1(x,t) = \psi_1(t), \quad \text{at } x = L, \tag{A.2.c}$$

$$T_1(x,t) = 0, \quad \text{at } t = t_1. \tag{A.2.d}$$

$T_1(x,t)$ also satisfies the boundary and initial conditions of $T_2(x,t)$. Let $W = T_2(x,t) - T_1(x,t)$. It is obvious that subtracting Equation (A.1.a) from Equation (A.2.a) will give

$$\frac{\partial^2 W}{\partial x^2} = \frac{1}{\kappa}.\frac{\partial W}{\partial t} \quad , \; x_1 \leq x \leq L, \; t_1 \leq t \; , \tag{A.3.a}$$

$$-k\frac{\partial W}{\partial x} + hW = 0, \quad \text{at } x = x_1, \tag{A.3.b}$$

$$k\frac{\partial W}{\partial x} + hW = 0, \quad \text{at } x = L, \tag{A.3.c}$$

$$W = 0, \quad \text{at } t = t_1. \tag{A.3.d}$$

Now multipling both sides of Equ. (A.3.a) by W and integrating from $x = x_1$ to $x = L$ gives

$$\int_{x_1}^{L} W \frac{\partial^2 W}{\partial x^2} \, dx = \frac{1}{\kappa}. \int_{x_1}^{L} W \frac{\partial W}{\partial t} \, dx. \tag{A.4}$$

Integrating the left-hand-side by parts and changing the order of the partial derivative and the integral in the rigth-hand-side, we obtain

$$W \frac{\partial W}{\partial x}\Big|_{x_1}^{L} - \int_{x_1}^{L} \left(\frac{\partial W}{\partial x}\right)^2 dx = \frac{1}{\kappa} \frac{\partial}{\partial t} \int_{x_1}^{L} W^2 \, dx. \tag{A.5}$$

Evaluating the first term on the left-hand-side at the boundaries gives

$$-\frac{h}{k} W^2\Big|_{x=L} - \frac{h}{k} W^2\Big|_{x=x_1} - \int_{x=x_1}^{L} \left(\frac{\partial W}{\partial x}\right)^2 dx = \frac{1}{\kappa} \frac{\partial}{\partial t} \int_{x=x_1}^{L} W^2 \, dx \tag{A.6}$$

The expression on the right-hand-side is negative, that is, the integral cannot increase with time. On the other hand, the integral cannot be negative because its integrand is a square. Since the initial value of W is zero and since the integral cannot increase with time, it must therefore be identically zero for all time, and throughout the region $[x_1,L]$. This is possible only when the integrand is identically zero. In other words, $T_2(x,t) \equiv T_1(x,t)$.

The above result proves the uniqueness of solutions to the type of problems considered here.

A more thorough discussion of the Uniqueness Theorem for heat conduction problems is presented in [8,11].

APPENDIX B. UNCOUPLING OF THERMAL AND ELASTIC PROBLEMS

Although the differential equations for temperature and stress are coupled in many practical situations, the coupling of stress on temperature is negligible. A measure of the degree of coupling is given by [8]

$$\delta << 1, \tag{B.1}$$

where δ is defined as

$$\delta = \frac{(3\lambda + 2\mu)^2 \alpha^2 T_0}{\rho^2 C_v v_e^2}. \tag{B.2}$$

This formulation involves the Lame's constants λ and μ, the linear thermal expansion coefficient α, the density ρ, the specific heat capacity C_v, and the dilatational wave velocity v_e. The temperature T_0 is the average heating temperature.

For granite, these values are obtained from [13,18,58,59,61] and are listed in Table 5.1.

The Lamé's constants can be computed as [29]:

$$\lambda = \frac{E\nu}{(1+\nu)(1-2\nu)} = 1.6667E10, \tag{B.3}$$

$$\mu = \frac{E}{2(1+\nu)} = 2.5E11, \tag{B.4}$$

which gives

$$\delta = 0.044 << 1. \tag{B.5}$$

For most rocks δ is also negligible compared to unity, and the thermal and elastic problem are essentially uncoupled.

APPENDIX C. REPETITIVE THERMAL SPALLING DUE TO HEATING

1. SOLUTION WITH THE TECHNIQUE OF FICTITIOUS BOUNDARY CONDITIONS

The slab of size L in figure 4.1.a is initially at uniform temperature $T_0 = 0$. If the initial temperature were not at 0, a simple linear transformation of variable would transform the problem into the one considered here. The constant heat flux q" is applied over the surface at x = 0. All material properties are assumed constant. Convective and radiative heat transfer are considered negligible compared to conductive heat transfer. The dimension L is chosen to be large enough so that the heat layer is always less than L.

Under the above assumptions, the problem can be formulated as follows.

$$\frac{\partial^2}{\partial x^2}T_1(x,t) = \frac{1}{\kappa}.\frac{\partial}{\partial t}T_1(x,t),\ 0 \le x \le L,\ 0 \le t, \qquad \text{(C.1.a)}$$

$$-k.\frac{\partial}{\partial x}T_1(x,t) = q'', \qquad \text{at } x = 0, \qquad \text{(C.1.b)}$$

$$T_1(x,t) = 0, \qquad \text{at } x = L, \qquad \text{(C.1.c)}$$

$$T_1(x,t) = 0, \qquad \text{at } t = 0. \qquad \text{(C.1.d)}$$

The solution is obtained by the integral transform method, i.e., from Equation 3.1.2, and is given below.

where

$$\beta m = \frac{2m_1 + 1}{L}\pi, \qquad m_1 = 1,2,3,... \tag{C.2.b}$$

At time $t = t_1$ a thin layer of material of size x_1 spalls off due to fracture caused by induced stresses. The same heat flux q'' is moved to the newly exposed surface at $x = x_1$. The initial temperature distribution at $t = t_1$ is the residual temperature distribution from the preceding thermal phase.

The second thermal phase is formulated similar to the one above, with some modifications.

$$\frac{\partial^2}{\partial x^2}T_2(x,t) = \frac{1}{\kappa}\cdot\frac{\partial}{\partial t}T_2(x,t), \quad x_1 \le x \le L, \quad t_1 \le t, \tag{C.3.a}$$

$$-k.\frac{\partial}{\partial x}T_2(x,t) = q'', \qquad \text{at } x = x_1, \tag{C.3.b}$$

$$T_2(x,t) = 0, \qquad \text{at } x = L, \tag{C.3.c}$$

$$T_2(x,t) = T_1(x,t), \qquad \text{at } t = t_1, \tag{C.3.d}$$

With the technique of fictitious boundary conditions, the solution is considered to be made up of two components, one of which is forced to be the continuation of the solution from the preceding thermal phase. That is

$$T_2(x,t) = T_1(x,t) + T_2''(x,t). \tag{C.4}$$

This reformulation of the problem forces $T_2''(x,t)$ to be the solution of the following partial differential equation.

$$\frac{\partial^2}{\partial x^2}T_2''(x,t) = \frac{1}{\kappa}\cdot\frac{\partial}{\partial t}T_2''(x,t), \quad x_1 \le x \le L, \; t_1 \le t, \tag{C.5.a}$$

$$- k\frac{\partial}{\partial x}T_2''(x,t) = q'' + k\frac{\partial}{\partial x}T_1(x,t), \qquad \text{at } x = x_1, \tag{C.5.b}$$

$$T_2''(x,t) = 0, \qquad \text{at } x = L, \tag{C.5.c}$$

$$T_2''(x,t) = 0, \qquad \text{at } t = t_1. \tag{C.5.d}$$

The right-hand-side of Equation C.5.b is the transient heat flux at $x = x_1$ from the previous solution and can be approximated with an exponential function of the form $b_1\exp(\kappa c_1 t)$. The constant term is not needed because the transient heat flux vanishes at steady-state.

Thermal diffusivity is included in the exponent to make the solution of all thermal phases to have similar functional forms. It turns out that in this problem the exponential form gives somewhat better accuracy and is more efficient than a polynomial.

The solution for the second thermal phase is now given as

$$T_2(x,t) = -\frac{1}{L}\frac{q''}{k}\sum_{m_1=0}^{\infty}\frac{e^{-\kappa\beta m_1^2 t}\cos(\beta m_1 x)}{\beta m_1^2} + \frac{q''}{k}(L - x)$$

$$+ \frac{2}{(L - x_1)}\frac{q''}{k} b_1 \sum_{m=0}^{\infty} e^{-\kappa\beta m_2^2 (t-t_1)}\cos(\beta m_2 (x-x_1))[A] \qquad (C.6.a)$$

where

$$[A] = \frac{e^{\kappa(\beta m_2^2 + c_1)(t - t_1)} - 1}{\beta m_2^2 + c_1}, \qquad (C.6.b)$$

and

$$\beta m_2 = \frac{2m_2 + 1}{(L - x)}, \qquad m_2 = 1,2,3,\ldots \qquad (C.6.c)$$

Following the same procedure as above, the general solution for the n^{th} thermal phase is given as follows.

$$T_n(x,t) = \frac{q''}{k}\sum_{i=1}^{n}\{\frac{2}{(L - x_i)}\sum_{m=0}^{\infty} e^{-\kappa\beta m_i^2 (t-t_i)}\cos(\beta m_i (x-x_i))\sum_{j=i}^{i-1}[Xj]\} \qquad (C.7.a)$$

$$[X_j] = b_j\,[\frac{e^{\kappa(\beta m_i^2 + c_j)(t-t_i)} - 1}{\beta m_i^2 + c_j}], \qquad (C.7.b)$$

$$x_1 = 0, \tag{C.7.d}$$

$$t_1 = 0, \tag{C.7.e}$$

$$b_0 = 1, \tag{C.7.f}$$

and

$$c_0 = 0. \tag{C.7.g}$$

The index n denotes the different thermal phases.

Other exponential forms for the approximating function has been experimented. An approximating function in form of a series of exponentials with one term added for each new thermal phase gives negligible improvement in accuracy in exchange for large increase in computing time and thus is not used here.

2. APPROXIMATE SOLUTION BY APPROXIMATING THE INITIAL CONDITION

The solution for the first thermal phase is exact, and is given in Equation C.2 above. The initial condition in the second thermal phase is now approximated, say by a third-order polynomial of the form

$$F_1(x,t_1) = a_1 + b_1x + c_1x^2. \tag{C.8}$$

Applying the technique of integral transform again, $T_2(x,t_1)$ is computed as

$$T_2(x,t) = \frac{2}{L_2} \sum_{m_2=0}^{\infty} e^{-\kappa\beta m_2^2(t-t_1)} \cos(\beta m_2 x) \left[\int_0^{L_2} \cos(\beta m_2 x') F_1(x'+x_2)dx' + \frac{\kappa q''}{k} \int_0^{t'} e^{\kappa\beta m_2^2(t'-t_1)}dt' \right], \tag{C.9.a}$$

where

$$\beta m_2 = \frac{2m_2 + 1}{2L_2}\pi. \qquad \text{(C.9.b)}$$

The same process is repeated for as many times as necessary. The general solution for the n^{th} thermal phase is given below.

$$T_n(x,t) = \frac{2q''}{L_n k}\sum_{m_n=0}^{\infty} e^{-\kappa\beta m_n(t-t_n)}\cos(\beta m_n(x-x_n))[X_n]$$
$$- \frac{2q''}{L_n k}\sum_{m_n=0}^{\infty}\frac{e^{-\kappa\beta m_n(t-t_n)}\cos(\beta m_n(x-x_n))}{\beta m^2} + \frac{q''}{k}(L_1-x). \qquad \text{(C.10.a)}$$

where

$$\beta m_n = \frac{2m_n + 1}{2L_n}\pi, \qquad \text{(C.10.b)}$$

and

$$[X_n] = \frac{a_n\sin(\beta m_n L_n)}{\beta m_n} - \frac{b_n}{\beta m_n} + \frac{c_n L_n\sin(\beta m_n L_n)}{\beta m_n}$$
$$+ c_3\left(\frac{L_n}{\beta m_n} - \frac{2}{\beta m_n}\right)\sin(\beta m_n L_n). \qquad \text{(C.10.c)}$$

APPENDIX D. DEFINITION OF THE FAILURE FACTOR

The safety factor in the modified Coulomb-Mohr theory of failure is defined as

$$n_s = \begin{cases} -S_c/\sigma_3 & \text{for } \sigma_1 \leq 0, \\ S_t/\sigma_1 & \text{for } \sigma_3 > 0, \\ S_3/\sigma_3 & \text{for } \sigma_3 \leq -S_t,\ \sigma_1 > 0. \end{cases} \qquad (D.1)$$

In the above expression, σ_1 and σ_3 are principal stresses such that $\sigma_3 \leq \sigma_2 \leq \sigma_1$. The compressive strength S_c is defined as a positive quantity. The limiting value of σ_3, S_3, is computed as

$$S_3 = \frac{S_c}{\frac{S_c - S_t}{S_t}\frac{\sigma_1}{\sigma_3} - 1}. \qquad (D.2)$$

The failure factor used in this work is defined as the inverse of the safety factor, i.e., $F = 1/n_s$.

BIBLIOGRAPHY

1. J. H. Ainsworth, "Calculation of Safe Heat-Up Rates for Steel Plant Furnace Linings", Am. Cer. Soc. Bull., Vol. 58, pp. 676-678, 1979.

2. J. H. Ainsworth and R. H. Herron, "Thermal Shock Damage Resistance of Refractories", Am. Cer. Soc. Bull., Vol. 53, pp. 533-538, 1974.

3. B. J. Aleck, "Thermal Stresses in a Rectangular Plate Clamped along an Edge ", J. Appl. Mech., Vol. 16, 118-122, 1949.

4. V. S. Arpaci, "Conduction Heat Transfer", Addison-Wesley, Massachusetts, 1966.

5. H. Becker, "An Exploratory Study of Stress Concentrations in Thermal Shock Fields", J. Eng. for Indust., Vol. 84, No. 3, pp. 343-348, 1962.

6. B. A. Boley, "The Embedding Technique in Melting and Solidification Problems", Moving Boundary Problems in Heat Flow and Diffusion, Edited by J. R. Ockendon and W. R. Hodgkins, Clarendon Press, Oxford, U.K., 1975.

7. B. A. Boley, "A Method of Heat Conduction Analysis of Melting and Solidification Problems, J. of Mat. and Phys. Vol. 40, no. 4, pp. 300-313, 1961.

8. B. A. Boley and J. H. Weiner, "Theory of Thermal Stresses", John Wiley & Sons, Inc., New York, 1960.

9. B. Brezny, "Crack Formation in BOF Refractories during Gunning", Am. Cer. Soc. Bull, Vol. 58 , pp. 679-682, 1979.

10. R. S. Carmichael, "Handbook of Physical Properties of Rocks", CRC Press, Fla., 1982.

11. H. S. Carslaw and J. C. Jaeger, "Conduction of Heat in Solids", 2nd Ed., Clarendon Press, Oxford, U.K., 1973.

12. W. S. Chang, et al., "Analysis of Thermal Stress Failure of Segmented Thick-Walled Refractory Structures", J. of Am. Cer. Soc. Vol. 66, pp. 708-713, 1983.

13. S. P. Clark, Jr., "Handbook of Physical Constants", Geological Soc. of America, Inc. New York, 1966.

14. R. D. Cook, "Concepts and Applications of Finite Element Analysis", 2nd ed., John Wiley & Sons, New York, 1981.

15. L. Davison and L. A. Stevens, "Continuum Measures of Spall Damage", J. Appl. Phys., Vol. 43, pp. 988-994, 1972.

16. L. Davison and L. A. Stevens, "Thermomechanical Constitution of spalling Elastic Bodies", J. Appl. Phys., Vol. 44, pp. 668-674, 1973.

17. G. J. DeSalvo and J. A. Swanson, "ANSYS Engineering Analysis System User's Manual", Houston, Pensylvania, 1983.

18. W. H. Duckworth, "Precise Tensile Properties of Ceramic Bodies", J. Am. Ceram. Soc., Vol. 34, pp. 1-9, 1951.

19. A. F. Emery, "Thermal Stress and Fracture in Elastic-Brittle Materials", Thermal Stresses in Severe Environments, edited by D. P. H. Hasselman and R. A. Heller, Plenum Press, New York, 1980.

20. D. C. Freeman, Jr., J. A. Sawdye, and F. A. Mumpton, "The Mechanism of Thermal Spalling in Rocks", Quarterly of the Colorado School of Mines, pp. 225-52.

21. B. E. Gatewood, "Thermal Stresses", McGrawHill Book Co., Inc., Toronto, Canada, 1957.

22. W. M. Gray, "Surface Spalling by Thermal Stresses in Rocks", Proceedings of the Symposium on Rock Mechanics, Univ. of Toronto, Dpt. of Mines and Technical Surveys, pp. 85-106, Jan. 1965.

23. D. P. H. Hasselman, "Unified Theory of Thermal Shock Fracture Initiation and Crack Propagation of Brittle Ceramics", J. Am. Ceram. Soc., Vol. 52, p. 600-604, 1969.

24. D. P. H. Hasselman, "Thermal Stress Resistance Parameters for Brittle Refractory Ceramics: A Compendium", Am. Ceram. Soc. Bull., Vol. 49, pp. 1033-37, 1970.

25. R. A. Heller, "The Stress-Volume Integral for Brittle Materials", Personal Notes, Department of Material Sciences, VPI&SU.

26. H. Henke, J. R. Thomas, Jr., and D. P. H. Hasselman, "Role of Material Properties in the Thermal-Stress Fracture of Brittle Ceramics Subjected to Conductive Heat Transfer", J. Am. Ceram. Soc., Vol. 67, pp. 393-398, 1984.

27. W. Jaunzemis and E. Sternberg, "Transient Thermal Stresses in a Semi-Infinite Slab", J. Appl. Mech., Vol. 26, pp. 503-509, 1959.

28. W. D. Kingery, "Factors Affecting Thermal Stress Resistance of Ceramic Material", J. Am Ceram. Soc., Vol. 38, pp. 3-15, 1955.

29. H. Kolsky, "Stress Waves in Solids", Dover Publications Inc., New York, 1963.

30. W. G. Lidman and A. R. Bobrowsky, "Correlation of Physical Properties of Ceramic Materials with Resistance to Fracture by Thermal Shock", NACA Technical Note 1918, July 1949.

31. S. S. Manson, "Behavior of Materials under Conditions of Thermal Stresses", NACA TN 2933, 1953.

32. S. S. Manson and R. W. Smith, "Theory of Thermal Shock Resistance of Brittle Material Based on Weibull's Statistical Theory of Strength", J. of Am. Ceram. Soc., January, 18-27, 1954.

33. S. S. Manson and R. W. Smith, "Quantitative Evaluation of Thermal Shock Resistance", Trans. ASME, pp. 533-544, April 1956.

34. S. S. Manson, "Thermal Stress and Low-Cycle Fatigue", McGraw-Hill, New York, 1966.

35. V. V. Mirkovich, "Experimental Study Relating Thermal Conductivity to Thermal Piercing of Rocks", Int. J. Rock Mech. Min. Sci., Vol. 5, pp. 205-218, 1968.

36. V. V. Mirkovich and K. E. Bell, "A Novel Method for Predicting Thermal Shock Resistance of Brittle Materials", J. of the Canadian Cer. Soc., vol. 50, pp. 29-33, 1981.

37. T. D. Nguyen, "Effect of Thermal Diffusivity on Thermal Stresses in a Flat Plate Subjected to Rapid Thermal Cycling", Master's thesis, VPI&SU, 1983.

38. F. H. Norton, "A General Theory of Spalling", J. Amer. Ceram. Soc., vol. 8, pp. 29-39, 1925.

39. F. H. Norton, "The Mechanism of Spalling", J. Amer. Cer. Soc., vol. 9, pp. 446-461, 1926.

40. F. H. Norton, "Discussion of Theory of Spalling", J. of Am. Cer. Soc., Vol. 16, pp. 423-424, 1933.

41. J. L. Nowinski, "Theory of Thermoelasticity with Applications", Sifthoff and Noordhoff, New York, 1978.

42. L. Obert, S. L. Windes, and W. I. Duvall, "Standardized Tests for Determining the Physical Properties of Mine Rocks", Report of Investigation, Bureau of Mines, August 1946.

43. D. R. J. Owen and A. J. Fawkes, "Engineering Fracture Mechanics: Numerical methods and Applications", Pineridge Press Ltd., Swansea, U.K., 1983.

44. M. N. Ozisik, "Boundary Value Problems of Heat Conduction", International Textbook Co., Pennsylvania, 1968.

45. M. N. Ozisik, "A Note on the General Formulation of Phase Change Problem as Heat Conduction Problem with a Moving Heat Source", Trans. ASME, Vol. 100, May 1978.

46. M. N. Ozisik, "Heat Conduction", John Wiley & Sons, New York, 1980.

47. A. P. Parker, "The Mechanics of Fracture and Fatigue", E. & F.N. SPON Ltd, New York, 1981.

48. F. W. Preston, "The Spalling of Bricks", J. of Am. Cer. Soc., Vol. 9, pp. 654-658, 1926.

49. R. A. Robie, B. S. Hemingway, and J. R. Risher, "Thermodynamic Properties of Minerals", Geological Survey Bulletin 1452, U.S. Govt. Printing Office, Washington, 1979.

50. H. C. Rolseth and R. H. Kohler, "Rocket-Jet Burners Cut Time and Costs in Granite Quarries", Mining Engineer, July 1969.

51. J. A. Soles and L. B. Geller, "Experimental Studies Relating Mineralogical and Petrographic Features to the Thermal Piercing of Rocks", Technical Bulletin 53, Mines Branch, Dept. of Mines and Technical Surveys, Ottawa, Canada, Jan. 28, 1962.

52. J. E. Shigley and L. D. Mitchell, "Mechanical Engineering Design", 4th ed., McGraw-Hill, 1983.

53. K. G. Stagg and O. C. Zienkiewicz, "Rock Mechanics in Engineering Practice", John Wiley & Sons, Inc., Sydney, Australia, 1968.

54. S. B. Stellan Persson, "Thermal Shock Resistance of Refractories: Correlation Between Relative Loss of Strength and the Thermal Stress Resistance Parameters, R_{st}", Advances in Ceramic Processing, Edited by P. Vincenzini, National Research Council, Forenza, Italy, 1978. pp. 325-328.

55. A. S. Tetelman and A. J. McEvily, "Fracture of Structural Materials", John Wiley, New York, 1967.

56. K. Thirumalai, "Process of Thermal Spalling Behavior in Rocks: An Exploratory Study", Rock Mechanics: Theory and Practice, Edited by W. H. Somerton, Proceedings of the 11th Symposium on Rock Mechanics, Univ. of CA at Berkeley, pp. 705-727, June 1969.

57. L. H. Van Vlack, "Elements of Material Sciences and Engineering", 4th. ed., Addison-Wesley, Massachusetts, 1981.

58. V. S. Vutukuri, R. P. Lama, S. S. Saluja, "Handbook on Mechanical Properties of Rocks, Vol. I, Trans Tech Publications, Switzerland, 1974.

59. V. S. Vutukuri and R. P. Lama, "Handbook on Mechanical Properties of Rocks", vol. II-IV, Trans Tech Publications, Switzerland, 1978.

60. R. E. Walpole and R. H. Myers, "Probability and Statistics for Engineers and Scientists", 2nd ed., MacMillan, New York, 1978.

61. W. H. Walton, "Mechanical Propeties of Non-Metallic Brittle Materials", Interscience Publishers Inc., New York, 1958.

62. "SAS User's Guide", 1982 Edition, SAS Institute Inc., Cary, North Carolina.

The vita has been removed from the scanned document